

Master's Dissertation in Mechanical Engineering on:

**Mesh stiffness and load sharing ratio
along the path of contact in parallel axis
involute spur gears**

Gonçalo Dias Teixeira da Silva

Supervisor: Doutor Pedro M. T. Marques
Co-Supervisor: Engenheiro João D. M. Marafona
Co-Supervisor: Professor Jorge H. O. Seabra



Mestrado Integrado em Engenharia Mecânica

September, 2021

*“Pelo sonho é que vamos,
Comovidos e mudos.
Chegamos? Não chegamos?
Haja ou não frutos,
Pelo Sonho é que vamos.
Basta a fé no que temos.
Basta a esperança naquilo
Que talvez não teremos.
Basta que a alma demos,
Com a mesma alegria,
Ao que desconhecemos
E ao que é do dia-a-dia.*

Chegamos? Não chegamos?

- Partimos. Vamos. Somos.”

Sebastião da Gama, *O Sonho*

This page was intentionally left blank.

Resumo

Neste trabalho, um modelo recorrendo ao Método dos Elementos Finitos, MEF, é desenvolvido de modo a avaliar a influência de determinados parâmetros geométricos na rigidez de engrenamento de engrenagens cilíndricas de dentado reto e eixos paralelos. Também se procura avaliar a influência desses parâmetros para posterior calibração de um modelo analítico aproximado. A maneira como esse modelo introduz o conceito de função Heaviside permite avaliar a rigidez de engrenamento de vários pares de dentes partindo da sobreposição de apenas um deles, através da razão de condução, permitindo que o modelo numérico adquira uma configuração mais simples. Este modelo depende de um parâmetro que é a razão entre o valor máximo e mínimo da parábola que define a rigidez de um único par de dentes ao longo do caminho de engrenamento, α_k . O objetivo deste trabalho foi então procurar a relação deste parâmetro com os vários parâmetros geométricos que definem a geometria do dentado de engrenagens.

Uma determinada roda com uma dada geometria é gerada através do *KISSsoft*. O modelo CAD é exportado e trabalhado no *SolidWorks*. De seguida, o modelo de Elementos Finitos é desenvolvido usando *ANSYS*. É efetuado um estudo de convergência para se chegar a uma configuração final. O erro de transmissão que é obtido pelo modelo de Elementos Finitos é usado para determinar a rigidez de engrenamento, permitindo a determinação do parâmetro livre α_k , que desempenha um papel crucial não só na rigidez de engrenamento como na distribuição de carga. Este parâmetro livre manifestou variações significativas com a alteração de alguns parâmetros, nomeadamente o factor de addendum, o factor de redução de addendum, as modificações de perfil na direção axial e a razão de condução; por outro lado, parâmetros como o módulo, o factor de raio de pé, a razão de transmissão, o factor de dedendum e a correção de dentado tiveram menor influência. As modificações de perfil na direção axial não permitiram uma análise tão direta. Os resultados numéricos mostraram também que as curvas pré-existentes para descrever o andamento de α_k não eram as mais adequadas.

A maioria dos trabalhos realizados atualmente e que podem ser consultados na literatura estabelecem o valor deste parâmetro livre, α_k , como sendo função apenas da razão de condução. Este trabalho demonstra que outros fatores devem ser tidos em conta. De facto a existência de valores diferentes de α_k para a mesma razão de condução é evidência de que a primeira grandeza não pode ser definida como função apenas da segunda.

Palavras-chave: Rigidez de engrenamento, Distribuição de carga, Modelo de Elementos Finitos, Engrenagens cilíndricas de dentado reto e eixos paralelos.

This page was intentionally left blank.

Abstract

In this work, a model based on the Finite Element Method, FEM, is developed to evaluate the influence of gear tooth geometry on the parallel axis spur gear mesh stiffness. This work also aims to evaluate such influence and use it to calibrate an approximated analytical model. The way the model introduces the Heaviside function to evaluate the gear mesh stiffness of the whole gear as a superposition of gear mesh stiffness of a single tooth pair, taking into account the contact ratio, makes the model have a simpler configuration. This model also depends on a parameter that defines the ratio between the maximum and minimum value of the parabola that defines the gear mesh stiffness of a single teeth pair along the contact path, α_k . The goal of this work was then attempting to find the relationship between this parameter and the several geometric parameters that define the geometry of the gear teeth.

A gear with a certain geometry is generated using *KISSsoft*. The CAD model exported is handled in *SolidWorks*. Then, the Finite Element model is developed using *ANSYS*. A convergence study is done to reach the final configuration of the model. The transmission error obtained from the Finite Element model is used to obtain the gear mesh stiffness, which allows the determination of the value of a free parameter, α_k , which plays a major role in gear mesh stiffness and load sharing ratio of spur gears. This free parameter showed significant variation as the some parameters were altered, namely the addendum factor, the tip alteration factor, the profile modifications on the axial direction and the contact ratio; on the other hand, the module, the root radius factor, the gear ratio, the dedendum factor and the profile shift coefficient had a smaller influence. The axial profile modifications did not allow for such a straightforward analysis. The numerical values also show that the pre-existing curves describing α_k do not perform so well.

The vast majority of the work done until now and that can be consulted in the literature only establishes the value of this free parameter, α_k , based on the contact ratio of the gears. This work shows that other factors must be taken into account. In fact, considering that, for the same driving ratio, different values of α_k were obtained, considering α_k a function of the driving ratio alone is mathematically incorrect.

Keywords: Gear Mesh Stiffness, Load Sharing, Finite Element Model, Parallel Axis Spur Gears.

This page was intentionally left blank.

Acknowledgments

To my supervisors, Doutor Pedro Marques, Engenheiro João Marafona and Professor Jorge Seabra, for kindly accepting to supervise me in this work, for always guiding me throughout its many steps and providing extensive knowledge without which this would not have been possible. Thank you for the opportunity to work with and learn from people I admire.

To my mother, father and brother, for always being the most supportive people I could ever ask for. Thank you for the advice at any occasion, for listening and being there in my worst and best times and always making sure I had someone that had my back, no matter what. Thank you for believing in me, even when I doubted myself the most and trying to make me believe in myself. Thank you for always being by my side, I immensely love you and always will.

To my friends, who always cheered me up during the darkest times and celebrated with me during the best. Thank you for the companionship, giving me strength to endure hardships, advising me and always striving to better yourselves and pushing me to do the same. Thank you for being the best part of these last years and for the memories I will cherish for eternity.

This page was intentionally left blank.

Contents

Notation	xi
1 Introduction	1
1.1 Motivation	1
1.2 Main Goal	1
1.3 Outline	2
2 Gear Mesh Stiffness	3
2.1 Brief History	3
2.2 Mesh Stiffness	6
2.3 Mesh Stiffness and Load Sharing Models	8
2.3.1 Potential Energy Method	9
2.3.2 Method B - ISO 6336-1-2006	15
2.3.3 Finite Element Models	20
2.3.4 Hybrid Model	23
2.3.5 Experimental Determination of Gear Mesh Stiffness	25
2.4 Approximated Analytical Model	28
2.4.1 Description on the length of the contact lines	28
2.4.2 Quasi-static elastic model	31
2.4.3 Load sharing and the free parameter importance and determination	32
3 Gear Geometry and Simulation Landscape	35
3.1 Geometric Parameters	35
3.1.1 Module	35
3.1.2 Pressure angle	36
3.1.3 Gear ratio and number of teeth	36
3.1.4 Tip alteration	37
3.1.5 Profile	37
3.1.6 Profile Modifications	38
3.1.7 Contact Ratio	38
3.2 Parameter Matrix	39
3.3 Hertzian contact model	42
3.4 Torsional Model	45
4 Simulation preparation and setup	49
4.1 Tools	49
4.2 Gear Geometry Definition	49
4.2.1 Geometry Generation	49
4.2.2 Geometry Manipulation	51

4.3	Simulation preparation: ANSYS Workbench	56
4.3.1	Boundary Conditions	57
4.3.2	Contact	63
4.3.3	Meshing	66
4.3.4	Solution and Results	77
4.3.5	Special Cases	80
4.3.6	Validation	82
5	Results and Discussion	87
5.1	Results	87
5.1.1	Coordinate Shift	87
5.1.2	M4_5	88
5.1.3	ER1	89
5.1.4	ER2	92
5.1.5	ER1M45	93
5.1.6	Summary	95
5.2	α_k parameter	96
6	Conclusions and Future Works	101
6.1	Main Conclusions	101
6.2	Future Work	101
	References	103
	Appendices	107
A	Zienkiewicz-Zhu estimator	109
B	Transmission Error and Mesh Stiffness Curves	111

Notation

Abbreviations

CAD	Computer Aided Design
DOF	Degree of Freedom
EV	Electric Vehicle
FEA	Finite Element Analysis
FEM	Finite Element Method
HRC	Rockwell C Hardness
ICE	Internal Combustion Engine
ISO	International Organization for Standardization
LVDT	Linear Variable Differential Transformer
STS	Single Tooth Stiffness
TVMS	Time Varying Mesh Stiffness
ZZ	Zienkiewicz-Zhu

Symbols

a	Contact semi-width (mm)
α	Pressure angle ($^{\circ}$)
α_c	Load angle ($^{\circ}$)
α_k	Ratio between the thin slice pair mesh stiffness at $\xi = 0$ and $\xi = \varepsilon_{\alpha}$ and its value at $\xi = \frac{\varepsilon_{\alpha}}{2}$ (-)
α_T	Angle given by the inverse cosine of the ratio base radius and load point radius (rad)
A_c	Cross section area (m^2)
A	Equivalent curvature along X (mm^{-1})
b	Gear facewidth (mm)
b_s	Web thickness (mm)
b_E	Length to starting point C_{β} from side I/II (mm)
b_X	Length of crowning from side I/II to the center of crowning (mm)
β	Helix angle ($^{\circ}$)
B	Equivalent curvature along Y (mm^{-1})
c'	Maximum tooth stiffness per unit face width (single stiffness) of a tooth pair ($\text{N}\cdot\text{mm}^{-1}\mu\text{m}^{-1}$)
c_{th}'	Theoretical single stiffness ($\text{N}\cdot\text{mm}^{-1}\mu\text{m}^{-1}$)
$c_{\gamma\alpha}$	Mean value of mesh stiffness per unit face width (used for K_v , $K_{F\alpha}$, $K_{H\alpha}$) ($\text{N}\cdot\text{mm}^{-1}\mu\text{m}^{-1}$)

$c_{\gamma\beta}$	Mean value of mesh stiffness per unit face width (used for $K_{F\beta}$, $K_{H\beta}$) ($\text{N}\cdot\text{mm}^{-1}\mu\text{m}^{-1}$)
$C_1 - C_9$	Coefficients for the determination of q' (-)
C_a	Coefficient for the determination of the smaller axis of the contact ellipse (-)
C_B	Basic rack factor for pinion and wheel (-)
C_β	Crowning height (mm)
C_{B1}	Basic rack factor for pinion (-)
C_{B2}	Basic rack factor for wheel (-)
C_f	Correction factor (-)
C_M	Correction factor (-)
C_R	Gear blank factor (-)
d	Pitch diameter (-)
e	Gear backlash
$e(y)$	Tooth chordal thickness at section y (m)
ξ	Adimensional coordinate on the line of action (-)
ξ_C	Normalized coordinate of the tooth load point (-)
ε_α	Transverse contact ratio (-)
E	Modulus of elasticity, Young's modulus (GPa)
E^*	Combined modulus of elasticity (GPa)
f_N	Normal force per length ($\text{N}\cdot\text{mm}^{-1}$)
F_c	Compressive load (N)
F_N	Tooth normal force (N)
F_t	Nominal transverse tangential load at reference cylinder per mesh (-)
G	Shear modulus (GPa)
h_{ap}^*	Addendum coefficient (-)
h_{fp}^*	Dedendum coefficient (-)
$H(\xi)$	Heaviside function (-)
i	Transmission ratio (-)
I	Second moment of area (mm^4)
J	Rotary inertia ($\text{kg}\cdot\text{m}^2$)
K	Stiffness ($\text{N}\cdot\text{m}^{-1}$)
k	Tip alteration factor (-)
k_{ab}	Ratio between the bigger and smaller axes of the contact ellipse (-)
K_t	Torsional mesh stiffness ($\text{N}\cdot\text{m}\cdot\text{rad}^{-1}$)
k^{st}	Single tooth stiffness of gear i ($\text{N}\cdot\text{m}^{-1}$)
k^{Cai}	Cai's single mesh stiffness (-)
k^l	Linear stiffness ($\text{N}\cdot\text{m}^{-1}$)
k^t	Torsional stiffness ($\text{N}\cdot\text{m}\cdot\text{rad}^{-1}$)
K_{\max}	Maximum Stiffness ($\text{N}\cdot\text{m}^{-1}$)
K_A	Application factor (-)
$K_{H\alpha}$	Transverse load factor (contact stress) (-)
$K_{F\alpha}$	Transverse load factor (root stress) (-)
K_v	Dynamic factor (-)
$K_{H\beta}$	face load factor (contact stress) (-)
$K_{F\beta}$	Face load factor (root stress) (-)
l_i^s	Length of a single line of contact (-)
L	Load (N)

L^s	Sum of the lengths of the lines of contact (-)
L_C	End relief length (mm)
m	Gear module (mm)
M	Moment (N·m)
p_0	Maximum value of the Hertzian pressure (GPa)
p_b	Base pitch (mm)
p_m	Average value of the Hertzian pressure (GPa)
ρ_{fp}^*	Root radius factor (-)
q'	Minimum value for the flexibility of a pair of meshing teeth ($\text{mm} \cdot \mu\text{m} \cdot \text{N}^{-1}$)
r	Pitch radius (mm)
r_a	Addendum radius (mm)
r_b	Base radius (mm)
R_X	Radius of curvature along the axial direction of the gear (mm)
R_Y	Radius of curvature along the radial direction of the gear (mm)
\mathcal{R}	Load sharing ratio for a spur gear at $\xi = 0$ (-)
T	Torque (N·m)
TE	Transmission Error (rad)
TI^s	Trim function (-)
u_t	Specific total tooth potential energy ($\text{J} \cdot \text{N}^2$)
U_a	Axial Compressive Energy (J)
U_b	Bending energy (J)
U_s	Shear energy (J)
U_t	Energy (J)
UI^s	Unbounded contact line length ratio (-)
V	Shear Load (N)
ω	Angular velocity ($\text{rad} \cdot \text{s}^{-1}$)
x_i	Profile shift coefficient of gear i (-)
y	Coordinate along the tooth centerline with origin at the gear rotation center (m)
y_C	Coordinate at load section (m)
y_f	Fillet-foundation compliance (m)
y_H	Contact compliance (m)
y_p	Coordinate at tooth root section (m)
z	Number of teeth (-)
z_n^i	Virtual number of teeth of gear i (-)
Z_s	Depth of the maximum Hertzian shear stresses (μm)
γ	Angle between the points T1 and A on the pinion rotation center (rad)
γ_b	Tooth angular thickness at base radius (rad)
γ_C	Tooth angular thickness at load radius (rad)
γ_p	Tooth angular thickness at root radius (rad)
$\gamma(y)$	Tooth angular thickness at section y (rad)
ϕ	Angle between the points T1 and B on the pinion rotation center (rad)
ϕ_1	Angle between the points A and B on the pinion rotation center (rad)
φ	Angular displacement (rad)

Subscripts

1..9	General numbering
I	Reference face
II	Nonreference face
g	gear
hb	Upper bound
lb	Lower bound
p	pinion

Superscripts

'	Single-flank single-pair tooth contact
---	--

List of Figures

2 Gear Mesh Stiffness

2.1	Relevant tooth geometry parameters for the PEM	11
2.2	Non solid disk gear parameters	18
2.3	Full gear model	21
2.4	Gear body model with several teeth	21
2.5	One tooth sector model	22
2.6	Three teeth sector model	22
2.7	Mesh stiffness distribution of an healthy gear.	25
2.8	Experimental setup	26
2.9	ξ coordinate	29
2.10	Heaviside function approximation	29
2.11	Curves for the α_k evolution with ε_α	34

3 Gear Geometry and Simulation Landscape

3.1	End relief profile modification schematic	41
3.2	Crowning profile modification schematic	41
3.3	Osculating cylinders	43
3.4	Free body diagram of the torsional model of the gear pair	46

4 Simulation preparation and setup

4.1	Overall workflow schematic	50
4.2	Tip alteration adjustment	51
4.3	Profile modification selection	51
4.4	Profile modifications window	52
4.5	Gear trimming schematic	52
4.6	Different refined region configurations employed	54
4.7	Schematic of the gear tooth partitioning	54
4.8	Initial and last stages of the tooth preparation process	55
4.9	Final configuration of the assembly	55
4.10	Location of the most common convergence problems	56
4.11	3D model geometry	57
4.12	Boundary conditions	58
4.13	Appropriate joint setup	58
4.14	Named selections	59
4.15	Pinion referential selection	59
4.16	Pinion referential	60

4.17	Symmetry plane	61
4.18	Displacements along the Z direction	61
4.19	Displacements along the Z axis on the symmetry plane	62
4.20	Contact Details	63
4.21	Contact Selection	64
4.22	Body mesh convergence study	67
4.23	Refined mesh convergence study	67
4.24	Substep number study	68
4.25	Torque value study	68
4.26	Mesh Details	69
4.27	Edge sizings applied to generate the mesh	70
4.28	Final mesh configuration on the pinion	72
4.29	Different partitions into which the geometry is divided	73
4.30	Additional partition added through revolution	73
4.31	Refined region mesh	74
4.32	Influence of the bias factor on the aspect ratio	75
4.33	Von-Mises Stress distribution on the initial models in MPa	76
4.34	Von-Mises Stress distribution on the final models	76
4.35	Analysis settings	78
4.36	Assigning values of torque and rotation speed	79
4.37	Meshing schematic	80
4.38	Abnormal distortion of the mesh	81
4.39	Relative rotation probe details for the pinion	81
4.40	Preserved body of the gear with 60 teeth	82
4.41	Structural error of the body of the gear with 60 teeth	83
4.42	Model with a refined region intersecting the central partition section	83
4.43	refined region modification	84
5	Results and Discussion	
5.1	Schematic for the coordinate shift	88
5.2	Numerical results of the M4_5 model	89
5.3	Normalized mesh stiffness of the M4_5 model	89
5.4	Numerical results of the ER1 model	90
5.5	Normalized mesh stiffness of the ER1 model	90
5.6	Torque along the X, Y and Z directions for the initial simulation	91
5.7	Contact status of the initial simulation of the ER1 model	91
5.8	Torque along the X, Y and Z directions for the refined simulation of the ER1 model	92
5.9	Contact status of the refined simulation of the ER1 model	92
5.10	Numerical results of the ER2 model	93
5.11	Normalized mesh stiffness of the ER2 model	93
5.12	Numerical results of the ER1M45 model	94
5.13	Normalized mesh stiffness of the ER1M45 model	94
5.14	Influence of the geometrical parameters on the α_k parameter	97
5.15	Influence of the contact ratio on the α_k parameter	97
5.16	Variation of the α_k parameter with the contact ratio in terms of \mathcal{R}	99
5.17	Different curves for the determination of α_k	100

B Transmission Error and Mesh Stiffness Curves

B.1	Numerical results of the M1_75 model	111
B.2	Normalized mesh stiffness of the M1_75 model	112
B.3	Numerical results of the M2_5 model	112
B.4	Normalized mesh stiffness of the M2_5 model	113
B.5	Numerical results of the M4_5 model	113
B.6	Normalized mesh stiffness of the M4_5 model	114
B.7	Numerical results of the M8 model	114
B.8	Normalized mesh stiffness of the M8 model	115
B.9	Numerical results of the M12 model	115
B.10	Normalized mesh stiffness of the M12 model	116
B.11	Numerical results of the PROFI11 model	116
B.12	Normalized mesh stiffness of the PROFI11 model	117
B.13	Numerical results of the PROFI12 model	117
B.14	Normalized mesh stiffness of the PROFI12 model	118
B.15	Numerical results of the PROFI21 model	118
B.16	Normalized mesh stiffness of the PROFI21 model	119
B.17	Numerical results of the PROFI22 model	119
B.18	Normalized mesh stiffness of the PROFI22 model	120
B.19	Numerical results of the PROFI31 model	120
B.20	Normalized mesh stiffness of the PROFI31 model	121
B.21	Numerical results of the PROFI32 model	121
B.22	Normalized mesh stiffness of the PROFI32 model	122
B.23	Numerical results of the I2 model	122
B.24	Normalized mesh stiffness of the I2 model	123
B.25	Numerical results of the I3 model	123
B.26	Normalized mesh stiffness of the I3 model	124
B.27	Numerical results of the C20 model	124
B.28	Normalized mesh stiffness of the C20 model	125
B.29	Numerical results of the CORR1 model	125
B.30	Normalized mesh stiffness of the CORR1 model	126
B.31	Numerical results of the CORR2 model	126
B.32	Normalized mesh stiffness of the CORR2 model	127
B.33	Numerical results of the K01 model	127
B.34	Normalized mesh stiffness of the K01 model	128
B.35	Numerical results of the K02 model	128
B.36	Normalized mesh stiffness of the K02 model	129
B.37	Numerical results of the ER1 model	129
B.38	Normalized mesh stiffness of the ER1 model	130
B.39	Numerical results of the ER2 model	130
B.40	Normalized mesh stiffness of the ER2 model	131
B.41	Numerical results of the ER1M45 model	131
B.42	Normalized mesh stiffness of the ER1M45 model	132
B.43	Numerical results of the CR1 model	132
B.44	Normalized mesh stiffness of the CR1 model	133
B.45	Numerical results of the CR2 model	133
B.46	Normalized mesh stiffness of the CR2 model	134

This page was intentionally left blank.

List of Tables

2	Gear Mesh Stiffness	
2.1	Advantages and disadvantages of numerical models	9
2.2	Advantages and disadvantages of analytical models	9
2.3	Advantages and disadvantages of approximated analytical models	9
2.4	Coefficients for the application of Eq. 2.38.	14
2.5	Coefficient values for the flexibility calculation	17
3	Gear Geometry and Simulation Landscape	
3.1	Parameter values for the simulated gears.	40
3.2	End relief parameters	40
3.3	Crowning parameters	41
3.4	Contact ratio values for the simulated gears.	42
3.5	Relevant geometric features of the C20 gear.	43
5	Results and Discussion	
5.1	Relevant values of the stiffness distributions for the simulated models.	95
5.2	Coefficients for the approximations for the first set of numerical points.	98

This page was intentionally left blank.

Chapter 1

Introduction

1.1 Motivation

The recent rise in electrical vehicle mobility calls for a development in all the areas that concern them. An electric vehicle, EV, may share some requisites with internal combustion engine, ICE, vehicles given that they both aim to solve the same main problem, but the differences between these technologies are far too great not to be acknowledged. In EV applications, motors typically rotate at a much faster rate than an ICE. Furthermore, the lower weight of the EV, the higher its possible range, making light weight construction a necessity in order to make the range of an EV competitive with that of an ICE powered vehicle. This creates the need for optimization in the multiple aspects of the drivetrain and structure of an EV.

The electric motors are far more silent than the ICE and therefore unable to mask the noise produced in the transmission. The fact that the EV have a lighter construction also leads to fewer layers and lower robustness when it comes to isolating vibrations produced in the transmission and are the source of the aforementioned noise [1]. In fact, EVs are heavier mainly due to the battery. Improvements can be achieved with a proper gear design, aiming to reach a constant mesh stiffness throughout the contact path [2].

The improvement that is expected greatly motivates the work that will be developed throughout the document and the author hopes that it will benefit those who are currently or will at some point study or work in the area. This work will feed data towards the calibration of an approximated analytical model for the calculation of the gear mesh stiffness of parallel axis spur gears.

1.2 Main Goal

One of the goals of this work is to develop a process to establish the dependence of the gear mesh stiffness with the main geometric parameters that define a gear. Through a parametric study conducted with FEA resources and an adequate parameter selection,

this work also aims to provide the last necessary data to complete analytical expressions that allow, with less time and effort, the determination of the absolute stiffness at a given point throughout the path of contact. In the future, this may help reducing the necessary time to design gears for EV automotive transmission (although this is not limited to this sector) optimized for smoothness of operation and efficiency. The vibrational problems are related with the gear mesh stiffness and its variation with time. The meshing dynamic can only be properly studied when the gear meshing is also adequately calculated. Knowing the gear dynamic can lead to the mentioned smoother, lighter and more efficient transmissions, possibly through optimization algorithms. As the efficiency is closely related to the autonomy of an EV, it is a topic of high importance [3–7].

The obtained results will calibrate an analytical model that far out speeds a FEM. The analytical model can easily be subjected to an optimization algorithm and quickly determine the most efficient gear with the lowest mesh stiffness variation, which is the main cause of the problems this work is aiming to solve. Finally, an analytical model, when appropriately validated, can be superior to FEA: simulations with durations exceeding half a day will become unnecessary.

1.3 Outline

In this Section, the contents of the remaining Chapters of this document are summarized.

Chapter 2 - To introduce the topic, a brief history of the evolution of the gear is presented in this chapter, followed by the presentation of the concept of the gear mesh stiffness and some example models for its calculation, along with the approximated analytical model that motivated this work and the method used in ISO 6336-1.

Chapter 3 - The main geometrical parameters that may influence the quantities that are being studied in this work are presented here. The matrix where all the models in study are presented also contemplates how the presented parameters will vary. The Hertzian contact model is also presented and applied to the contact of gear teeth.

Chapter 4 - In this chapter, the whole process of the practical part is presented. From the geometry definition to the FEA part, the main steps towards achieving the results are described.

Chapter 5 - The results and their respective discussion are included here. Abnormal results and the influence of the input parameters are evaluated here to reach the conclusions that will follow.

Chapter 6 - In this final chapter, some conclusions about the obtained results are exposed to summarize the information that this work provided. Based on these conclusions, some future works are proposed in order to follow up the work done thus far regarding this topic.

Chapter 2

Gear Mesh Stiffness

In this chapter, a brief history of the evolution of the gear is presented, alongside the presentation of the concept of the gear mesh stiffness and some example models for its calculation. The approximated analytical model that motivated this work and the method used in ISO 6336-1 are presented with more detail due to their importance regarding the work at hands.

2.1 Brief History

Literature has no definitive information regarding the origin of gears. It is not known who first used gears or started their development. It is speculated that the first versions of gears were made from wooden disks and used in farm work or to ladle water. The first literature regarding the subject dates about 2300 years ago, written by Aristotle, *Subject on Machine* [8].

Nonetheless, the gear history goes way back. Several machines, deriving from Hellenistic sources, such as Archimedes, Ctesibius, Philo of Byzantium and others, were described by Vitruvius. His descriptions included machines for engineering structures (hoists, cranes and pulleys) and war machines (ballistae, catapults and siege catapults). The more detailed descriptions covered, among others, [8]:

- dewatering devices;
- raising water and dewatering machines to irrigate fields and drain mines, speculated to be based on Archimedes' works, although not mentioned;
- water clocks and sundials;
- surveying and measuring instruments (diopeters, chorobates such as water levels) and odometers;
- lifting machines, such as endless chains of buckets and reverse overshot water wheels;

- aqueducts and inverted siphons;
- a steam engine named aelopile, which was conceived as an experiment to demonstrate the nature of atmospheric air motions;
- a water mill named after the author of these descriptions in a vertical configuration which outperformed the horizontal one in terms of efficiency.

It is worth noting that these machines did not pose a worthy novelty. Instead, they preserved construction details, which could be traced back. Another big step in gear history was achieved thanks to the widely known genius, Leonardo da Vinci. Several sketches drawn by Leonardo da Vinci, about 500 years ago, contemplated almost all the varieties of gear that are used nowadays [8].

His contributions regarding mechanisms that involved gears were countless, but some main ones, as a term of comparison with the previous mentioned, are [8]:

- lifting equipment: winches, cranes and mechanical jacks using different gear drives;
- buckets for underwater works, fans and helicoidal impellers;
- excavators and dredges for port works and channels;
- printing presses with an automatic device;
- clockwork mechanisms;
- mechanisms that allowed a continuous rotation motion to be turned into an intermittent motion;
- measuring instruments of the same categories as aforementioned;
- friction wheels, flywheels and cam actuated levers;
- a speed gear where a lantern-pinion could be meshed with three spur gear wheels and allowed all of them to have different diameters;
- a small car driven by pedal or sprint system, a chariot with a transmission system to all the four wheels and a self-propelled chariot driven by a spring system;
- a rear axle with differential;
- a helical motion propulsion system, which would become an ancestor of today's helicopter.

The importance of such contributions for the mechanical engineering is undeniable. Furthermore, the importance of these systems for the evolution of the gear is equally beyond doubt.

Many of these machines used previously known types of gears, but Leonardo da Vinci proposed new types that could be considered novelties. The bevel gear pair, where the bevel is a crown wheel, the worm gear pair, where the worm has a toroidal shape, cylindrical helical gears and a double worm gear mechanism are the types of gears he introduced [8].

It is also stated that Leonardo da Vinci knows the kinematics of the helicoidal motion, being the first one to describe it. Additionally, the tooth profile shape was also a concern he kept in mind, as he understood it had an importance in terms of gear transmission. He made use of his vast knowledge not only for civil and mechanical engineering problems, but also for belic purposes. It's undeniable that war instigated many developments in the gearing sector [8].

Later on, the laws of gearing are established. For a given position and transmission function, in the most general case of axes arrangement in the Euclidian three-dimensional space, the laws of gearing were formulated as [8]:

- **First law of gearing:** A unique relationship exists between the instantaneous displacement of the output member and the instantaneous displacement of the input member;
- **Second law of gearing:** A unique relationship exists between the spiral angle and the pressure angle at the contacts between conjugate surfaces in order to provide motion transmission as defined by the first law of gearing;
- **Third law of gearing:** The conjugate action requires a unique effective curvature at the contacts that satisfy the second law of gearing.

The topic of the tooth profile became more prominent, having already been introduced. Hawkins stated that the involute profile had considerable advantages when compared to the widely adopted profile at that time, the cycloid profile [8].

The involute profile allowed a perfect kinematic operating mode, allowed more than one pair of teeth to contact at the same time, which lead to improvements in terms of mechanical strength and load carrying capacity and, under the same operating conditions, the rolling velocity increased and the sliding velocity decreased, leading to a slide/roll-ratio with almost half the value [8].

The involute profile would then become increasingly more popular, as it was superior to the cycloid profile regarding [8]:

- adjustability;
- uniformity of distribution of the pressure of contact;
- sliding friction and efficiency;
- thrusts on the bearings;
- mechanical strength and load carrying capacity.

As the knowledge regarding gears increased, so did the studies and researches concerning the topic. By the early 20th century, the concerns towards the gear teeth in action rose. The mechanical strength characteristics of materials, their manufacture and cutting processes in the teeth and production technologies of the gears became addressed problems [8].

These problems necessarily evolved in complexity, until the actual state of the art is reached. Dynamic analyses of the gears were gradually introduced, more and more advanced and complicated, to calculate more accurately the dynamic loads, also as a function of the dynamic transmission error, or in order to take account of specific influences, or still to achieve predetermined goals. Some of these goals can be listed as studying [8]:

- periodic excitation, as for example the one related to step changes in mesh stiffness, due to the change from single pair to double pair tooth contact;
- transient excitation, for example the one related to different types of transmission and/or manufacturing errors, some of which with random distributions;
- different types of gear, including cylindrical spur and helical gears, bevel and spiral bevel gears, crossed-axes gears, worm gears and hypoid gears or even various type combinations;
- areas of application, namely aerospace, automotive, industrial gearing, gears for marine applications, etc.;
- speed regions, i.e., subcritical, main resonance, and supercritical speed ranges;
- vibratory behavior, in terms of modal shapes and related frequencies, and noise control;
- acoustics of cavity and comfort control, etc.

The problem that motivates this dissertation, gear mesh stiffness, is also one of the main topics on which gear technology focuses on, nowadays.

2.2 Mesh Stiffness

Fundamentally, the concept of stiffness establishes the resistance manifested by a body to a deflection caused by a given load. The simplest way of expressing is through the analysis of a linear system with a single degree of freedom, DOF, such as a linear spring, where the stiffness, k is given by the ratio between the applied load, L , and the resulting displacement from its application, δ , as stated in Eq. 2.1 [9].

$$k = \frac{L}{\delta} \quad (2.1)$$

In more realistic scenarios, systems will likely have more than one DOF. In such cases, for a system with n DOFs, the stiffness is defined as a square matrix of order n . Each element of the k matrix, k_{ij} , can be obtained by the relation established in Eq. 2.2, which is a ratio between the load applied in the DOF i , L_i and the resulting displacement in the DOF j , δ_j [9].

$$k_{ij} = \frac{L_i}{\delta_j} \quad (2.2)$$

Once the concept of stiffness is established, it can be adapted to gear mesh stiffness with the appropriate adjustments. Similarly, the gear mesh stiffness also establishes a relation between a load that must be applied on the gear mesh to produce a given displacement. However, in the gear meshing process, several deflections occur during the loading process. First, the Hertzian deflection occurs at the contact point on the profile, which is then transmitted to the body, causing bending, shear and compression deflections. When the load reaches the tooth root, it is transferred to the adjacent parts until it eventually reaches the gear body. If it is strained, there may exist an angular tooth deflection with respect to the gear center. The concept that immediately follows this line of thought is the Transmission Error, TE , which is represented by the difference between the theoretical position of the unmodified, geometrically perfect and infinitely rigid gears and their actual position. As such, it is the relative displacement of the gear with respect to the pinion (output with respect to the input) and can be mathematically expressed, in its angular form, as presented in Eq. 2.3 [9] :

$$TE = \theta_2 - \frac{r_{b1}}{r_{b2}}\theta_1 \quad (2.3)$$

where θ_1 and r_{b1} are the rotation angle and base radius, respectively, of the pinion and θ_2 and r_{b2} are the rotation angle and base radius, respectively, of the gear. The angular form of the TE can be converted into its linear form by multiplying both sides of Eq. 2.3 by r_{b2} , which translates into a displacement along the line of action. There are two types of transmission, which apply to the working conditions: static transmission error and dynamic transmission error. Since the transmission error itself is a displacement caused by a load, it can be related to the gear mesh stiffness. The gear mesh stiffness can be either linear or torsional, as well as converted between both. The torsional mesh stiffness, k^t , corresponds to the ratio between the applied torque, T , and the angular transmission error, established in Eq. 2.4. Likewise, the linear mesh stiffness, k^l is given by the ratio between the applied load, L , and the linear transmission error, δ , established in Eq. 2.5 [9].

$$k^t = \frac{T}{TE} \quad (2.4)$$

$$k^l = \frac{L}{\delta} \quad (2.5)$$

Stiffness is related, by definition, to elastic deflections. Therefore, the no-load transmission error, which is associated with manufacturing errors, must be removed from the transmission error when calculating the associated gear mesh stiffness since it is associated to a rigid-body motion and not elastic deflection. Nonetheless, the no-load transmission error must be taken into account when a gear pair is modeled, given its impact on the system's behavior. As said, and recalling that $T = L \cdot r_b$ and the Eqs. 2.4 and 2.5, the torsional and linear mesh stiffness are intrinsically related, with the relationship denoted in Eq. 2.6 [9]:

$$k^t = \frac{T}{TE} = \frac{L r_{b2}^2}{TE r_{b2}} = \frac{L}{\delta} r_{b2}^2 = k^l r_{b2}^2 \quad (2.6)$$

The gear mesh stiffness plays a crucial role in today's technology. Two sectors that have seen a rise in the importance of this problematic are electric vehicles (EVs) and polymer gears. Electric vehicles are currently a sector in ascension due to industrial and environmental reasons and, consequently, have seen an increase in production volume over the last few years. There are common drivetrain configurations that can be found in electric vehicles:

- in small EVs, the electric motor (low/average speed motor) is typically attached directly to the wheels;
- for EVs with the objective of replacing the internal combustion engine vehicles, the electric motor (high speed motor) is coupled to a transmission.

The high-speed motors typically work between 8900 and 16 000 rpm. However, it is expected that this value will eventually reach 30000 rpm. This will completely change the design requirements for the majority of the parts that make up the drivetrain. The modeling of the gear mesh stiffness will also require adjustments to account for an increase in already existing effects and other effects that may appear, such as Hertzian dampening, extension of contact, loss of contact, centrifugal expansion, manufacturing errors, teeth friction, precession and gyroscopic effects. Some models already consider some of these effects, but there isn't currently a model that includes all of the ones mentioned or even the majority of them. [9].

To give the reader insight on the state of the art, some models for the determination of the gear mesh stiffness will be presented, however without great detail.

2.3 Mesh Stiffness and Load Sharing Models

Tables 2.1 to 2.3 summarize the main advantages and disadvantages of the different methods to obtain the gear mesh stiffness. These are not the only advantages and disadvantages to take into account when deciding which way to choose in order to address this problematic, but rather the main aspects that should be the first focus of such decision.

Table 2.1 Advantages and disadvantages of numerical models [9].

Advantages	Disadvantages
Geometry freedom	Long simulation times
Models may contain several types of elements depending on the desired output	Most commercial softwares require licences, which may be costly
Great Accuracy	Always contain some numerical error

Table 2.2 Advantages and disadvantages of analytical models [9].

Advantages	Disadvantages
Higher modeling efficiency	Need for calibration
Greatly reduced time to produce results	Very complex phenomena may be extremely difficult to describe analytically
Only type of models capable of providing exact results	Frequently require the need for simplifications that are non-realistic
Rely on expressions already established by the mechanics of materials	

Table 2.3 Advantages and disadvantages of approximated analytical models [8].

Advantages	Disadvantages
Lowest computational cost of all the model natures	They involve approximations and therefore, cannot provide exact results
Possibility to undergo iterative processes of optimization	May also require calibration until they can replace other methods
They provide simple and direct expression to describe complex phenomena that would otherwise require high numerical computation	

2.3.1 Potential Energy Method

The Potential Energy Method is strictly analytic and there are several ways to implement it and calculate the numerous parameters on which it depends. Only some of them

will be presented here. This method establishes, through the superposition of different effects, the gearmesh stiffness as a time varying parameter which reflects the meshing conditions as the number of teeth pairs in contact changes. It is greatly dependent on tooth geometry, the position of the contact point, tooth deflections, tooth profile errors, the torsional deflection of the gear hub and local defects on the tooth [9,10]. Eq. 2.7 establishes the total potential energy, U_t , as a combination of the potential energy associated with bending, U_b , shear, U_s , and axial compression, U_a . Eqs. 2.8, 2.9 and 2.10 show how each of these strain energies is calculated [9].

$$U_t = U_b + U_s + U_a \quad (2.7)$$

$$U_b = \int \frac{M^2}{EI} dy \quad (2.8)$$

$$U_s = \int \frac{C_f V^2}{2A_c G} dy \quad (2.9)$$

$$U_a = \int \frac{F_c^2}{2A_c E} dy \quad (2.10)$$

where E is the modulus of elasticity of the material, M represents the bending moment, calculated according to Eq. 2.11 [9],

$$M = F_N \cos(\alpha_C)(y_C - y) \quad (2.11)$$

I is the second moment of area, calculated through Eq. 2.12 [9],

$$I = \frac{be^3(y)}{12} \quad (2.12)$$

C_f is the correction factor, assuming the value of 1.2 for rectangular cross sections, V is the shear load, calculated through Eq. 2.13 [9],

$$V = F_N \cos(\alpha_c) \quad (2.13)$$

A_c is the area of the cross section, calculated through Eq. 2.14 [9],

$$A_c = be(y) \quad (2.14)$$

G is the transverse modulus of elasticity of the material and F_c is the compressive load, calculated through Eq. 2.15 [9].

$$F_c = F_N \sin(\alpha_C) \quad (2.15)$$

From the definitions shown in Eqs. 2.11 to 2.15, Eqs. 2.8 to 2.10 can be rewritten as shown in Eqs. 2.16, 2.17 and 2.18 [9]:

$$U_b = 6 \frac{F_N^2 \cos^2(\alpha_C)}{Eb} \int_{y_p}^{y_C} \frac{(y_C - y)}{e^3(y)} dy \quad (2.16)$$

$$U_s = 0.6 \frac{F_N^2 \cos^2(\alpha_C)}{Gb} \int_{y_p}^{y_C} \frac{dy}{e(y)} \quad (2.17)$$

$$U_a = \frac{F_N^2 \sin^2(\alpha_C)}{2Eb} \int_{y_p}^{y_C} \frac{dy}{e(y)} \quad (2.18)$$

y_p and y_C , the integration limits, correspond to the values of y at the fixed boundary of the tooth and the load section. The fixed boundary is located at the chordal tooth root line and the load section is located at the intersection between the line of action and the tooth centerline. To better understand these geometrical parameters, Fig. 2.1 shows their location on the tooth geometry [9]. To define the geometrical parameters in terms of the

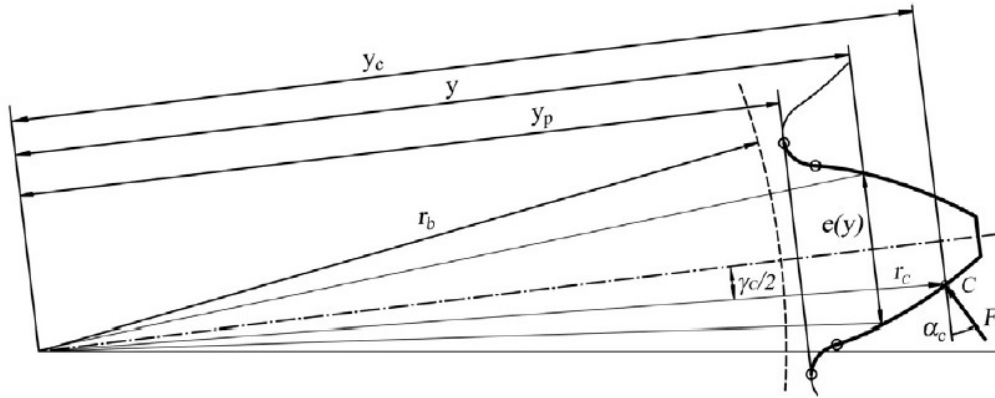


Figure 2.1 Relevant tooth geometry parameters for the PEM [11].

load point, a normalized coordinate, ξ_C , can be defined as stated in Eq. 2.19 [9].

$$\xi_C = \frac{\overline{TC}}{p_b} = \frac{\sqrt{r_C^2 - r_b^2}}{\pi m \cos(\alpha)} \quad (2.19)$$

It is calculated as the ratio between the curvature radius at the load point C , \overline{TC} and the circular base pitch, p_b [9]. The load angle can be defined by Eqs. 2.20 to 2.22 [9]:

$$\alpha_C = \alpha_T - 0.5\gamma_C \quad (2.20)$$

$$\alpha_T = \arccos\left(\frac{r_b}{r_C}\right) \quad (2.21)$$

$$\gamma_C = 2 \left(\frac{s}{d} + \text{inv}(\alpha_t) - \text{inv}(\alpha_T) \right) \quad (2.22)$$

where s is the tooth thickness at the pitch radius, d represents the pitch diameter, inv is the involute of the argument angle and α_t is the transverse pressure angle. Reworking Eq. 2.20 allows it to be rewritten as stated in Eq. 2.23 [9],

$$\alpha_C = \frac{\pi}{z}\xi_C - \frac{\pi}{2z} - \frac{2x \tan(\alpha)}{z} - \text{inv}(\alpha_t) \quad (2.23)$$

where x is the profile shift coefficient. The tooth chordal thickness, $e(y)$, can be defined as a function of the angular thickness of the tooth, $\gamma(y)$, as shown in Eq. 2.24. The angular thickness of the tooth is defined on Eq. 2.25.

$$e(y) = 2r(y) \sin\left(\frac{\gamma(y)}{2}\right) \quad (2.24)$$

$$\gamma(y) = \gamma_b - 2v(y) \quad (2.25)$$

In the angular thickness expression, $v(y)$ represents the polar angle of the profile. This angle is measured from the radius of the involute start point at the base circle and can be visually interpreted from Fig. 2.1. Eqs. 2.26 and 2.27 show how to calculate the limits of integration [9].

$$y_p = r_p \cos(\gamma_p) \quad (2.26)$$

$$y_C = \frac{r_b}{\cos(\alpha_C)} \quad (2.27)$$

In these equations, γ_p is the angular thickness of the tooth at the root radius and r_p is the tooth root radius. Based on the assumption that the load-deflection relationship is linear, the strain energy and stiffness can be linked through the expression in Eq. 2.28 [9]:

$$U = \frac{L^2}{2k} \quad (2.28)$$

where U is the total potential energy of the system, which is the single tooth. L is the total load applied in that same system, which in this case is the tooth normal load, represented by F , and k is the system's stiffness. Once again, in this case, it represents the single tooth's stiffness. The total potential energy for a single tooth, U_t , can be transformed into the specific total tooth potential energy, u_t , as shown in Eq. 2.29 [9]:

$$U_t = U_b + U_s + U_a = \frac{F^2}{2} u_t \quad (2.29)$$

This shift is done by taking out $\frac{F^2}{2}$ out of each individual term and highlighting u_t . Finally, Eq. 2.28 can be rewritten as Eq. 2.30 by employing the changes in Eq. 2.29 in order to establish the relation between the single tooth stiffness and the specific total potential energy:

$$k^{st} = \frac{1}{u_t} \quad (2.30)$$

The stiffness of a single tooth is obtained, but the entire system is made of more than a single tooth. The gear mesh stiffness contemplates, at least, one pair of teeth in contact. As such, the contact stiffness must be taken into account. The contribution of the gear body to the tooth deflection must also be considered, in the form of fillet-foundation stiffness. For the first additional contribution, the contact compliance, y_H , three approaches can be considered: an approximate Hertzian and compression approach, which originates from the Hamilton Standard [9], calculated through Eq. 2.31 [9],

$$y_H \approx \frac{4F}{\pi b} \left[\left(\frac{1 - \nu_1^2}{E_1} \right) + \left(\frac{1 - \nu_2^2}{E_2} \right) \right] \left(1 + \frac{\pi}{4} \right) \quad (2.31)$$

a semi-empirical approach developed by Palmgren [9], defined by Eq. 2.32,

$$y_H = \frac{1.275F^{0.9}}{E_{12}^{0.9}b^{0.8}} = \frac{4(1 - \nu^2)F}{\pi E_{12}b} \left(1.10 \frac{b^2 E_{12}}{F} \right)^{0.1} \quad (2.32)$$

where $E_{12} = \frac{1}{2} \left(\frac{1}{E_1} + \frac{1}{E_2} \right)$, and finally a closed form approach developed by Weber [9], which can be calculated as stated in Eqs. 2.33 and 2.34,

$$y_H = \frac{2F}{\pi b} \left[\left(\frac{1 - \nu_1^2}{E_1} \right) \left\{ \ln \frac{2\bar{h}_1}{b_H} - \left(\frac{\nu_1}{2(1 - \nu_1)} \right) \right\} + \left(\frac{1 - \nu_2^2}{E_2} \right) \left\{ \ln \frac{2\bar{h}_2}{b_H} - \left(\frac{\nu_2}{2(1 - \nu_2)} \right) \right\} \right] \quad (2.33)$$

$$b_H = \left\{ \frac{4F}{\pi b} \left[\left(\frac{1 - \nu_1^2}{E_1} \right) + \left(\frac{1 - \nu_2^2}{E_2} \right) \right] / \left[\frac{1}{\rho_1} + \frac{1}{\rho_2} \right] \right\} \quad (2.34)$$

where b_H is the halved Hertzian contact width, \bar{h}_1 and \bar{h}_2 are the distances on the pinion, 1, and gear, 2, between the point of contact and the tooth centerline along the line of action and ρ_1 and ρ_2 are the radii of curvature of the pinion and gear, respectively. From the definition of stiffness and compliance, the Hertzian contact stiffness can be calculated from Eq. 2.35 [9].

$$k_H = \frac{F}{y_H} \quad (2.35)$$

An improved expression to calculate the contact compliance can be developed including the ones presented in Eqs. 2.31 to 2.33. This new expression, presented in Eq. 2.36, corroborates with finite element simulations and overcomes some inadequacies shown by the previous expressions [9].

$$y_H = \left[\ln \left(\left(1 + \sqrt{1 + \frac{1}{k^2}} \right) \bar{k} \right) - \frac{0.429}{1 + \sqrt{1 + \frac{1}{k^2}}} \right] \left[\frac{b_H^2}{4} \left(\frac{1}{\rho_1} + \frac{1}{\rho_2} \right) \right] \quad (2.36)$$

In this novel expression, \bar{k} is introduced and represents the datum depth in the normal direction, normalized in respect to half Hertz contact. The most common fillet-foundation compliance analysis is based a theory applied for circular elastic rings. The expression Eq. 2.37 for the fillet-foundation compliance depends on h and θ_p , which are the ratio between the tooth root radius and the bore hole radius and the angle between the tooth centerline and the junction with the root circle, respectively.

$$y_f = \frac{F \cos^2 \alpha_C}{E \cdot b} \left\{ \mathbf{L}^* \left(\frac{u_p}{S_p} \right)^2 + \mathbf{M}^* \left(\frac{u_p}{s_p} \right) + \mathbf{P}^* \left(1 + \mathbf{Q}^* \tan^2 \alpha_C \right) \right\} \quad (2.37)$$

with L^* , M^* , P^* , Q^* being functions that depend on h and θ_p , α_C being the load angle, u_p being the distance along the tooth centerline measured from the tooth root to the loading tooth section and s_p being the tooth root thickness [9]. Under the assumption of plain strain conditions, these functions, leading to Eq. 2.38 [9].

$$X_i^*(h, \theta_p) = \frac{A_i}{\theta_p^2} + B_i h^2 f_i + \frac{C_i h}{\theta_p} + \frac{D_i}{\theta_p} + E_i h + F_i \quad (2.38)$$

where h is defined as stated in Eq. 2.39

$$h = \frac{r_p}{r_B}, \quad (2.39)$$

The constants A_i through F_i are defined in Table 2.4.

Table 2.4 Coefficients for the application of Eq. 2.38.

	$A_i \times 10^5$	$B_i \times 10^3$	$C_i \times 10^4$	$D_i \times 10^3$	E_i	F_i
$L^*(h, \theta_p)$	-5.574	-1.9986	-2.3015	4.7702	0.0271	6.8045
$M^*(h, \theta_p)$	60.111	28.100	-83.431	-9.9256	0.1624	0.9086
$P^*(h, \theta_p)$	-50.952	185.50	0.0538	53.300	0.2895	0.9236
$Q^*(h, \theta_p)$	-6.2042	9.0889	-4.0964	7.8297	-0.1472	0.6904

The fillet-foundation stiffness can be calculated in a similar way, as stated in Eq. 2.40 [9].

$$k_f = \frac{F}{y_f} \quad (2.40)$$

The single tooth pair mesh stiffness is given by Eq. 2.41, not taking into account correction factors that some works include [9]:

$$k^{tp} = \frac{1}{\left(\frac{1}{k_1^{st}} + \frac{1}{k_2^{st}} + \frac{1}{k_H} + \frac{1}{k_{f1}} + \frac{1}{k_{f2}} \right)} \quad (2.41)$$

The gear mesh stiffness is obtained by adding the single tooth pair mesh stiffness of all

gear teeth pairs in mesh according to their position, as stated in Eq.2.42 [9].

$$k_{gm} = \sum_{i=1}^N k_i^{tp} \quad (2.42)$$

The gear mesh stiffness established here is one of the ways to determine the gear mesh stiffness of spur gears and is a solid basis for other implementations of the method. Besides the variety of procedures for spur gears, there are also different methods to calculate the gear mesh stiffness for helical gears which slightly diverge from the spur gear methodology [9].

2.3.2 Method B - ISO 6336-1-2006

Unlike Method A, which establishes tooth stiffness through an analysis that includes every individual influence, that can be done through direct measurements and incorporate values obtained through FEM or based on the theory of elasticity, this method is based on studies of solid disc spur gears and their elastic behavior [12]. As is usual, the differences between the theoretical results and the measured results are mitigated through correction factors. Other correction factors are included to take into account changes in constructive solution (rims and webs), rack profiles and/or even extend it to helical gears [12].

A superposition of the single tooth mesh stiffness for all the teeth pairs in contact makes the development of an expression to calculate c_γ possible, having had its accuracy thoroughly measured *a posteriori*.

The stiffness parameters, c' and c_γ , calculated through this method, offer satisfactory accuracy for the calculation of the dynamic and face load factors and the determination of profile and helix modifications for gears when [12]:

- dealing with external gears;
- the rack profile is considered basic;
- dealing with spur gears or helical gears with an helix angle β that does not exceed 45° ;
- the gears in mesh are both made of steel;
- dealing with any gear blank design;
- the connection between the shaft and gear hub allow for the torque to be transferred and evenly spread around the circumference (achieved through interference or splined fitting or when the pinion is integral with shaft);
- the specific load, calculated through $\frac{F_t K_A}{b}$, is no less than $100 \text{ N} \cdot \text{mm}^{-1}$.

However, this method can be extended, contemplating approximations or including further auxiliary factors, to the following cases [12]:

- internal gears;
- gears made of a material other than steel and different material combinations;
- a shaft-hub assembly that does not necessarily follow the condition presented right above, for example, in cases where the connection between the hub and shaft is achieved through a fitted key;
- specific loads that are below the value specified in the parameters applicability conditions.

The overall parameter, maximum tooth stiffness per unit face width (single stiffness) of a tooth pair, c' , with acceptable average values when the conditions for its fairly accurate application are met, can be obtain through Eq. 2.43 [12].

$$c' = c'_{th} C_M C_R C_B \cos \beta \quad (2.43)$$

It is important to understand the importance and the role played by each member of the right hand side of the equation. The first one, the theoretical single stiffness c'_{th} , is applied to solid disc gears obtained through a basic rack profile. Its application to helical gears requires the calculation of its corresponding virtual spur gear, which can be done as expressed in Eq. 2.44. The theoretical single stiffness of that same virtual gear is then represented as c_{th} [12],

$$z_{ni} = \frac{z_i}{\cos^3 \beta} \quad (2.44)$$

This parameter can then be calculated from Eq. 2.45 [12],

$$c'_{th} = \frac{1}{q'} \quad (2.45)$$

where q' is the minimum value of the flexibility of a pair of teeth. As stiffness and flexibility are inversely proportional, it is logical to establish such relation: the maximum stiffness is necessarily inversely proportional to the minimum flexibility, as stated in Eq. 2.45. The minimum flexibility can be calculated from the Eq. 2.46 [12],

$$q' = C_1 + \frac{C_2}{z_{n1}} + \frac{C_3}{z_{n2}} + C_4 x_1 + \frac{C_5 x_1}{z_{n1}} + C_6 x_2 + \frac{C_7 x_2}{z_{n2}} + C_8 x_1^2 + C_9 x_2^2 \quad (2.46)$$

being C_1 through C_9 constant coefficients for a given range of several parameters regarding gear geometry, which also rules over the series progression in Eq.2.46. These constants and series progression apply to gears with a basic rack profile that manifests [12] :

- $\alpha_P = 20^\circ$;
- $h_{aP} = m_n$;
- $h_{fP} = 1.2m_n$;

- $\rho_{fP} = 0.2m_n$;
- $x_1 \geq x_2$;
- $-0.5 \leq x_1 + x_2 \leq 2.0$.

When the load ranges from $100 \leq \frac{F_{bt}}{b} \leq 1600 \text{ Nmm}^{-1}$, the deviations vary between -8% and $+5\%$. For such conditions, the coefficients are given in Table 2.5.

Table 2.5 Coefficient values for the flexibility calculation [12].

C1	C2	C3	C4	C5	C6	C7	C8	C9
0.04723	0.15551	0.25791	-0.00635	-0.11654	-0.00193	-0.24188	0.00529	0.00182

The factor that follows this parameter is C_M , which, as referred, takes into account measured values for solid gears to mitigate, as best as possible, the difference between those and the theoretical values obtained through calculation. Its value is $C_M = 0.8$ [12]. For different constructive solution, particularly gears with rims and webs, C_R , takes into account the added flexibility. For solid disc gears, it can be stated that $C_R = 1.0$. For non solid disc cases, such as gears with webs and rims, this value can be determined either through calculation or graphically. Both methods are consistent with one another and their differences do not exceed -1% to $+7\%$. The expression that allows the determination of this value through calculation goes as follows in Eq. 2.47 [12]:

$$C_R = 1 + \frac{\ln \frac{b_s}{b}}{5e^{\frac{s_R}{5m_n}}} \quad (2.47)$$

and is subjected to some boundary conditions [12]:

- for $\frac{b_s}{b} < 0.2$, the fraction must be take the value of 0.2
- for $\frac{b_s}{b} > 1.2$, the fraction must be take the value of 1.2
- for $\frac{s_R}{m_n} < 1$, the fraction must be take the value of 1

As an alternative, Fig. 2.2 shows the parameters than can be used to graphically determine this factor. The value is determined with an input of s_R , gear rim thickness, and b_s , central web thickness and the relevant curves can be consulted in [12]. Finally, C_B , the basic rack factor, includes the effects of the deviations from the basic rack profile of the gear. The standard basic rack profile mentioned here is the one defined in ISO 53. It can be calculated from Eq. 2.48 [12],

$$C_B = [1.0 + 0.5(1.25 - \frac{h_{fP}}{m_n})][1.0 - 0.02(20 - \alpha_{Pn})] \quad (2.48)$$

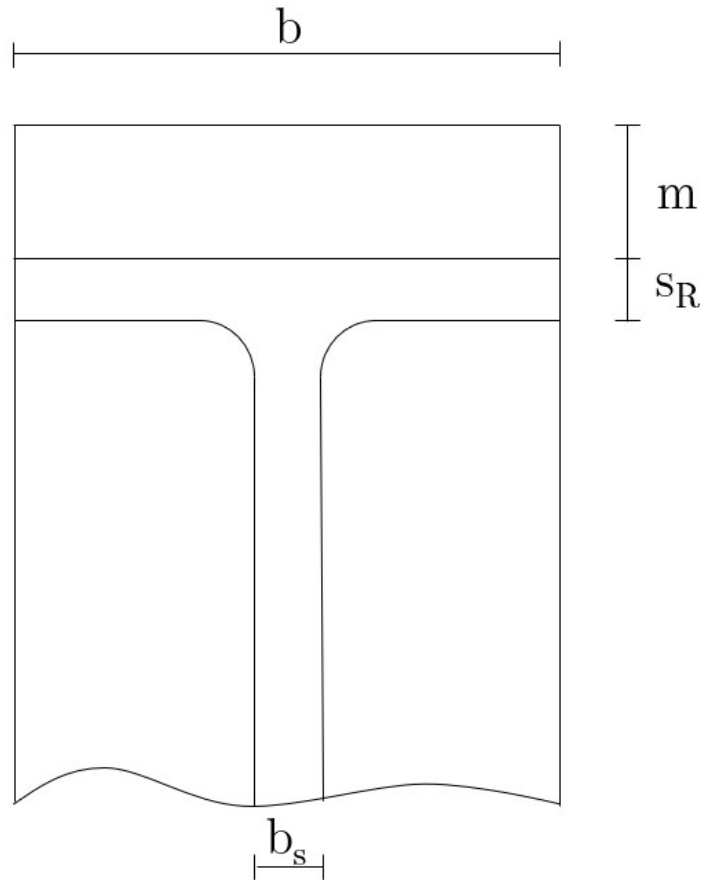


Figure 2.2 Non solid disk gear parameters [12].

and, in cases where the pinion basic rack dedendum does not match that of the wheel it is meshing with, a value corresponding to the arithmetic mean of the factor calculated for each of the gears, C_{B1} and C_{B2} , is used, calculated from Eq. 2.49 [12].

$$C_B = 0.5(C_{B1} + C_{B2}) \quad (2.49)$$

The final term, $\cos \beta$, transforms the theoretical single stiffness of the teeth of the virtual spur gear associated with a given helical gear from the normal into the transverse theoretical single stiffness of that same helical gear.

The extension of this method to internal gears can be easily achieved by replacing z_{n2} by ∞ in Eq. 2.46 [12].

The extension to materials other than steel also requires some modifications, being, in such cases, c' determined by Eqs. 2.50 and 2.51 [12]:

$$c' = c'_{St/St} \left(\frac{E}{E_{St}} \right) \quad (2.50)$$

where

$$E = \left(\frac{2E_1E_2}{E_1 + E_2} \right) \quad (2.51)$$

Given the most typical cases where this modification applies, common values can be presented here, where $\frac{E}{E_{St}}$ assumes a value of 0.74 in a steel/grey cast iron combination and a value of 0.59 in a grey cast iron/grey cast iron combination [12].

The way the gear and shaft are connected also requires further modifications when the first assembly condition presented earlier is not met, i.e., connection through fitted key. In such cases, the single stiffness, under constant load, varies between a maximum and minimum value twice per revolution. This minimum value can be approximated to the value of the single stiffness when the assembly is accomplished through interference or spline fits [12].

Press fitting one gear of a pair is press fitted onto a shaft with a fitted key and having the gear it meshes with mounted onto a shaft through interference or splined fitting leads to an average value of the single stiffness about 5% greater than the minimum value verified. However, when both gears are push fitted onto shafts with fitted keys, the average value of the single stiffness, relative to the minimum, increases to 10% [12].

Finally, a modification regarding lower values of the load is presented in Eq. 2.52, for cases where $\frac{(F_t K_A)}{b}$ is lower than 100 Nmm^{-1} [12]:

$$c' = c'_{th} C_M C_B C_R \cos \beta \left(\frac{F_t K_A}{100 b} \right)^{0.25} \quad (2.52)$$

When $\frac{(F_t K_A)}{b}$ is equal to or higher than 100 Nmm^{-1} , c' can be considered constant [12].

Up until now, single stiffness has been discussed and the conditions of its applicability. Now, regarding mesh stiffness, it is important to understand why it matters as much as it does. The mean value of mesh stiffness per unit face width, $c_{\gamma\alpha}$, is used for the calculation of the internal dynamic factor, K_v , and the transverse load factors $K_{H\alpha}$ and $K_{F\alpha}$ [12]. Respecting what was established from c' , $c_{\gamma\alpha}$ can be calculated from Eq. 2.53 [12],

$$c_{\gamma\alpha} = c' (0.75\varepsilon_\alpha + 0.25) \quad (2.53)$$

for spur gears with $\varepsilon_\alpha \geq 1.2$ and helical gears with $\beta \leq 30^\circ$. The mean value of mesh stiffness per unit face width, $c_{\gamma\beta}$, necessary for the calculation of the face load factors $K_{H\beta}$ and $K_{F\beta}$ and can be obtained from Eq. 2.54 [12],

$$c_{\gamma\beta} = 0.85c_{\gamma\alpha} \quad (2.54)$$

respecting the conditions that allow $c_{\gamma\alpha}$ to be determined beforehand.

2.3.3 Finite Element Models

This procedure has become increasingly popular as its accuracy allowed major experimental setups and major expenditures to be discarded. For structural analysis, FEM is a great resource to calculate displacements, stresses and deflections on loaded structures [9].

This method requires an appropriate discretization of the geometry by dividing the continuous domain of the problem into non-overlapped subdomains, known as finite elements. The connection between the elements is achieved through nodes and, together, they create a mesh that achieves said discretization. The solution for each element is obtained by the combination of the values at each node and assembling all the elements allows the problem to be solved. This method relies on the boundary and initial conditions imposed, without which a solution can not be found [9].

Being a numerical method, there are always inherent errors. However, they can be reduced as the modeling, both conceptually and structurally, becomes closer to depict the system's behavior. An appropriate element selection and the number of subdomains become determinant factors in the mitigation of the numerical errors [9].

This method allows complex geometries to be analyzed. Many complex boundary conditions, loading and material properties can also be handled, which proves the versatility of this method. The popularity of the method, alongside the versatility, comes from its high precision. However, such advantages come at a cost, which is the high computational effort that sometimes poses an inevitable obstacle [9].

Due to its precision, the finite element method is often used as validation of other techniques. In this work's context, its versatility makes it a very attractive tool to conduct analyses of the gear mesh stiffness in the presence of defects such as cracks, spalling and pitting. It also allows the study of the influence of geometrical parameters on the gear mesh stiffness and the study of gear mesh stiffness in a dynamic scope. Although these are the main applications concerning the gear mesh stiffness, other may exist, although not as featured in the current literature as the ones mentioned [9].

2.3.3.1 Typical implementations

There are many softwares that allow the analysis through FEM to be conducted. One of the most commonly used is ANSYS. There are also several approaches concerning the modeling of the meshing gears exist. The gear can be modeled, mainly, as [2, 13]:

- full gear, as exemplified in Fig. 2.3;
- gear body with a single or several teeth, as seen in Fig. 2.4;
- single tooth sector model, as shown in Fig. 2.5;
- three tooth sector model, as presented in Fig. 2.6.

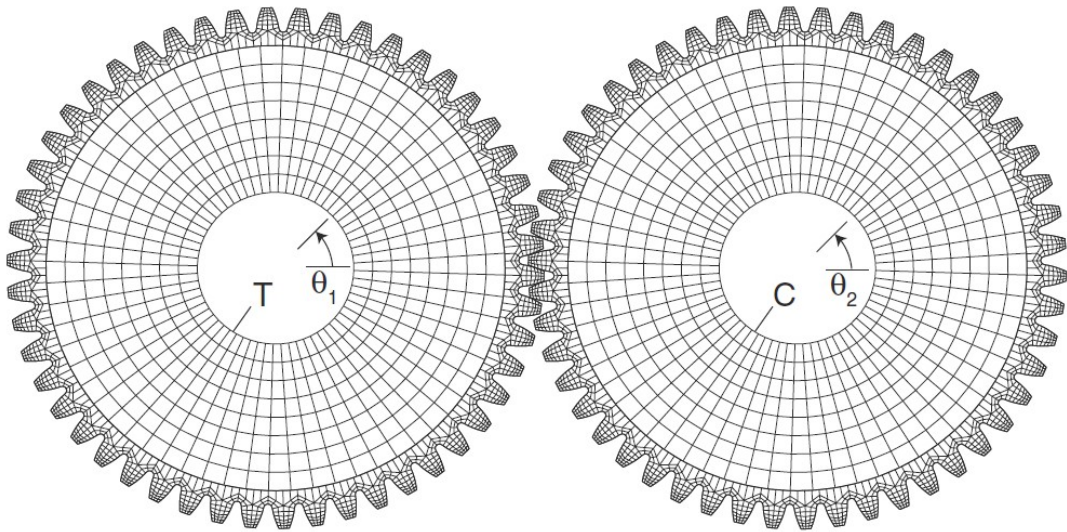


Figure 2.3 Full gear model [14].

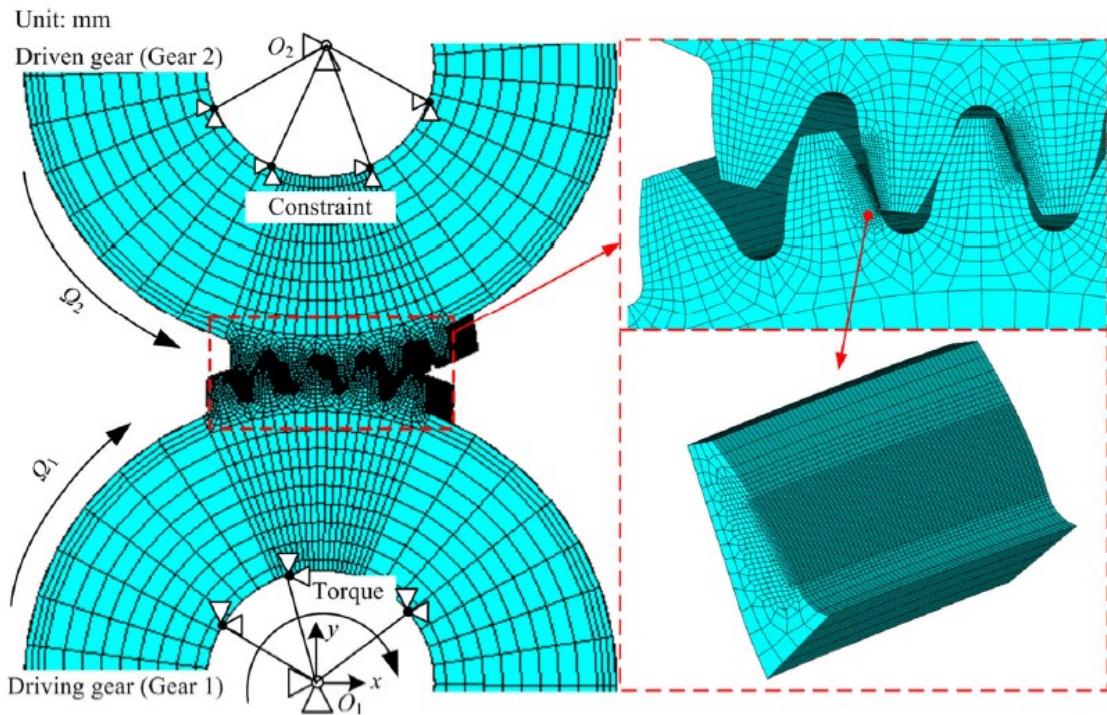


Figure 2.4 Gear body model with several teeth [15].

Several element types are used, but the number of elements also plays an important part in the implemented mesh.

The extraction of the mesh stiffness can be done in two different ways. The first one requires the extraction of the relative rotations of the input and output gears. The difference between both of them is the transmission error. From this quantity, the torsional gear mesh stiffness can be easily obtained. The second method requires the extraction of

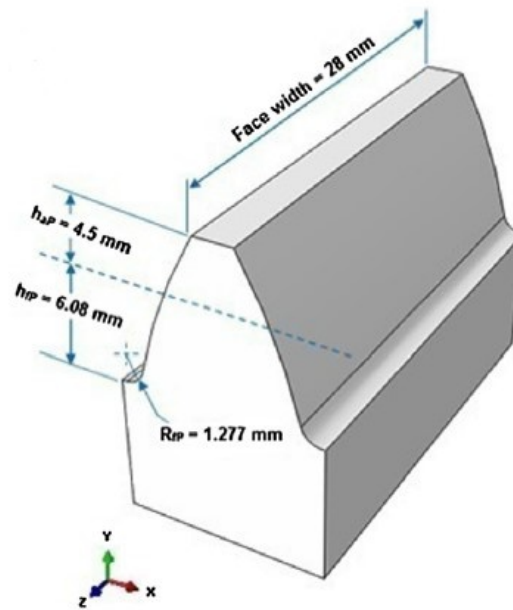


Figure 2.5 One tooth sector model [16].

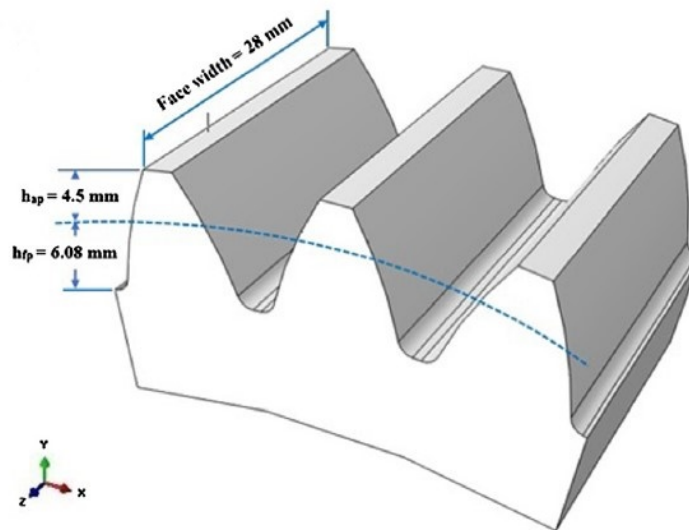


Figure 2.6 Three teeth sector model [16].

the deflection in the direction of the applied load. Necessarily, these quantities allow the determination of the linear gear mesh stiffness. However, as previously stated, the linear and torsional gear mesh stiffness can be easily related [9]. An implementation guideline is suggested in the works of Zhan et al. [17]. The techniques mentioned regarding the model can be used as a canvas to a personalized implementation, while always respecting the rules of the model's behavior through the many adjustable options offered. As mentioned, there are several ways to model a gear pair, but there are commonly adopted practices that lead to better outcomes and avoids, *a priori*, problems that researchers have already come across [9].

Finite Element Method based models are also used when studying polymer gears. Given how recent the topic is, FEM becomes a great tool to overcome the lack of analytical models to describe it, due to the method's versatility [9].

2.3.4 Hybrid Model

The main difference that this model introduces is the definition of a local rigid region in the vicinity of the contact in order to avoid unwanted and inaccurate local distortion caused by the concentrated force transmitted. This greatly simplifies the process of building the model, which is often a complex process, and raises its efficiency at calculating and outputting results [18].

First, a boundary condition is established to have the hub nodes behave in a rigid manner in relation to the gear and pinion geometric/rotation centers. The contact force is applied both in the gear and the pinion, in the contact node and its respective meshing node, along the line of action and, necessarily, opposing directions. This applied force, F_u , is unitary. The deflection verified at these nodes, caused by this applied force, includes not only the global deflection but also the local distortion which the authors aim to avoid/eliminate. Therefore, a local rigid area around the contacting nodes is created. Extensive testing has shown that the radius of this rigid area should be $0.2m$, where m is the module of the gear pair and its Young's modulus should be 1000 times bigger than that of the surrounding body [18].

For the contacting nodes, upon the consideration of the local rigid region, the global displacement vector U can be obtained from Eq. 2.55 [18],

$$U = K^{-1}F \quad (2.55)$$

where F is the global nodal force vector and K is the global stiffness matrix, where the local rigid area consideration is contemplated. To obtain the total displacements of each node, the displacements along the directions x and y can be used on Eq. 2.56 [18],

$$u = u_x \cos \alpha_n + u_y \sin \alpha_n \quad (2.56)$$

where u_x and u_y are the displacements along the x and y direction, respectively, and α_n is the operating pressure angle. It is assumed that the force moves along the tooth flank from the meshing starting point to the tooth tip while the gear pair is fixed. Since the force is unitary, the verified nodal displacement corresponds directly to the nodal compliance. From that relationship, when the load is applied on every node, the compliance matrix, in its rough form, can be obtained for the pinion, represented by λ^{Pr} . This matrix can be

written as stated in Eq. 2.57 [18],

$$\lambda^{Pr} = \begin{bmatrix} \lambda_{11} & \lambda_{12} & \cdots & \lambda_{1j} & \cdots & \lambda_{1N} \\ \lambda_{21} & \lambda_{22} & \cdots & \lambda_{2j} & \cdots & \lambda_{2N} \\ \cdots & \cdots & \cdots & \cdots & \cdots & \cdots \\ \lambda_{i1} & \lambda_{i2} & \cdots & \lambda_{ij} & \cdots & \lambda_{iN} \\ \cdots & \cdots & \cdots & \cdots & \cdots & \cdots \\ \lambda_{N1} & \lambda_{N2} & \cdots & \lambda_{Nj} & \cdots & \lambda_{NN} \end{bmatrix} \quad (2.57)$$

where N represents the number of nodes in which the pinion's tooth surface is discretized. The value λ_{ij} represents the nodal compliance of the i indexed node when the j indexed node has the unitary load F_u applied. Since the number of nodes in the tooth surface is limited, the accuracy of the interpolation matrix can be enhanced through interpolation, leading to the definition of a matrix λ^P which represents the pinion's compliance matrix. A similar approach allows the determination of the equivalent matrix for the gear, λ^G . For the load distribution and static transmission error analysis, a compatibility equation concerning the displacements can be written as stated in Eq. 2.58 ,

$$-(\lambda_c + \lambda_b)F_n + x_s = \varepsilon \quad (2.58)$$

where x_s is the static transmission error, ε is the initial separation clearance vector, which contains all the information concerning the separation distance, the initial assembly error and machining error. λ_b corresponds to the compliance matrix of all the potential contact points.

Both these quantities can be obtained from the matrices λ^P and λ^G , respectively. It is worth noting that the approach presented so far is based on a two-dimensional analytical FEM. This means that all the potential contact points are located on the tooth surface and the existence of potential contact points along the tooth width is discarded. The quantity λ_c , which contemplates the effects of the tooth contact, represents the nonlinear contact compliance matrix, also at all potential contact points, and can be written as follows in Eq. 2.59 ,

$$\lambda_c = \text{diag}(\lambda_{c1}, \lambda_{c2}, \dots, \lambda_{ci}, \dots, \lambda_{cN}) \quad (2.59)$$

where λ_{ci} can be obtained through Eq. 2.60 [18].

$$\lambda_{ci} = \frac{1.275}{E^{0.9} L^{0.8} F_i^{0.1}} \quad (2.60)$$

The contact compliance at potential contact point i , λ_{ci} is a function of the force at that same potential contact point i , F_i and the material's Young's modulus and face width, E and L respectively. Also in the compatibility equation, Eq. 2.58, F_n is the normal contact force vector at all potential contact points, being possible to express it as stated in Eq. 2.75 [18]

$$F_n = [F_1, F_2, \dots, F_i, \dots, F_n]^T, \quad F = \sum_{i=1}^n F_i, \quad (1 \leq i \leq n) \quad (2.61)$$

with F being the total contact force, calculated from Eq. 2.62 [18]

$$F = \frac{T}{r_{b1}} \quad (2.62)$$

with T being the applied torque and r_{b1} being the pinion's base radius [18].

2.3.4.1 Results and Conclusions

Fig. 2.7 shows the obtained results for the analyzed healthy gear, where the proposed method is the hybrid method implemented in reference [18]. There is also a comparison with a strictly based FEM approach and the PEM, which was explained earlier. The absolute values of the gear mesh stiffness are not relevant for the purpose with which this model was presented, but rather the shape of the curves and how they estimate the gear mesh stiffness, for comparison purposes [18].

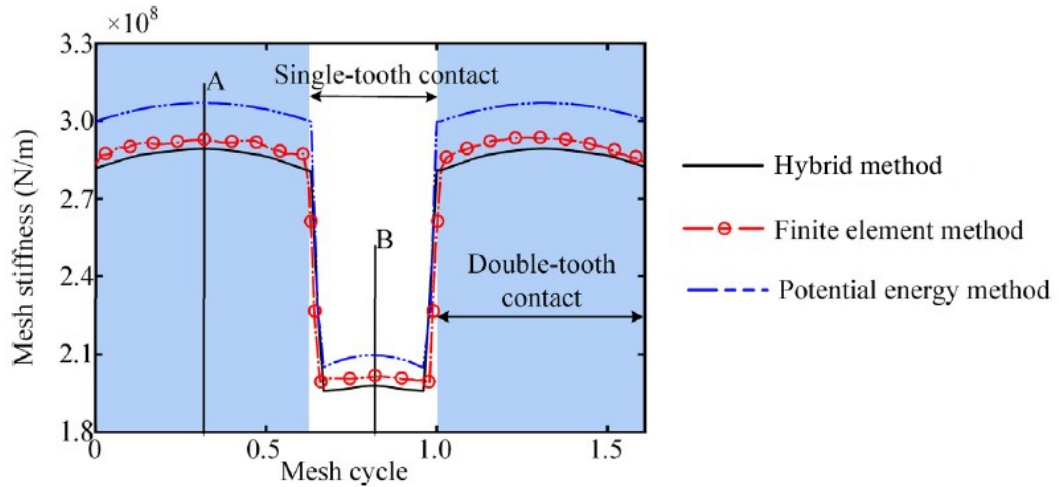


Figure 2.7 Mesh stiffness distribution of a healthy gear. Adapted from [18].

There is a fairly decent agreement between the three exposed methods, seeing that the values of the mesh stiffness do not vary significantly throughout the contact path and the parabolic shape of the curves is evident.

2.3.5 Experimental Determination of Gear Mesh Stiffness

This experimental model aims to accurately measure the stiffness of a single tooth, experimentally. The accuracy can be evaluated by comparison with the other presented models, for the same configurations of the gear pair. This technique also allows studies of the effect of the variation of the pressure angle on the single tooth stiffness, which

requires gear types that aren't manufactured by traditional methods, such as additive manufacturing and bimetallic forging [19]. This is only an example of a technique, as other experimental approaches can be seen in the literature, namely in works presented in [9].

2.3.5.1 Setup

A steel rigid body was mounted on the base with bolts. A force impactor with a load cell and a Linear Variable Differential Transformer were used in order to obtain all the required information to determine the Single Tooth Stiffness, load-wise and displacement-wise, respectively. The support structure was reinforced with welding and bolted connections in order to minimize any unwanted effects on the tooth elastic deflection. The heat-hardened steel force impactor had a rectangular cross section at its end and its contact with the sample had a thickness of 0.2 mm [19]. The experimental setup used is shown in Fig. 2.8. The forces applied ranged from 750 N to 1500 N, with an increment of 250 N

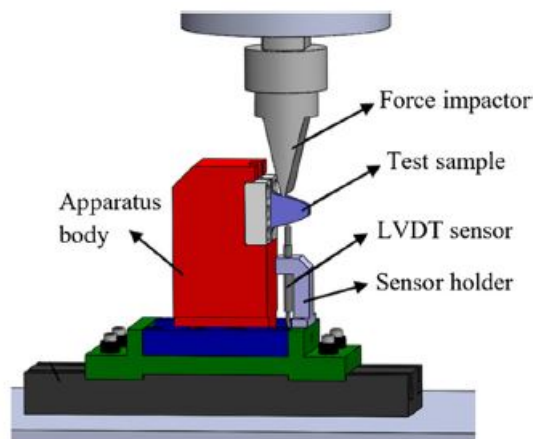


Figure 2.8 Experimental setup [19].

N [19]. This study involved both symmetric ($\alpha = 20^\circ$) and asymmetric ($\alpha = 25^\circ, 30^\circ, 35^\circ$) configurations. The asymmetric configurations kept the first tested pressure angle at the inferior flank, where the LVDT was located, and changed the pressure angle of the flank on which the force was applied. The samples were designed as a cantilever beam with an involute profile. The chosen material was 4140 steel which would undergo a surface hardening process to prevent submergence. The process chosen was induction heating based heat treatment: in this process, the samples were heated as quickly as possible to their austenitic temperature (ranging from 840°C to 870°C), followed by a quenching in oil. The resulting surface hardness ranged from 55 to 65 HRC among all the samples. To remove any possible quenching stresses, the samples were then tempered between 160°C and 200°C . This greatly reduces the risk of grinding cracks on the samples, which would invalidate the results and compromise the setup [19].

2.3.5.2 Validation through FEA

For the validation of the obtained experimental results, the authors of this test setup decided on a FEA approach. The first step was the generation of the CAD data of the samples, which was done with MATLAB and CATIA software. A fully rounded rack cutter was used to achieve the higher values of DSPA. As mentioned, the CSPA was kept constant at 20°. The CAD models were exported to ANSYS Workbench to initiate the meshing operation. The chosen elements were hexahedral and, for all cases in this study, mesh convergence tests were performed in order to make the finite element model/analysis as reliable as could be. The authors defined 280 000 elements as the converged mesh number for this study as a stabilization of the elastic deflection is denoted beyond that point. Following the suggestion from Coy [20], the grid near the point of loading was dimensioned according to Eq. 2.63 [19],

$$\frac{e}{b_h} = -0.2 \left(\frac{c}{e} \right) + 1.2, \text{ for } 0.9 \leq \frac{c}{e} \leq 3 \quad (2.63)$$

where c and e are, respectively, the length and width of the element and b_h is the Hertzian contact width. Doing so allows for the definition of the Hertzian part of the deflection, which is detrimental in contact problems such as the one being studied in this experimental setup and the one that motivates this thesis. The boundary conditions consisted of fully fixed surfaces representing the situation of the body of the gear being clamped to the rigid body with bolts and a force applied as described, with its value changed according to the range and increment also as specified above. A linear static analysis was chosen as the FEA type. The applied loads are constant, having no variation with time [19]. Finally, in order to validate both the experimental results and the results obtained through the FEA, expressions for the calculation of STS of spur gears with symmetric teeth, from Kuang and Lin's works, were used [19].

The expression for the STS goes as shown in Eq. 2.64 [19],

$$\bar{K}_i(r) = (A_0 + A_1 \cdot X_i) + (A_2 + A_3 \cdot X_i) \frac{(r - R_i)}{(1 + X_i) \cdot m} \quad (2.64)$$

where $\bar{K}_i(r)$ is the STS at a given r of the gear, $A_{0,1,2,3}$ are the empirical equations, X_i is the addendum modification coefficient, m is the gear modulus, R_i is the radius of the pitch circle and r is the radius of any point along the involute profile curve. All the empirical equations on which the STS definition presented relies on only depend on Z_i , which is the number of teeth, and can be written as shown in Eqs. 2.65 to 2.68 [19]:

$$A_0 = 3.867 + 1.612Z_i - 0.02916Z_i^2 + 0.0001553Z_i^3 \quad (2.65)$$

$$A_1 = 17.060 + 0.7289Z_i - 0.01728Z_i^2 + 0.0000999Z_i^3 \quad (2.66)$$

$$A_2 = 2.637 - 1.222Z_i - 0.02217Z_i^2 - 0.0001179Z_i^3 \quad (2.67)$$

$$A_3 = -6.330 - 1.033Z_i + 0.02068Z_i^2 - 0.0001130Z_i^3 \quad (2.68)$$

2.3.5.3 Results and Conclusions

Once again, it is experimentally determined that the gear mesh stiffness behaves according to a parabola. The STS of involute spur gears with symmetric (conventional) and asymmetric teeth is measured with a novel experimental method and a validation procedure is also presented [19].

This method makes it possible to analyze, experimentally, gears that are not produced by conventional design and manufacturing methods. These gears require, typically, difficult analytical calculations in order to verify the FE models established to determine their stiffness. On that note, the experimental measurement results were compared with FEA, analytically calculated from the literature and the STS results obtained from the experimental measurements were generally consistent with the FEA results [19].

With the increase in drive side pressure angle, the single tooth stiffness for involute spur gears increased nearly 38%. Numerical and analytical studies in the literature can be verified experimentally using the method developed and by using the developed FE model, the TVMS can be calculated [19].

2.4 Approximated Analytical Model

The approximated analytical model that will, later in the present work, undergo a calibration process, is going to be presented. The advantages of such approach have been discussed and the required values for calibration will be presented [2, 13]. These kinds of models bear some game changing advantages, such as being ideal to undergo iterations based optimization methods. These optimization methods may aim to minimize power losses or the variations of gear mesh stiffness throughout the whole meshing process [7].

2.4.1 Description on the length of the contact lines

This first model is based on the assumption that the load per unit of contact line length along the path of contact is constant. A coordinate ξ must be considered, being the non-dimensional coordinate along the path of contact and is obtained dividing the distance by the transverse base pitch, p_{bt} , shown in Fig. 2.9 [2, 13]. For spur gears, it is known that the length of the contact line over a teeth is constant. A teeth entering the plane of action can therefore be seen as a constant value increment in the function that describes the sum of the length of contacting lines, mathematically translated by a Heaviside function. The expression in Eq. 2.69 [2, 13],

$$H(\xi) = \lim_{k \rightarrow \infty} \left(\frac{1}{1 + e^{-2 \cdot k \cdot \xi}} \right) \quad (2.69)$$

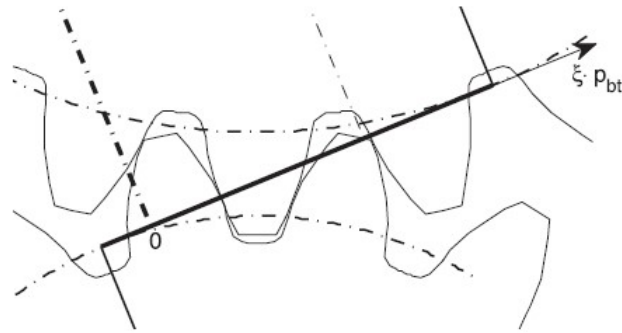


Figure 2.9 ξ coordinate [2, 13].

closely behaves in accordance to the theoretical Heaviside function, also known as the unit step function, for $k = 10000$, as Fig. 2.10 shows. Defining a trim function based on the

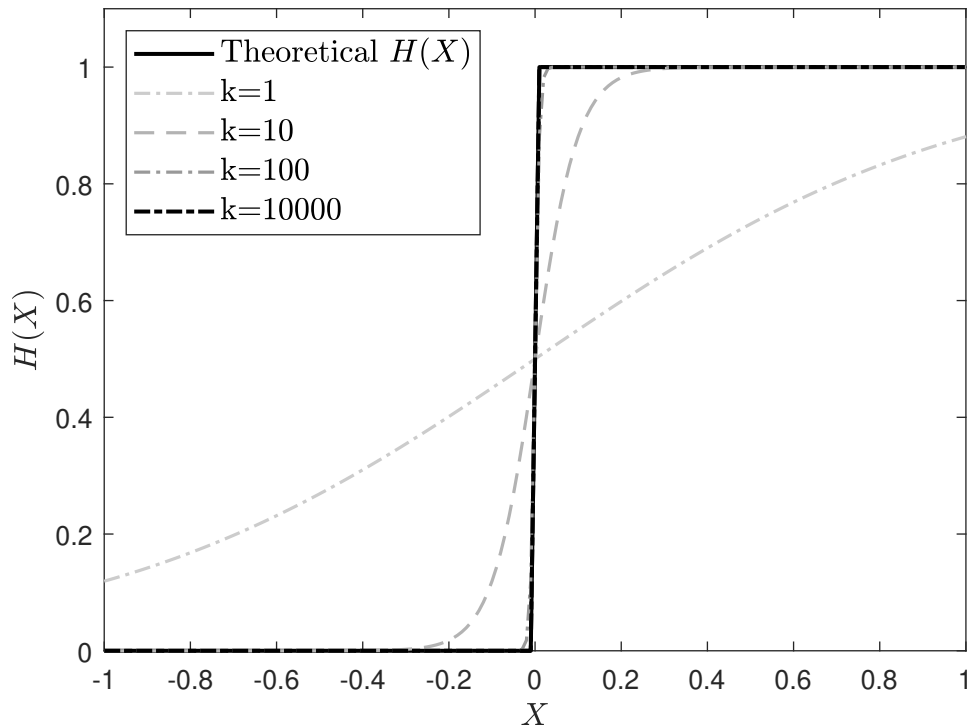


Figure 2.10 Heaviside function approximation [2, 13].

property that the ratio of length of the contact line over a tooth to the face width is always equal to 1 in the active section of the plane of action and 0 outside of it becomes necessary to discard the need to define independent domains for each pair entering or leaving the contact. This trim function, $Tl^S(\xi)$, has a unitary height and a width equal to ε_α and can be obtained through the subtraction of two Heaviside functions shifted by its width, as stated in Eq. 2.70 [2, 13],

$$Tl^S(\xi) = H(\xi) - H(\xi - \varepsilon_\alpha) \tag{2.70}$$

It is known that more than one pair of teeth may be in contact simultaneously. This information is stored in the ε_α value and the trimmed function must be adjusted to contemplate this possibility. The meshing pairs are always shifted by a transverse base pitch, p_{bt} , which corresponds to a single unit in the coordinate system defined earlier. To obtain the line length of the other meshing pairs, in action, it is now the trim function that must be shifted back and forth by integer values. This manipulation leads to an unbounded contact line length ratio, $Ul^S(\xi)$, defined in Eq. 2.71 [2, 13],

$$Ul^S(\xi) = Tl^S(\xi - i) = H(\xi - i) - H(\xi - \varepsilon_\alpha - i) \quad (2.71)$$

From the definition of both the coordinate system, ξ and the contact ratio, ε_α , the values of i can be computed in a way that

$$i = -\text{floor}(\varepsilon_\alpha) : 1 : \text{floor}(\varepsilon_\alpha) \quad (2.72)$$

where $\text{floor}()$ represents the action of rounding down a real number to its integer part [2, 13]. Since the length of the line of contact, for a given pair, should only be defined between the bounds 0 and ε_α in the ξ axis, the trim function, which is defined in that same domain, can be used to both trim and bound each of the $Ul_i^S(\xi)$ functions, as stated in Eq. 2.73 [2, 13]:

$$l_i^S = Ul_i^S(\xi) \cdot Tl^S(\xi), \quad \forall i \quad (2.73)$$

resulting in a function that represents the bounded contact line length to gear face width ratio, for a given tooth pair i in a spur gear. The application of the concept to all the meshing pairs leads to a sum that contemplates all the active ones, resulting in a function $L^S(\xi)$, defined by Eq. 2.74 [2, 13],

$$L^S(\xi) = \left[\sum_{-\text{floor}(\varepsilon_\alpha)}^{\text{floor}(\varepsilon_\alpha)} Ul_i^S(\xi) \right] \cdot Tl^S(\xi) \quad (2.74)$$

These equations can then be extended to helical gears, with the appropriate adjustments, which can be seen in detail in [2, 13]. With the concept defined on equations 2.74, the load per unit of length over a tooth can be obtained through Eq. 2.75 [2, 13]:

$$f_N(\xi) = \frac{M_w}{r_{bw}} \cdot \frac{1}{b \cdot L^S(\xi)} \quad (2.75)$$

If, in addition to the sum of the lengths, the concept of the length of each individual contact line for all active meshing teeth pairs, $l_i^s(\xi)$ is included, the normal load acting in a single tooth along the path of contact can be obtained through Eq. 2.76 [2, 13]:

$$F_{Ni}(\xi) = \frac{M_w}{r_{bw}} \cdot \frac{l_i^s(\xi)}{L^s(\xi)} \quad (2.76)$$

Eq. 2.76 can be viewed as a product between the load supported by a pair of contacting teeth and a load sharing function. The value of this load is $\frac{M_w}{r_{bw}}$ and the load sharing function is given by the length of the individual contact line divided by the sum of the lengths of the contacting lines for all the contacting pairs, for a certain position ξ along the defined referential [2, 13].

2.4.2 Quasi-static elastic model

This model is based on the assumption that, for a given position along the path of contact, the load per unit length, $f_N(\xi)$, over a line of contact for a single tooth/for a single i , is constant. This applies to a single tooth only, as the that quantity is not assumed to be the same among all the meshing tooth pairs, again, for a given position ξ [2, 13].

It is then assumed that the gear body, up to the base cylinder (the gear hub), is perfectly rigid and the displacement of that same base cylinder, when the gear is loaded, is very small ($d\theta$). Necessarily, it follows that the length of the arc corresponding to that same angular displacement can be approximated by a linear displacement δ_b , in the direction of the plane of action [2, 13].

Stiffness can be defined as the load divided by the displacement resulting from its application. In other words, stiffness can be seen as the necessary load to apply an unitary displacement. To keep the concept coherent, torsional stiffness establishes the relation between a torque and an angular displacement and linear stiffness establishes the relation between a force and a linear displacement. There is interchangeability among both of them but the relation must be respected. That being said, the total normal force in the transverse plane, F_{bt} , and the linear displacement δ_b are related through the linear stiffness $K^T(\xi)$ as the following expression as shown in Eq. 2.77 [2, 13].

$$\delta_b = \frac{F_{bt}}{K^T(\xi)} \quad (2.77)$$

If a teeth pair i is in contact, the load supported by that pair can be obtained multiplying the displacement δ_b by the stiffness of that same pair, $K_i(\xi)$, as done in Eq. 2.78 [2, 13].

$$F_{Ni}^K(\xi) = \delta_b \cdot K_i(\xi) \quad (2.78)$$

The load distribution for a spur gear in the normal plane can be obtained from Eq. 2.79 [2, 13],

$$F_{Ni}^K(\xi) = \frac{K_i(\xi)}{K_T(\xi)} \cdot F_{bn} \quad (2.79)$$

ISO 6336-1 [12], as discussed in 2.3.2, issues a method to calculate a maximum value of the single tooth mesh stiffness with an acceptable possible deviation error for a certain set of conditions. From there, one can define a function of the single tooth mesh stiffness per

unit of gear width according to Eq. 2.80 [2, 13].

$$K_i^u(\xi) = k_i^u(\xi) \cdot \frac{K_{max}}{b} \quad (2.80)$$

From the literature, the single tooth mesh stiffness, for spur gears, has shown an approximately parabolic/half-sine-wave behavior throughout the whole meshing period. Rincon combined Cai's suggestion, k^{Cai} with the ISO 6336-1 average mesh stiffness, K_m^{ISO} to obtain the single teeth pair mesh stiffness in Eq. 2.81 (for spur gears, naturally) [2, 13].

$$k^{Cai}(t) = \frac{1}{0.85\varepsilon_\alpha} \cdot \left[\frac{-1.8}{\varepsilon_\alpha^2} \cdot t^2 + \frac{1.8}{\varepsilon_\alpha} \cdot t + 0.55 \right] \quad (2.81)$$

Defining the minimum mesh stiffness, Eq. 2.82, according to a parameter α_k , which represents the fraction of the maximum stiffness at either $\xi = 0$ or $\xi = \varepsilon_\alpha$ [2, 13],

$$K_{min} = \alpha_k \cdot \frac{K_{max}}{b} \quad (2.82)$$

allows the unitary single tooth mesh stiffness to be expressed as stated in Eq. 2.83 [2, 13]:

$$k_i^u(\xi) = \frac{4(\alpha_k - 1)}{(\varepsilon_\alpha + \varepsilon_\beta)^2} \cdot (\xi - i)^2 - \frac{4(\alpha_k - 1)}{(\varepsilon_\alpha + \varepsilon_\beta)} \cdot (\xi - i) + \alpha_k \quad (2.83)$$

Fusing the concept of the definition of the contact line length with the single tooth mesh stiffness leads to Eq. 2.84.

$$kl_i^u(\xi, i) = Ul_s^i \cdot k_i^u \quad (2.84)$$

By superposition of effects, the normalised gear mesh stiffness for a spur gear, $Kl_s(\xi)$, can be calculated as stated in Eq. 2.85.

$$Kl_s(\xi) = \left[\sum_{i=-\text{floor}(\varepsilon_\alpha)}^{\text{floor}(\varepsilon_\alpha)} kl_i^u \right] \cdot Tl_s \quad (2.85)$$

Extending such procedure to helical gears can be done considering that an helical gear is made of a stack of infinitesimal spur gears, being stacked once subjected to a rotation that generates the β throughout the width. The worked equations and a more detailed explanation of this extension can be found in [2, 13].

2.4.3 Load sharing and the free parameter importance and determination

\mathcal{R} is the load sharing ratio for a spur gear at the start of the meshing process [13]. Literature currently suggests different values for this parameter. For a single slice of a

spur gear with $1 < \varepsilon_\alpha < 2$, for $\xi = 0$, it can be estimated according to Eq. 2.86,

$$\mathcal{R} = \frac{\alpha_k}{\left[\frac{4(\alpha_k-1)}{(\varepsilon_\alpha)^2} \cdot (1)^2 - \frac{4(\alpha_k-1)}{\varepsilon_\alpha} \cdot (1) \right] + \alpha_k} \quad (2.86)$$

which leads to a definition of α_k as stated in Eq. 2.87.

$$\alpha_k = \frac{4\mathcal{R}(\varepsilon_\alpha - 1)}{\varepsilon_\alpha^2(2\mathcal{R} - 1) - 4\mathcal{R}\varepsilon_\alpha + 4\mathcal{R}} \quad (2.87)$$

Sánchez et al. [11] introduced an approximation to the single teeth pair mesh stiffness based on a cosine function, Eq. 2.88, for spur gears. Manipulation towards achieving an expression in terms of the relevant parameter, α_k , leads to the expression

$$\alpha_k^{\text{Sanchez}} = \cos \left(\frac{\varepsilon_\alpha}{2} \left[\frac{1}{2} \left(1.11 + \frac{\varepsilon_\alpha}{2} \right)^2 - 1.17 \right]^{-\frac{1}{2}} \right) \quad (2.88)$$

This solution was validated by Sánchez et al. aswell through a model based on the minimization of the potential energy that was previously developed. The validation consisted on 3775 cases of different gear ratios, pressure angles and profile shift coefficients with the following ranges [13]:

- $20 < z < 100$;
- $18^\circ < \alpha_m < 25^\circ$;
- $-0.1 < x_i < +0.1$.

From the expression proposed, the value of $\mathcal{R} = 0.36$ can be found, which is very close to the other existing values. AGMA 925-A03 [13] suggests a value of 1/3, simulations done using KISSsoft lead to a value of about 0.43 and the model based on the potential energy method returned, as mentioned, a value of 0.36 [13]. Fig. 2.11 shows the different curves obtained for α_k for these scenarios. Naturally, the expressions are restricted by the conditions under which they are determined. They lack generality. These equations:

- yield negative values of α_k for a given range of $\varepsilon_\alpha < 1$;
- have a root on the denominator in the $0 < \varepsilon_\alpha < 1$ domain;
- do not depict an increase in α_k as ε_α decreases, which should happen, culminating in $\alpha_k = 1$ for $\varepsilon_\alpha = 0$.

This set of physical incoherences becomes the aspect that should be the focus of the investigation that follows the work done until the moment, on this matter [13].

The α_k parameter plays a decisive role in the estimation of the gear mesh stiffness, load sharing ratio and friction torque. Its value depends on several parameters that influence

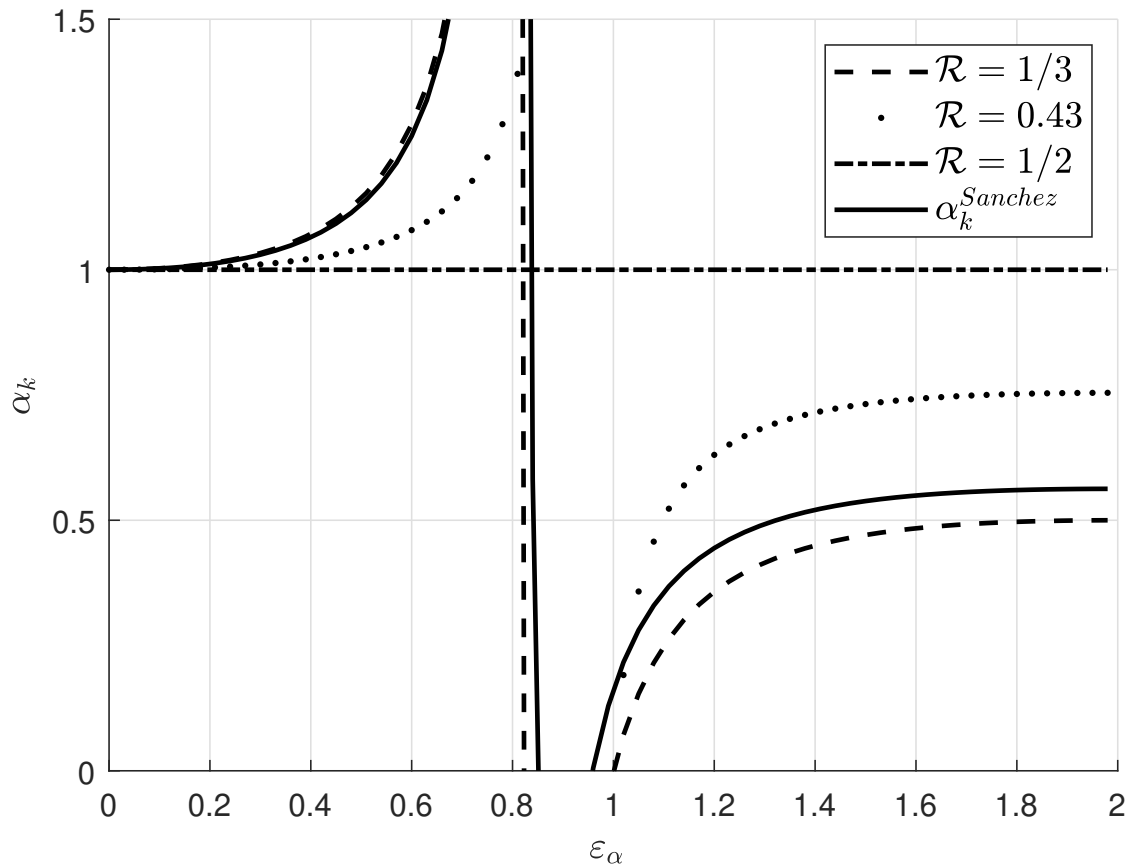


Figure 2.11 Curves for the α_k evolution with ε_α [13].

the gear geometry. A numerical model, based on works that can be consulted in [9], or with greater detail in [17] will be developed to estimate this parameter's variation with each of the geometrical parameters presented. The numerical model is, as mentioned, a way of addressing the problem and a choice was made to follow that path.

Chapter 3

Gear Geometry and Simulation Landscape

In this chapter, the main geometrical parameters that may influence the quantities that are being studied in this work are presented here. The matrix where all the models in study are presented also contemplates how the presented parameters will vary. The Hertzian contact model is also presented, applied to the contact of gear teeth. Finally, the torsional model that will allow the gear mesh stiffness to be obtained from the values of transmission error will be presented.

3.1 Geometric Parameters

Gear mesh stiffness depends on the gear geometry. In order to provide some background to the parametric study that will follow the theoretical part of this work, the geometric parameters that may influence the gear mesh stiffness and load sharing ratio will be presented.

3.1.1 Module

The module, represented by the parameter m , alongside with the number of teeth, z , defines the size of the gear. A gear pair may only mesh if and only if the modules of both individual gears match: otherwise, the meshing becomes impossible. It is a fundamental rule of gear technology. This quantity also corresponds to the length of the pitch diameter per tooth. Varying the module can be seen as a scaling of the gear, considering that most of its geometry is based on factors of this quantity [21].

Closely related to this parameter is the circular pitch, calculated from Eq. 3.1,

$$p = \frac{\pi d}{z} \tag{3.1}$$

which is the ratio of the pitch circle circumference and the number of the teeth. Its value represents the linear distance, along the pitch circle arc, between an arbitrary point and its counterpart on an adjacent tooth [21].

The circular pitch can also be obtained from Eq. 3.2.

$$p = \pi m \quad (3.2)$$

Equations 3.1 and 3.2 allow the conversion between both of these parameters, p and m . This is particularly interesting given that each parameter, even though both of them are major influences on gear size, dimensions the gear size with specific features. When a specific spacing between teeth is desired, the circular tooth is the parameter used to represent tooth size. In cases when a given feed is necessary or when designing position control systems, this parameter often assumes integer values or specific fractional values [21].

3.1.2 Pressure angle

The pressure angle is given by the angle between the line-of-action and a perpendicular line to a line that crosses both the gears centers. Alterations in the center distance result in a slight alteration of the value of this parameter; however, there is a relation that never changes between the base and pitch circles and the pressure angle, as Eq. 3.3 states [21]:

$$r_b = r \cos(\alpha) \quad (3.3)$$

When the center distance changes, so does the pressure angle, being α' the changed value as a consequence. The relation in Eq. 3.3 remains, but is adjusted as presented in Eq. 3.4 [21],

$$r_b = r' \cos(\alpha') \quad (3.4)$$

to contemplate the exact operating values.

3.1.3 Gear ratio and number of teeth

Gears' size ranges from a few millimeters to several meters. The size of the gears is established through the value of both the module and its number of teeth. If the module can be seen as a scaling of the whole gear, changing the number of teeth does not scale the teeth but rather the size of the remaining part of the gear, the hub and changes its shape, namely its curvature of the flank. This is one of the many properties that explain why this technology is so popular nowadays.

Power, that can be defined as stated in Eq. 3.5 [21],

$$P = T \cdot \omega \quad (3.5)$$

where T represents the torque and ω represents the angular velocity, allows the gear mechanisms to provide speed and torque according to the needs, keeping the product on the right-handed side of the expression in 3.5 constant. The first step towards the definition of the transmission ratio consists on relating the input and output powers as done in Eq. 3.6 [21].

$$P_1 = P_2 \equiv T_1 \cdot \omega_1 = T_2 \cdot \omega_2 \equiv \frac{T_1}{T_2} = \frac{\omega_2}{\omega_1} \quad (3.6)$$

From the pitch circles, one can determine the velocity ratio of gear 2 to gear 1 through the ratio of pitch diameters as seen in Eq. 3.7 [21],

$$i = \frac{d_1}{d_2} \quad (3.7)$$

The inverse of this quantity, given the power must be kept constant, represents the torque of gear 2 to gear 1. The gear ratio, or velocity ratio, can be defined in terms of number of teeth. Since, necessarily, $m_1 = m_2$ and $d = zm$, Eq. 3.7 can be rewritten as seen in Eq. 3.8 [21].

$$i = \frac{z_1 \cdot m}{z_2 \cdot m} = \frac{z_1}{z_2} \quad (3.8)$$

3.1.4 Tip alteration

Tip alteration contemplates the removal of material from the tooth addendum by an amount proportional to the modulus. This amount is known as the tip alteration factor, k . A positive factor can be seen as an addition of material relative to the standard profile, resulting in a thinner tooth thickness at the tip circle and a negative factor, in contrast, can be seen as a removal of material, which leads to a thicker tooth at the tip circle [21].

3.1.5 Profile

A single profile standard defines a specific set of parameters concerning the geometry of the tooth. The addendum corresponds to the proportion of material located above the pitch circle. The dedendum corresponds to the proportion of material located below the pitch circle. The normalized profiles typically include specific values of addendum factor, h_{ap} , dedendum factor, h_{fp} , root radius factor, ρ_{fp} , among other specifications. Once again, these factors are established in terms of the module. The way the addendum factor alters the tooth size is comparable to the tip alteration factor. However, the dedendum factor changes the distance between the root and pitch circles, shortening or extending the tooth on that metric. The root radius factor defines the tooth fillet radius according to the tooth modulus. A higher value leads to a thinner/smaller cross section area at the root of the tooth, which may play an important role in the load capacity of the tooth [21].

3.1.6 Profile Modifications

Profile modifications, which are basically intentional deviations from the involute tooth profile, are a commonly used resource to prevent excessive tooth load deflection interference and, consequently, improve load capacity. However, in the axial direction, the profile modifications may not change the chosen profile. The elimination of tip interference, through these alterations, reduces meshing noise. Some modifications also accommodate assembly misalignment towards preserving load capacity [21].

Crowning and side relieving are tooth surface modifications along the axial direction. Crowning consists on the removal of a slight amount of tooth from the center to the edge in order to make the surface slightly convex. This modification makes it possible for the gear to maintain contact in the central region of the tooth and avoid the lower load capacity of the edges, being more relevant in cases where the assembly of gears includes misalignment. Edge relieving is a modification that consists of a chamfering of the tooth surface near the edges. It does not change the nature of the contact. Therefore, it merely accomplishes the advantage that the crowning also provides regarding stress concentration at the gear edges but not misalignments [21]. The tip relief modification also changes the tooth flank and may greatly influence the mesh stiffness, mainly at the beginning and the end of the meshing. However, due to time limitations and the need to prepare each model from scratch, it is not included in this work.

3.1.7 Contact Ratio

The value of the contact ratio is determinant on the smoothness and continuity of the meshing by guaranteeing a pair of teeth begins contacting before another one ceases its own contact. This parameter is a measure of the meshing overlap, calculated as the ratio between the length of the line of action and the base pitch, as follows in Eq. 3.9 [21]:

$$\varepsilon_\alpha = \frac{\overline{AB}}{p_b} \quad (3.9)$$

For the case of spur gears, this expression can be rewritten to directly contemplate geometric parameters of the gear pair,

$$\varepsilon_\alpha = \frac{\sqrt{(r_{a1}^2 - r_{b1}^2)} + \sqrt{(r_{a2}^2 - r_{b2}^2)} - a \sin(\alpha)}{p_b} \quad (3.10)$$

Also known as normalized contact length, this value, ε_α , must always be greater than 1 in order to ensure that there is no gap between the initiation of contact in A and the release of contact in B, which would lead to an acceleration of the driving gear and shock when the contact is resumed. It is widely adopted, for parallel axis spur gears, to keep this value above 1.2 and it should never drop below 1.1 when all the tolerances are considered to be at their worst-case values [21].

A contact ratio between 1 and 2 means that during meshing, there are periods when two pairs are in contact and only one pair is in contact. Similarly, a ratio between 2 and 3 means that two or three pairs of teeth are always in contact. Usually, such a high contact ratio is not obtained with external spur gears. Nonetheless, it is possible to reach these values through specially designed nonstandard external spur gears [21].

3.2 Parameter Matrix

The first step towards conducting the parametric study is the appropriate definition of the parameters to be studied and their values. The chosen parameters are the ones that impact the gear tooth the most and even its size, resulting in a wide variety of geometries. The values adopted for each parameter were chosen according to ISO 53. Table 3.1 summarizes the parameters of each model studied, highlighting the changes relative to the standard geometry adopted, M4_5. Aside from the value of the module, m , and the axial distance, a , every other parameter is dimensionless.

Table 3.1 Parameter values for the simulated gears.

Gear	z_1	$i = \frac{z_2}{z_1}$	x_1/x_2	m /mm	α	a /mm	k	ρ_{fp}^*	h_{ap}^*	h_{fp}^*	Profile Modif.
M4_5(Ref.)	20	1	0/0	4.5	20	90	N/A	0.38	1.00	1.25	N/A
M1_75	20	1	0/0	1.75	20	35	N/A	0.38	1.00	1.25	N/A
M2_5	20	1	0/0	2.5	20	50	N/A	0.38	1.00	1.25	N/A
M8	20	1	0/0	8	20	160	N/A	0.38	1.00	1.25	N/A
M12	20	1	0/0	12	20	240	N/A	0.38	1.00	1.25	N/A
I2	20	2	0/0	4.5	20	135	N/A	0.38	1.00	1.25	N/A
I3	20	3	0/0	4.5	20	180	N/A	0.38	1.00	1.25	N/A
K0.1	20	1	0/0	4.5	20	90	+0.1	0.38	1.00	1.25	N/A
K0.2	20	1	0/0	4.5	20	90	+0.2	0.38	1.00	1.25	N/A
PROFI11	20	1	0/0	4.5	20	90	N/A	0.38	1.10	1.25	N/A
PROFI12	20	1	0/0	4.5	20	90	N/A	0.38	1.20	1.25	N/A
PROFI21	20	1	0/0	4.5	20	90	N/A	0.38	1.00	1.35	N/A
PROFI22	20	1	0/0	4.5	20	90	N/A	0.38	1.00	1.45	N/A
PROFI31	20	1	0/0	4.5	20	90	N/A	0.20	1.00	1.25	N/A
PROFI32	20	1	0/0	4.5	20	90	N/A	0.25	1.00	1.25	N/A
C20	20	1	0.1766/0.1766	4.5	20	91.5	N/A	0.38	1.00	1.25	N/A
CORR1	20	1	0/0.3532	4.5	20	91.5	N/A	0.38	1.00	1.25	N/A
CORR2	20	1	-0.1000/0.4532	4.5	20	91.5	N/A	0.38	1.00	1.25	N/A
ER1	20	1	0/0	4.5	20	90	N/A	0.38	1.00	1.25	End Relief 1
ER2	20	1	0/0	4.5	20	90	N/A	0.38	1.00	1.25	End Relief 2
ER1M45	20	1	0/0	4.5	20	90	N/A	0.38	1.00	1.25	End Relief 1
CR1	20	1	0/0	4.5	20	90	N/A	0.38	1.00	1.25	Crowning 1
CR2	20	1	0/0	4.5	20	90	N/A	0.38	1.00	1.25	Crowning 2

It is known that, even though care was put into changing only one parameter at once to avoid crossover effects, underlying quantities, such as the contact ratio, may suffer from these changes. It is then important to investigate whether possible changes are a result of the parameter that was directly changed or rather a consequence of the change in the underlying parameters associated with such direct definition. Table 3.4 summarizes the contact ratios for each of the models presented in Table 3.1. In the recent theories, summarized in [9], it is always implied that α_k depends on the contact ratio alone. Some of these will be presented later on, but these values will be presented here for consistency of the provided information.

The axial profile modifications are exemplified in Figs. 3.1 and 3.2 and their values are presented in Tables 3.2 and 3.3.

Table 3.2 End relief parameters. [22]

End Relief	Type	L_{CI} / μm	L_{CII} / μm	$C_{\beta I}$ /mm	$C_{\beta II}$ /mm
1	Linear	100	100	0.2	0.2
2	Linear	200	200	0.2	0.2

Some of the proposed gears share the same value of contact ratio. This happens because the parameter that was directly changed has no influence on this underlying parameter. However, this becomes advantageous to determine whether its the parameter that was purposely changed that determines the behavior of α_k or the parameters that

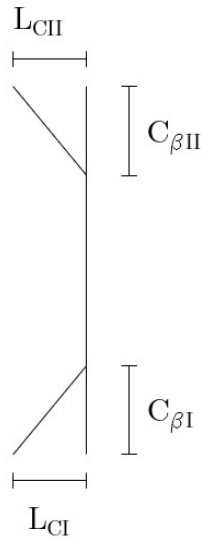


Figure 3.1 End relief profile modification schematic [22].

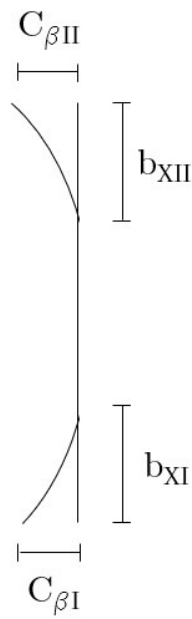


Figure 3.2 Crowning profile modification schematic.

Table 3.3 Crowning parameters. [22]

Crowning	$C_{\beta I} / \mu\text{m}$	$C_{\beta II} / \mu\text{m}$	$b_{XI/II} / \text{mm}$
1	100	100	$b/2$
2	200	200	$b/2$

were indirectly altered.

Table 3.4 Contact ratio values for the simulated gears.

Gear	ε_α
M4_5(Ref.)	1.557
M1_75	1.557
M2_5	1.557
M8	1.557
M12	1.557
I2	1.635
I3	1.671
K01	1.621
K02	1.811
PROFI11	1.686
PROFI12	1.811
PROFI21	1.557
PROFI22	1.557
PROFI31	1.557
PROFI32	1.557
C20	1.470
CORR1	1.460
CORR2	1.466
ER1	1.557
ER2	1.557
CR1	1.557
CR2	1.557

3.3 Hertzian contact model

As the contact pressure will be kept constant, it is important to present the model that will be used for its calculation. This is done to remove the influence of different penetrations that would arise if the value of the torque was the load part of the simulation to be kept constant throughout all the simulations. The contact problem that is being studied in this work can be modeled according to Hertz's contact theory, since all the underlying conditions are met:

- The contact are dimensions are far smaller than those of the contact bodies and their curvature radius;
- The contact force is normal to the common tangent plane and its line of action intersects both solids' curvature center;
- The materials are isotropic, homogeneous and elastic, obeying the Hooke's Law;
- When no force is applied, the contact between the bodies occurs along a line instead of an area;
- The contact area is plane and parallel to the common tangent plane;

- The bodies in contact can be obtained through revolution, since the contact between involute profile gear teeth can be modeled as a contact between two cylinders, in the close vicinity of the contact line.

For the C20 gear that is serving as the stepping stone to start the parametric study, the main geometric features relevant to the Hertzian contact approach are presented in table 3.5. The normal force can be obtained through the applied resistant torque through

Table 3.5 Relevant geometric features of the C20 gear.

$\alpha / ^\circ$	r_b / mm	$\overline{T_1I} = \overline{T_2I} / \text{mm}$
20	43.0105	17.4625

Eq. 3.11,

$$F_n = \frac{T}{r_b} \quad (3.11)$$

With a Young's Modulus of 210 GPa and a Poisson's coefficient of 0.3, the combined Young's Modulus can be calculated through Eq. 3.12.

$$\frac{1}{E^*} = \left(\frac{1 - \nu_1^2}{E_1} + \frac{1 - \nu_2^2}{E_2} \right) \cdot \frac{1}{2} \quad (3.12)$$

Finally, the radius of curvature is given by the $\overline{T_1I}$ and $\overline{T_2I}$ segments, which comes from the cylindrical contact approach. The osculating cylinders that are the basis of this approach are shown in Fig. 3.3. The equivalent radius can then be obtained through Eq. 3.13

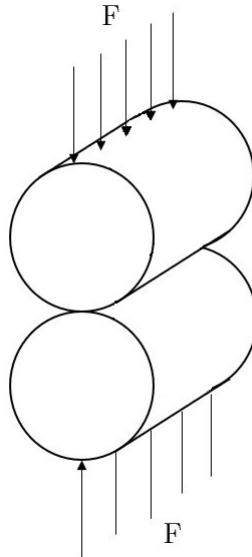


Figure 3.3 Osculating cylinders.

$$\frac{1}{R_X} = \frac{1}{2} \left(\frac{1}{R_{X1}} + \frac{1}{R_{X2}} \right) \quad (3.13)$$

Finally, the value of a , which is the contact surface semi-width, for $F_n = 1162.507$ N, , for a torque which initially had a value of 50 N·m, $E^* = 115.385$ GPa and $R_X = 17.4625$ mm, can be computed through the expression in Eq. 3.14:

$$a = \sqrt{\frac{2 F_n R_X}{\pi \ell E^*}} \quad (3.14)$$

and has a value of $89.44 \mu\text{m}$. The maximum Hertz pressure can also be computed as stated in Eq. 3.15

$$p_0 = \frac{4}{\pi} \cdot p_m = \sqrt{\frac{2 F_n E^*}{\pi \ell R_X}} \quad (3.15)$$

and has a value of approximately 591 MPa, being p_m the average pressure. From this point onwards, several stresses and their distribution can be obtained, but the main aspect that concerns the validation is the location/depth at which the maximum stresses occur. The maximum shear stress occurs, for a linear contact, at a depth given by Eq. 3.16

$$Z_s = 0.7861a \quad (3.16)$$

and its value is, for this case, $70.31 \mu\text{m}$. With this information, in the numerical simulation a refinement shell can be dimensioned to contemplate the relevant part of the contact stresses by defining its thickness according to this value through a relation of $N \times Z_s$, for an arbitrary value of $N = 15$. For the developed models, the thickness of the shell had its value kept at about 1 mm for the gears with a module of 4.5 mm and adjusted by a factor of $\frac{m}{m_{std}}$ for the gears with a different module.

The *Crowning* profile modification results in a pure elliptic contact instead of a linear one, which requires a different approach. For an elliptic contact, there are now curvatures along both contact directions. For the first case of crowning, the radius of curvature along the axial direction of the gear, R_X , obtained from 3.13, has a value of 15.391 mm, which is equal to each of the teeth curvature, due to the fact that they're equal. The same happens with the radius of curvature along the radial direction of the gear, R_Y , which can also be obtained through 3.13 applied to Y instead of X. Its value is 245 mm and, since $R_X > R_Y$, the equivalent curvatures are defined by $A = \frac{1}{R_X}$ and $B = \frac{1}{R_Y}$. Determining the curvature ratio can be done as stated in Eq. 3.17.

$$\frac{A}{B} = \frac{245}{15,391} = 15,9184 \quad (3.17)$$

The values of k_{ab} and C_a and can be obtained through table consultation with this value as an input. Knowing how these parameters vary with the curvature ratio, since its value exceeds 15, a linear interpolation leads to a fairly accurate value. Interpolating between

$A/B = 15.5$ and $A/B = 16$, according to the expression in Eq. 3.18

$$k_{ab} = k_{lb} + \left(\frac{A}{B}\right) \cdot \frac{(k_{hb} - k_{lb})}{\left(\frac{A}{B}|hb\right) - \frac{A}{B}|lb)} \quad (3.18)$$

where the lb and hb indexes indicate whether the value corresponds to the lower bound or upper bound, respectively, the value of k_{ab} can be obtained. This expression can be used to determine the values of C_a simply by replacing the k_{ab} variables with the one to be determined. Finally, the contact semi-width/smaller axis of the contact ellipse can be determined through the expression in Eq. 3.19

$$a = C_a \left[\frac{F_n}{(A + B)E^*} \right]^{\frac{1}{3}} \quad (3.19)$$

The larger axis of the ellipse can be obtained by Eq. 3.20

$$b = \frac{a}{k} \quad (3.20)$$

and finally, the maximum contact pressure can be computed from Eq. 3.21

$$p_0 = \frac{3}{2} \frac{F_n}{\pi ab} = \frac{3k}{2} \frac{F_n}{\pi a^2} \quad (3.21)$$

Rather than keeping constant input torque for all simulations, the contact pressure value was kept constant throughout the different geometries. Fixing the value calculated, the resistant torque applied on the gear will be adjusted in the relevant cases to accommodate the changes in active root radius and curvature radius at the primitive circle. For that, the *Microsoft Excel Solver* becomes a quick and useful tool to determine the value of the resistant torque that must be applied in each case: the maximum contact pressure cell becomes the objective, with the value obtained from Eq. 3.15, the resistant torque cell becomes the variable and a restriction to keep the torque value as non negative can be added to avoid solutions outside the problem's domain.

3.4 Torsional Model

A spur gear pair contact can be simplified as two-DOF vibrational model, represented in the free body diagram shown in Fig. 3.4. The shafts are considered rigid and the mesh condition is assumed perfect. Inaccuracies such as eccentricity, unequal tooth width and pitch deviations are, as a consequence, not taken into account. However, these imperfections are negligible in this study [17].

Based on these considerations and the D'Alembert Lagrange's principle, the differential equations of motion can be expressed as shown in Eqs. 3.22 and 3.23:

$$J_p \ddot{\varphi}_p + C(\dot{\varphi}_p - \dot{\varphi}_g - \dot{e}) + K_t(\varphi_p - \varphi_g - e) = T_p \quad (3.22)$$

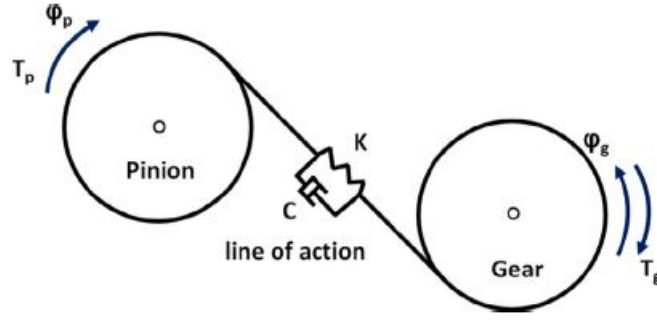


Figure 3.4 Free body diagram of the torsional model of the gear pair [17].

$$J_g \ddot{\varphi}_g - C(\dot{\varphi}_p - \dot{\varphi}_g - \dot{e}) - K_t(\varphi_p - \varphi_g - e) = -T_g \quad (3.23)$$

The rotary inertia of the pinion and the gear are represented by J_p and J_g , C and K_t are, respectively, the damping coefficient and the torsional mesh stiffness. $\ddot{\varphi}_p$ and $\ddot{\varphi}_g$ represent the angular acceleration of the pinion and gear, $\dot{\varphi}_p$ and $\dot{\varphi}_g$ the angular velocity and φ_p and φ_g the angular displacement. The total gear backlash is taken into account in the quantity e [17].

A quasi-static approach becomes valid when the pinion and gear rotate very slowly, with constant speeds typically under 0.1 /rads^{-1} , and the inertial effects produced are disregardable. Ignoring the derivatives in order to the time variable, 3.22 and 3.23 can be rewritten as stated in Eqs. 3.24 and 3.25 [17].

$$K_t(\varphi_p - \varphi_g - e) = T_p \quad (3.24)$$

$$-K_t(\varphi_p - \varphi_g - e) = -T_g \quad (3.25)$$

From the expressions obtained upon simplification, the concept of transmission error can be materialized by the following definition in Eq. 3.26,

$$TE = \varphi_p - \varphi_g - e \quad (3.26)$$

which translates into the difference between the theoretical angular position of the driven gear and its actual position during the contact and while it runs the driving gear, at constant speed.

Upon such definition and recalling the Eqs. 3.24, 3.25 and 3.26, the torsional mesh stiffness can be defined as stated Eq. 3.27 [17].

$$K_t = \left| \frac{T_p}{TE} \right| = \left| \frac{T_g}{TE} \right| \quad (3.27)$$

Based on the gear geometry, the linear mesh stiffness can be easily obtained dividing

the torsional mesh stiffness by the squared base radius, which yields Eq. 3.28.

$$K_t = \frac{K_t}{r_{bp}^2} = \frac{K_t}{r_{bg}^2} \quad (3.28)$$

These equations lead to the same definitions presented in Eqs. 2.4 and 2.6. These expressions will be used in the result analysis since this model describes the behavior of the implemented model and handles the quantities that can be obtained from it.

This page was intentionally left blank.

Chapter 4

Simulation preparation and setup

In this chapter, the whole process of the numerical implementation part is presented. From the geometry definition to the FEA part, the main steps towards achieving the results are described. Some problems that occurred and some implementation details that are considered important or even necessary are highlighted to save the reader some time, both avoiding those problems and time spent solving them.

4.1 Tools

Fig. 4.1 condensates the implementation and analysis steps of the work done. There it can also be seen where the FEA part, Simulation preparation, is located along the workflow.

The *KISSsoft* version used was the 2019 one, the *SolidWorks* version was the 2020 one and the *ANSYS* version used was 2020 R2.

4.2 Gear Geometry Definition

In this section, the generation and treatment of the geometry to be inserted into the FEM software is discussed.

4.2.1 Geometry Generation

The first step is the definition of the gear design parameters in *KISSsoft*. Since the desired position of the gear teeth will be defined in the assembly later on, a single gear can be generated. This procedure covers not only the cases where the gear teeth are identical but also the cases where they differ and therefore is more generic. Since the loading/operation conditions of the gear teeth pair will be an aspect concerning the simulation and not the applicability of the gear, the Rating tab can be removed. However, if one wishes to validate or verify the loading conditions, Rating must be kept and a Contact Analysis

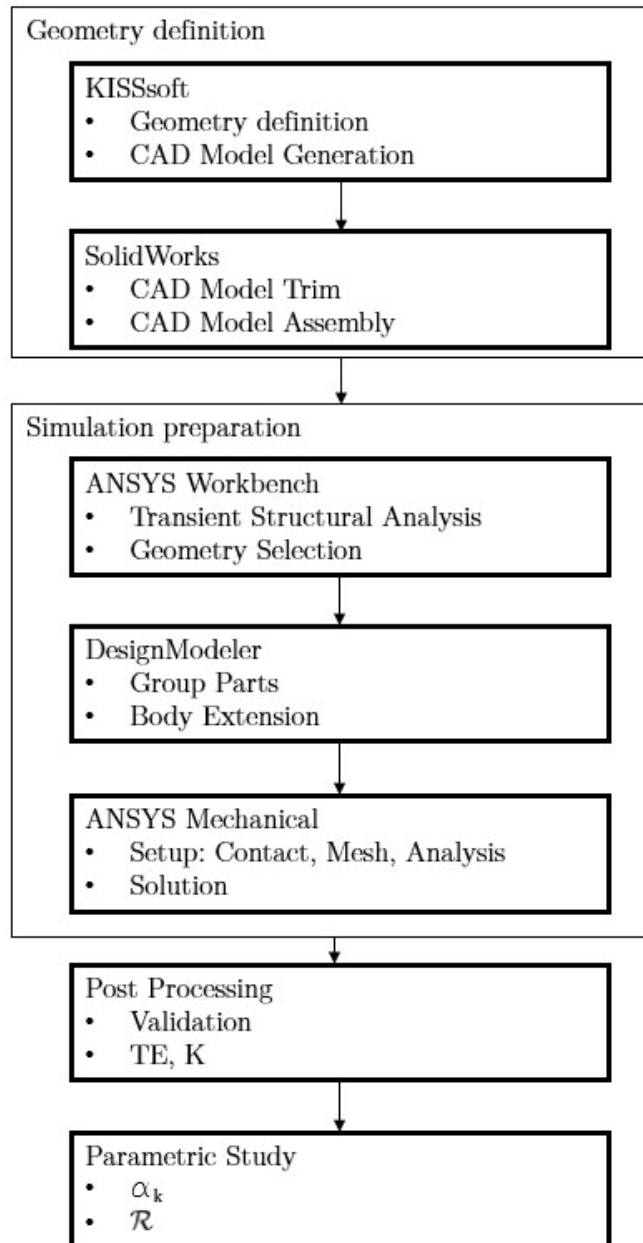


Figure 4.1 Overall workflow schematic.

must be employed. The tip alteration modifications are not present in the base parameters, as well as the profile modifications that are going to be studied. Fig. 4.2 shows the checkbox that needs to be checked to allow this parameter to be an input chosen by the user. As an additional regard concerning tip alteration, when profile shifts are included, the software automatically inserts tip alteration on the gear. Since the aim of this study requires each parameter to be modified at a time, such cases require the tip alteration to be manually set to 0.00. The modifications tab is not a base one, meaning it must be

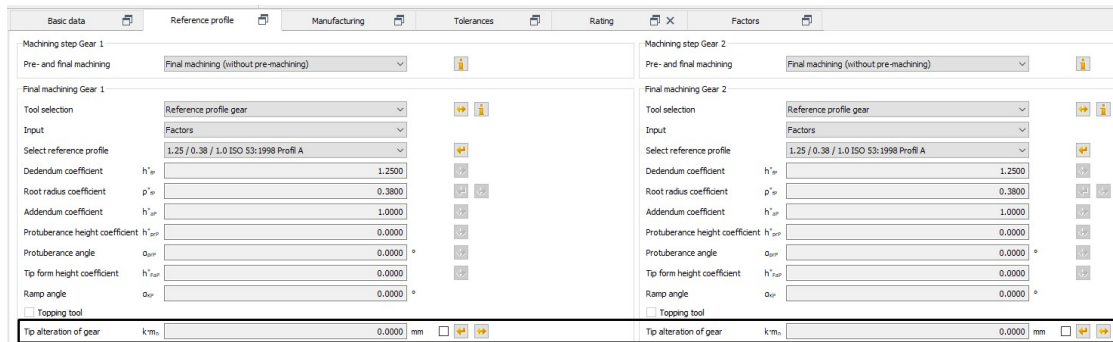


Figure 4.2 Tip alteration adjustment.

added. This can be done by selecting the option shown in Fig. 4.3. The chosen profile

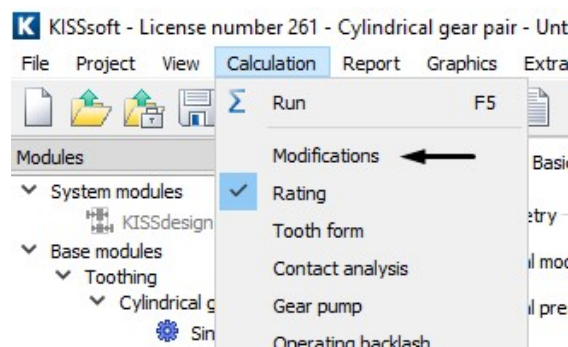


Figure 4.3 Profile modification selection.

modifications already mentioned and their type and value must be inserted in the area shown in Fig. 4.4.

Once the geometry is fully defined, a Calculation must be run and from the Graphics, the CAD model can be exported as a .stp file. Generating a report concerning this geometry is very useful, since all the information needed for contact pressure, coordinate shift and mesh stiffness calculation is included there.

4.2.2 Geometry Manipulation

Once the CAD model is exported from KISSsoft, it can be handled in the SolidWorks environment in order to be assembled properly. A good manipulation of the geometry will make the modeling in the FEM software much easier. Since the relevant approximated

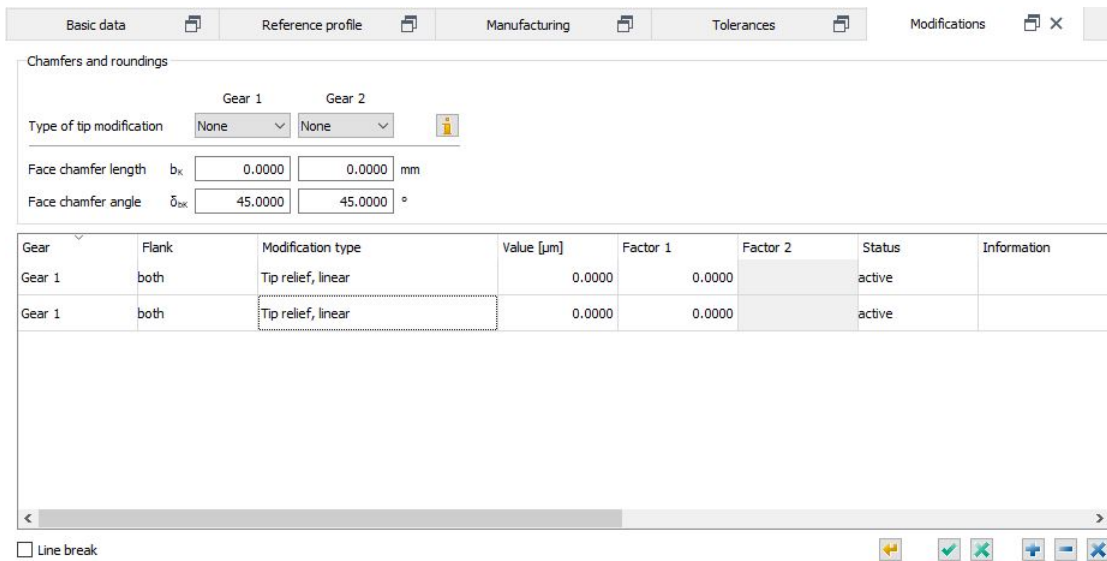
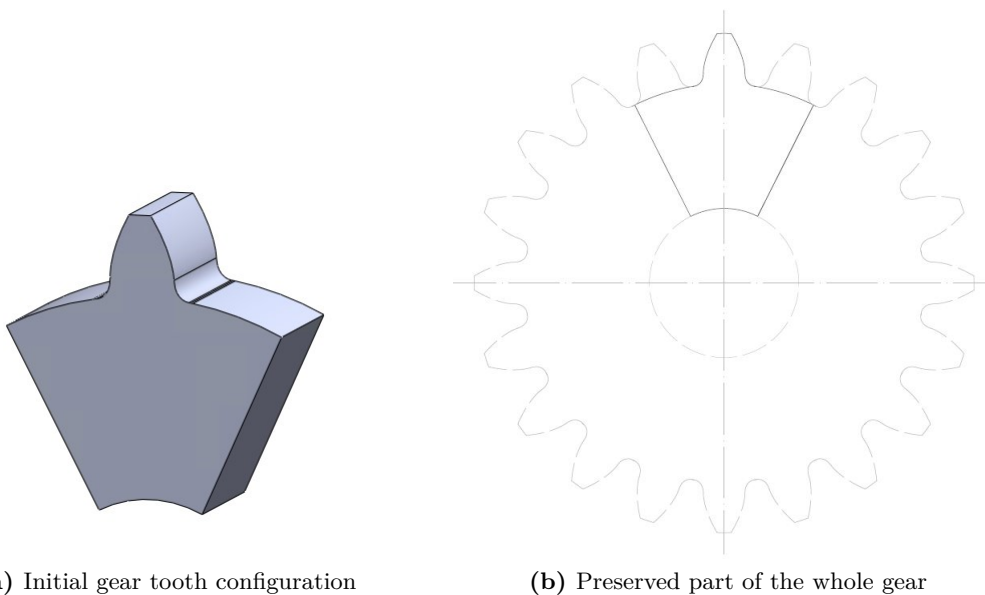


Figure 4.4 Profile modifications window.

analytical model allows the study of a single teeth pair contact, the geometry will be modeled that way, which is a great way of reducing complexity of the geometry and allow a much better discretization. Summarizing the whole process, the main steps towards achieving the desired model are:

1. Gear Trimming (Cut Extrude Feature), as exemplified in Fig. 4.5;



(a) Initial gear tooth configuration

(b) Preserved part of the whole gear

Figure 4.5 Gear trimming schematic.

2. Gear Partitioning (Split Feature);

3. Refined region Creation (Split Feature);
4. Assembly, where it is required to:
 - (a) Create a point at the center of rotation of the pinion and gear;
 - (b) Create a vertical line with a length equal to the center distance of the gear pair;
 - (c) Draw a circle with a diameter equal to the active root diameter on the pinion;
 - (d) Draw a circle with a diameter equal to the addendum diameter on the gear;
 - (e) Create a point on the leftmost (to an observer on the front plane) intersection of both drawn circles;
 - (f) Make both the pinion and gear coincident with the point created on the previous step;
 - (g) Verify that the assembly is fully defined. Restrict any leftover unwanted movement if the assembly is under defined.
5. Export as `.stp` file.

Since this model was unable to provide acceptable results, a similar model containing a refinement region was developed. Several configurations, shown in Fig. 4.6, were tested until an acceptable one was found. An extensive study towards capturing local deflections in the model was employed. Since the refinement has the main goal of capturing local effects, restricting it to the contact area was an advantageous measure both in terms of computational efforts and simulation time. Several refinement regions were tested in order to evaluate the necessary refinement level for the contact stresses to match the analytical stress distributions obtained. Some refined regions, Figs. 4.6a and 4.6b, proved inefficient in the meshing process given their reduced dimension and the inability for the model to transition from the local refined elements to the coarser mesh on the remaining gear body. The third refined region, Fig. 4.6c, even though the meshing process happened smoothly, would lead to an excessive element concentration at the zone and would go beyond the region where the contact happened. The chosen refined region was Fig. 4.6d, having a thickness of about $15 \times Z_s$ mm, for the Z_s calculated for an initial torque of 50 N·m. This refined region performed well when the torque was increased later on, so this configuration was maintained. To achieve a structured mesh, in a similar way that was done with the refined region, the remaining body was partitioned as shown in Fig. 4.7. Finally, a configuration that turns Fig. 4.8a into Fig. 4.8b was adopted. With the trimmed teeth, the assembly was made to achieve the configuration shown in Fig. 4.9.

Once again, the geometry is exported as a `.stp` file in order to be handled in the next software.

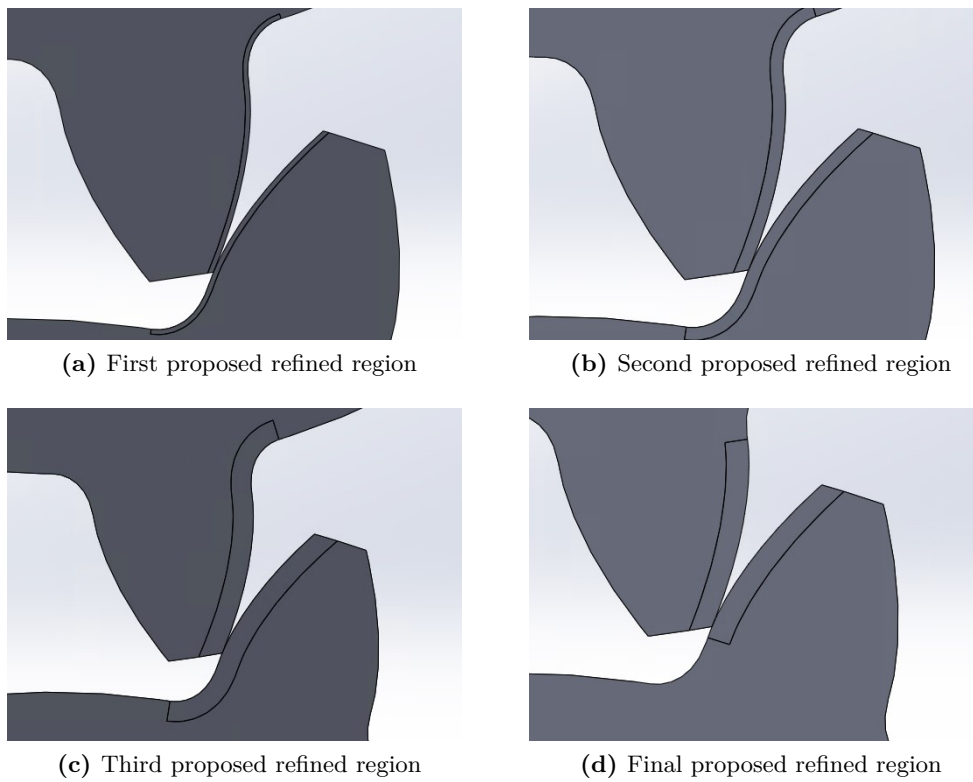


Figure 4.6 Different refined region configurations employed.

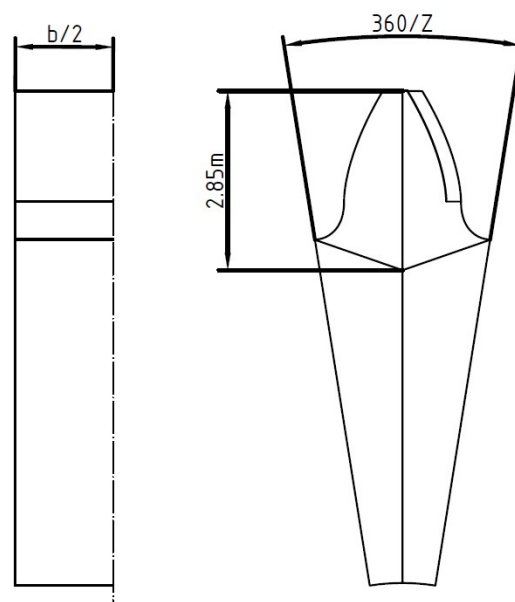


Figure 4.7 Schematic of the gear tooth partitioning .

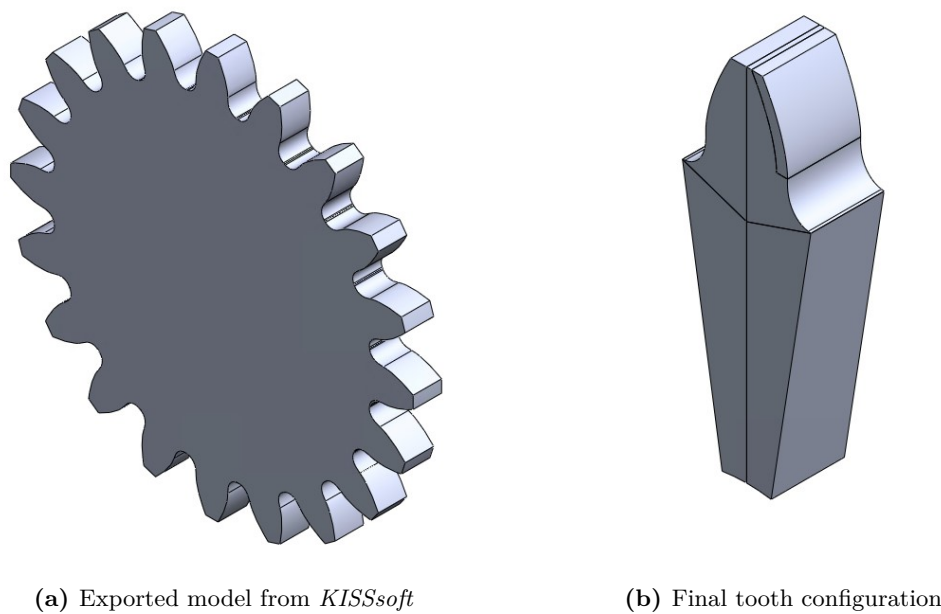


Figure 4.8 Initial and last stages of the tooth preparation process.

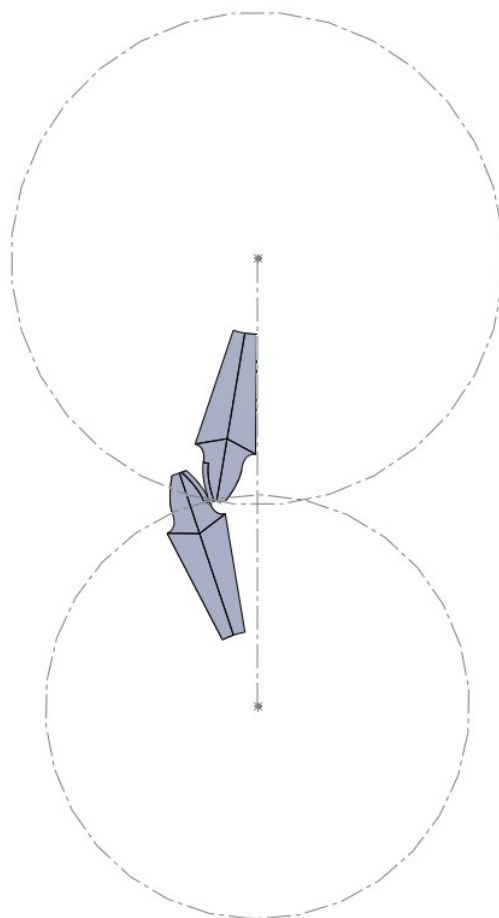


Figure 4.9 Final configuration of the assembly.

4.3 Simulation preparation: ANSYS Workbench

In the ANSYS Workbench, a Transient Structural analysis is created. In the Geometry tab, the saved SolidWorks CAD model is inserted. The configuration obtained from SolidWorks, for most cases, performed well. However, for some setups tested, convergence errors occurred on the region highlighted in Fig. 4.10. To overcome this, material was

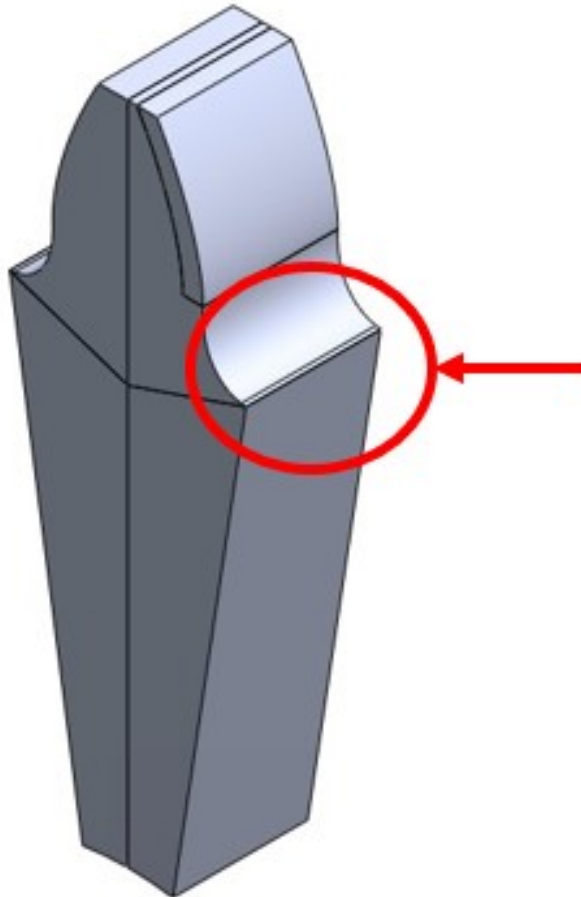


Figure 4.10 Location of the most common convergence problems.

added at the location to spread what was believed to be an excessive load at the mentioned region where the elements became excessively distorted. In the Design Modeler environment, which can be accessed by right clicking the Geometry tab and selecting *Open with Design Modeler*, the material was added through revolution of the lateral faces. To each side, a revolution, in degrees, given by $\frac{360}{4-z}$ was inserted. For that, an additional referential was added, in relation to the default ones with an offset equal to the center distance. Only then was the Revolve feature possible for the gear. This amount of material was enough to prevent the same convergence error to happen in the following simulations, for a transmission ratio of 1. The final geometry is shown, as seen in the Design Modeler

environment, in Fig. 4.11. Having established the geometry of the model, the boundary

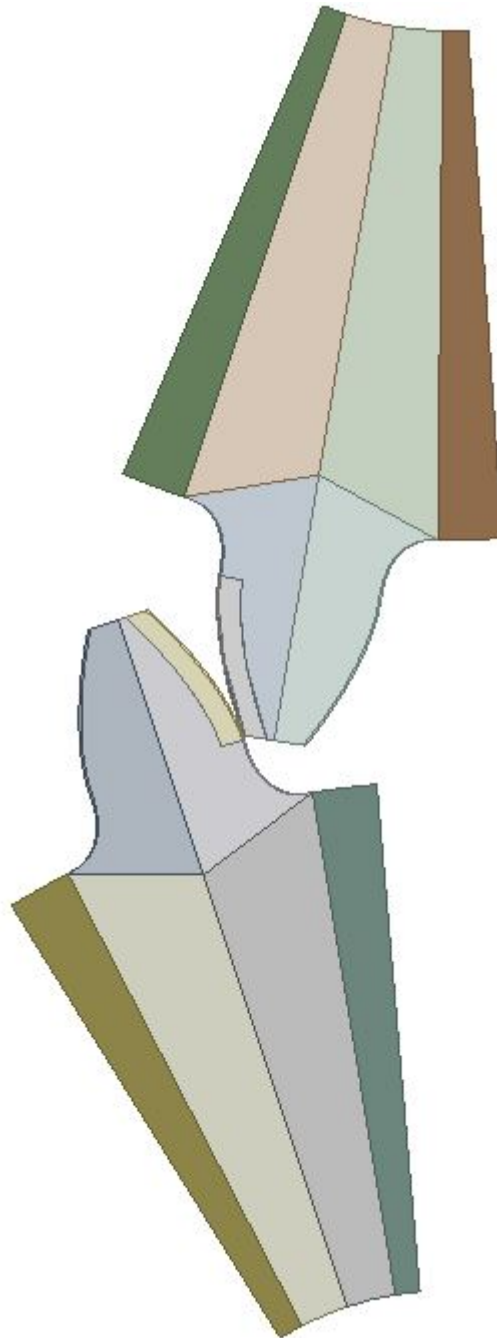


Figure 4.11 3D model geometry

conditions, contact definitions, meshing, solution and results will be discussed.

4.3.1 Boundary Conditions

Concerning the boundary conditions applied, the main features to be introduced are presented in Fig 4.12. Given the attention that the contact requires, Section 4.3.2 will

deal with it with the deserved detail. Two joints are added, one for the gear and one for

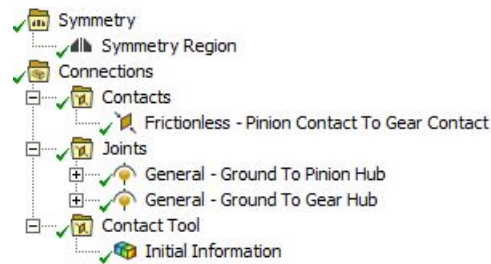
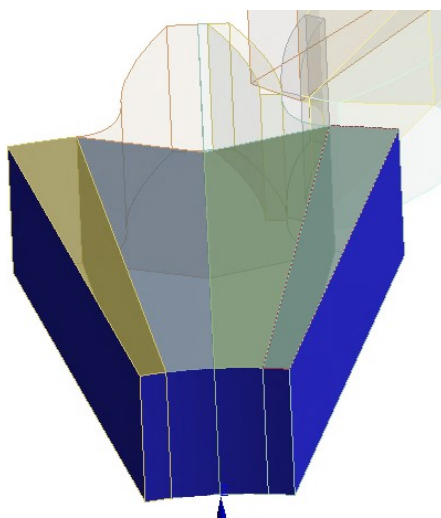


Figure 4.12 Boundary Conditions.

the pinion, both with the details shown in Fig. 4.13. This addition will allow each body to fully behave according to a rotational DOF at its center, being the most appropriate way to probe the most relevant results for this study. Both the pinion hub and gear hub are connected with Body-Ground joints with all the DOF restricted except the rotation around the Z axis.



(a) Pinion joint selections

Details of "General - Ground To Pinion Hub"	
Definition	
Connection Type	Body-Ground
Type	General
Suppressed	No
Translation X	Fixed
Translation Y	Fixed
Translation Z	Fixed
Rotations	Free Z
Element APDL Name	
Reference	
Coordinate System	Reference Coordinate System
Behavior	Rigid
Mobile	
Scoping Method	Named Selection
Applied By	Remote Attachment
Mobile Component	Pinion Hub
Body	Multiple
Initial Position	Unchanged
Behavior	Rigid
Pinball Region	All

(b) Pinion joint details

Figure 4.13 Appropriate joint setup.

To ease the repetition of these steps in all the models prepared, which has to be done separately, named selections, shown in Fig. 4.14 are created. The Gear and Pinion selections include the whole bodies, individually but containing all the partitions for each one. The Gear and Pinion Contact named selections correspond to the contact selection of the contact and target faces and the Pinion and gear Hub are the selections that grant an appropriate behavior of the model. Among all those created, the one remaining that requires an exemplification is the selection that allows the joint referential to be created at the designated location. By employing the selection shown in Fig. 4.15, the referentials show up at the desired locations, respecting the center distance that was defined when the assembly was created earlier. This selection allows a referential to be automatically

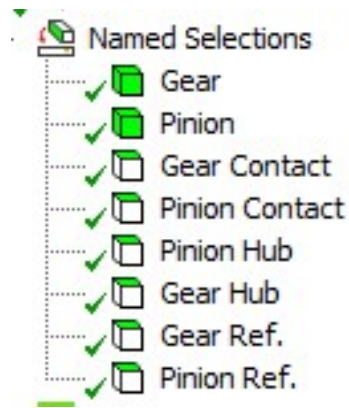


Figure 4.14 Named selections.

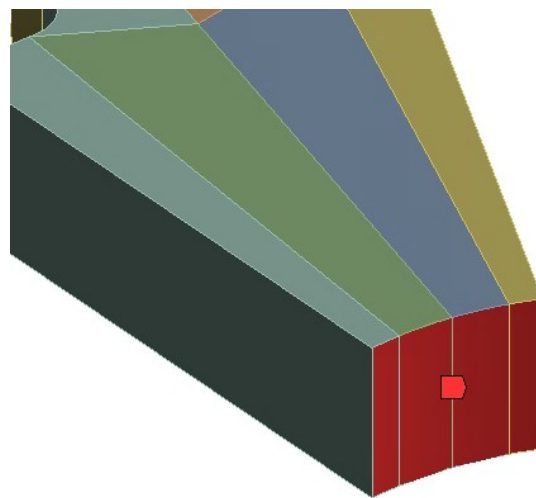


Figure 4.15 Pinion referential selection.

created as shown in Fig. 4.16. If the same is done for the gear, it is expected that a referential respecting the same rules is created for that body.

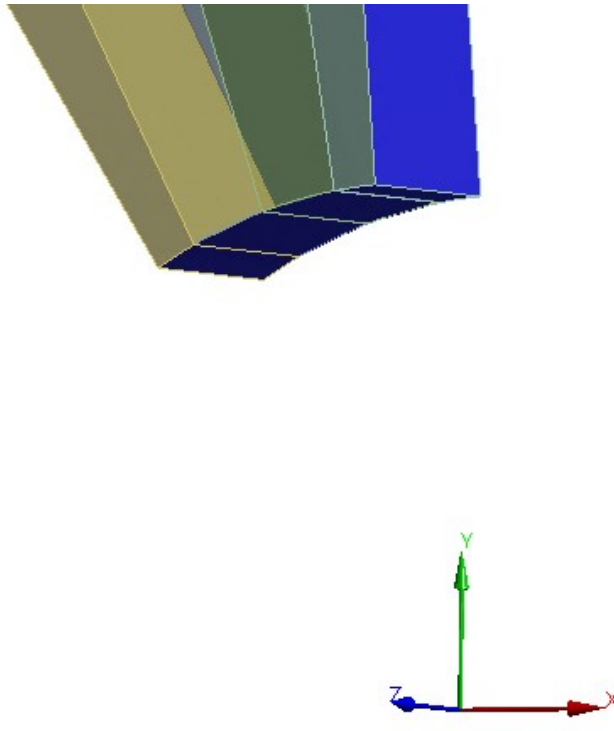


Figure 4.16 Pinion referential.

4.3.1.1 Symmetry

A symmetry is added to the model dividing it in half through its width. Symmetry planes, when existing, are widely used and extremely advantageous in finite element analyses, specially when there are limitations on how many elements/nodes are allowed to exist, which happens in the current work. This symmetry makes it possible to double mesh's density by halving the model's volume, making it possible to analyze bigger models with more detail. The symmetry plane added is shown in Fig. 4.17.

The symmetry plane can either be defined directly or have all the nodes comprising it with movement along the Z direction, the direction normal to the rolling plane, restricted. For a converged simulation, the displacements along the Z direction, on the face not contained in the symmetry plane, can be seen in Fig. 4.18. The values are not zero and the zones under compression and tension are easily identifiable and according to what is expected. Once again, for a converged simulation, the displacements along the Z direction, this time on the face contained in the symmetry plane, can be seen in Fig. 4.19 and their values are, practically, zero. This is indeed the expected behavior and provides validation towards the symmetry approach.

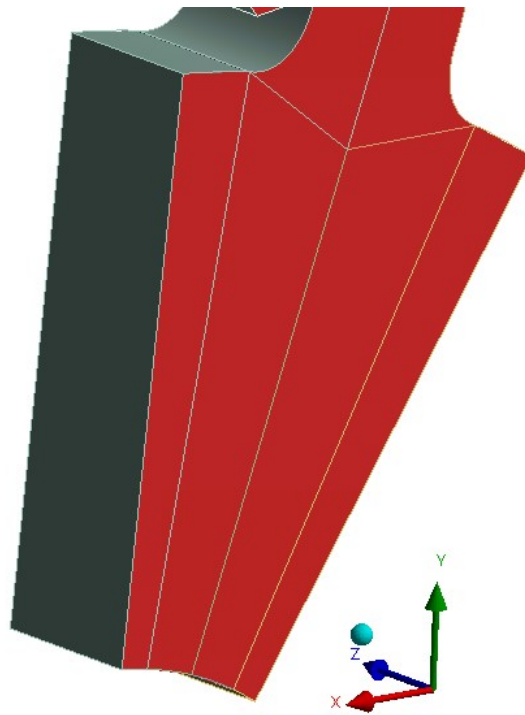


Figure 4.17 Symmetry plane.

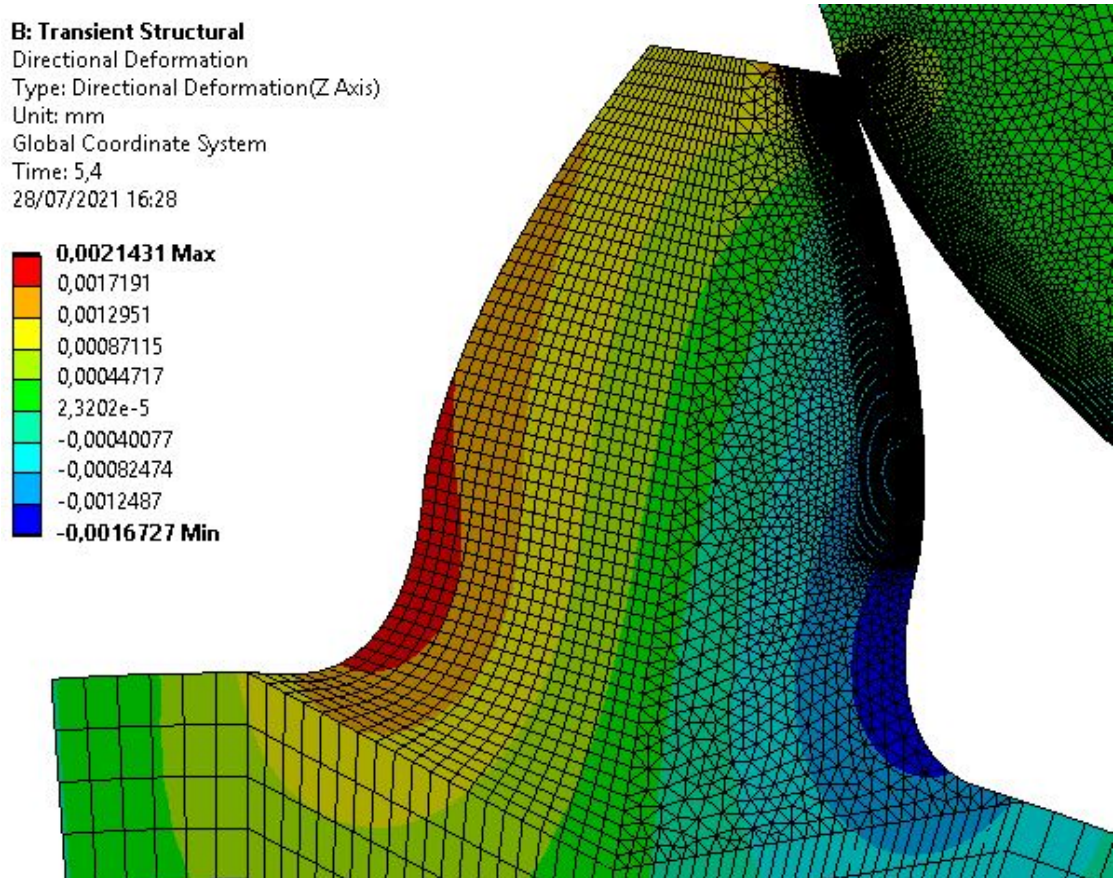


Figure 4.18 Displacements along the Z direction.

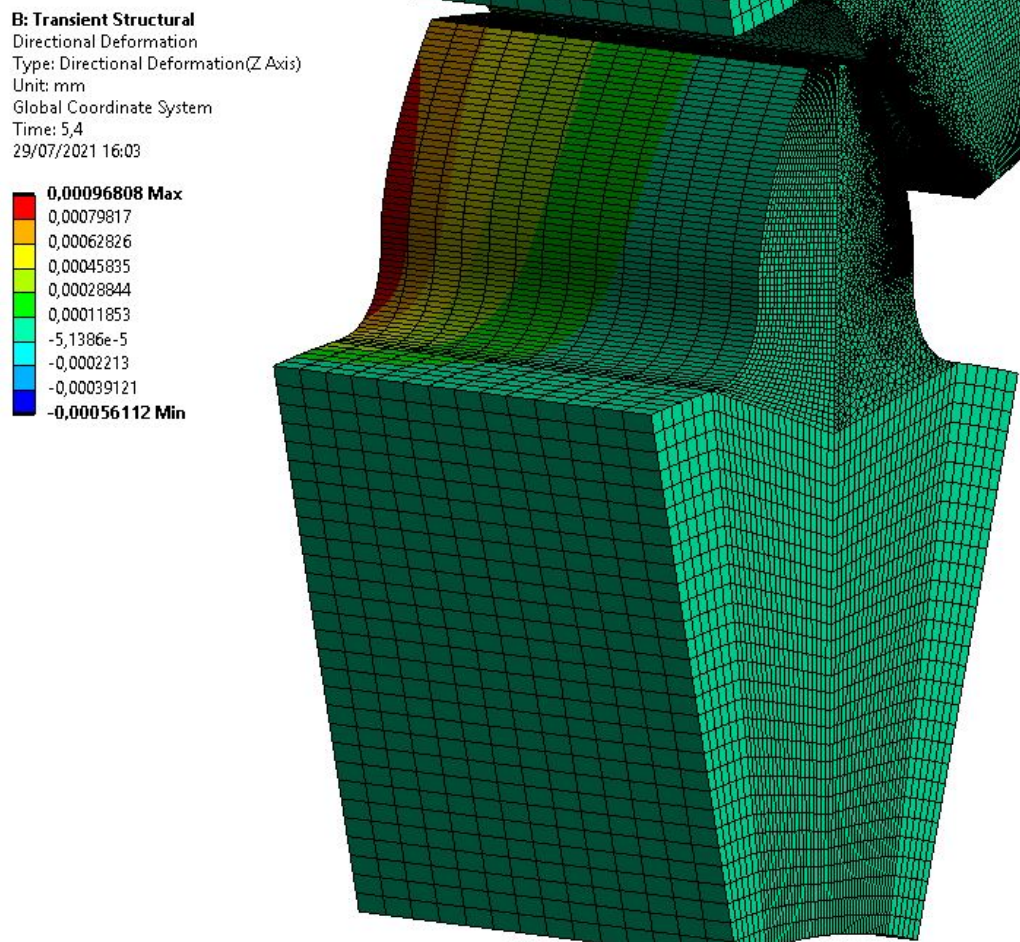
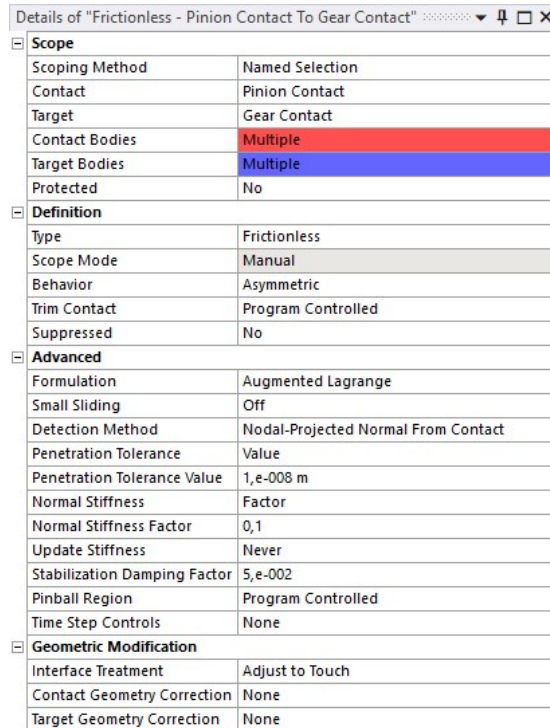


Figure 4.19 Displacements along the Z axis on the symmetry plane.

4.3.2 Contact

A frictionless contact is adopted, since the main aspect regarding the transmission error, load sharing and mesh stiffness is the normal force transmitted between the teeth flanks. Some adjustments regarding the formulation and penetration between the bodies are implemented to diminish the model's sensitivity to the contact stiffness, as shown in Fig. 4.20.



Details of "Frictionless - Pinion Contact To Gear Contact"	
Scope	
Scoping Method	Named Selection
Contact	Pinion Contact
Target	Gear Contact
Contact Bodies	Multiple
Target Bodies	Multiple
Protected	No
Definition	
Type	Frictionless
Scope Mode	Manual
Behavior	Asymmetric
Trim Contact	Program Controlled
Suppressed	No
Advanced	
Formulation	Augmented Lagrange
Small Sliding	Off
Detection Method	Nodal-Projected Normal From Contact
Penetration Tolerance	Value
Penetration Tolerance Value	1, e-008 m
Normal Stiffness	Factor
Normal Stiffness Factor	0,1
Update Stiffness	Never
Stabilization Damping Factor	5, e-002
Pinball Region	Program Controlled
Time Step Controls	None
Geometric Modification	
Interface Treatment	Adjust to Touch
Contact Geometry Correction	None
Target Geometry Correction	None

Figure 4.20 Contact Details.

The target and contact surfaces/bodies are selected as shown in Fig.4.21. The asymmetric default option is kept to achieve convergence. A single contact surface-target surface pair is created, known as an asymmetric contact or "one-pass contact". When the symmetric option is chosen, two sets of contact pairs are generated. Each surface then acts as both a contact and a target surface and this contact is also known as "two-pass contact". This configuration is, naturally, less efficient, but many analysis benefit from it when it comes to reducing penetration. In this case, the penetration reduction is achieved by reducing the penetration tolerance value.

The Augmented Lagrange formulation is suitable for most problems and its wide coverage makes it appropriate for a problem that does not perfectly fit in the categories in which the other options excel. This formulation blends the Lagrange Multiplier method with the Penalty formulation to compensate each other's disadvantages. In this method, the contact tractions (in this case pressure only, since there are no frictional stresses) are augmented while iterating to achieve a final penetration within the defined tolerances.

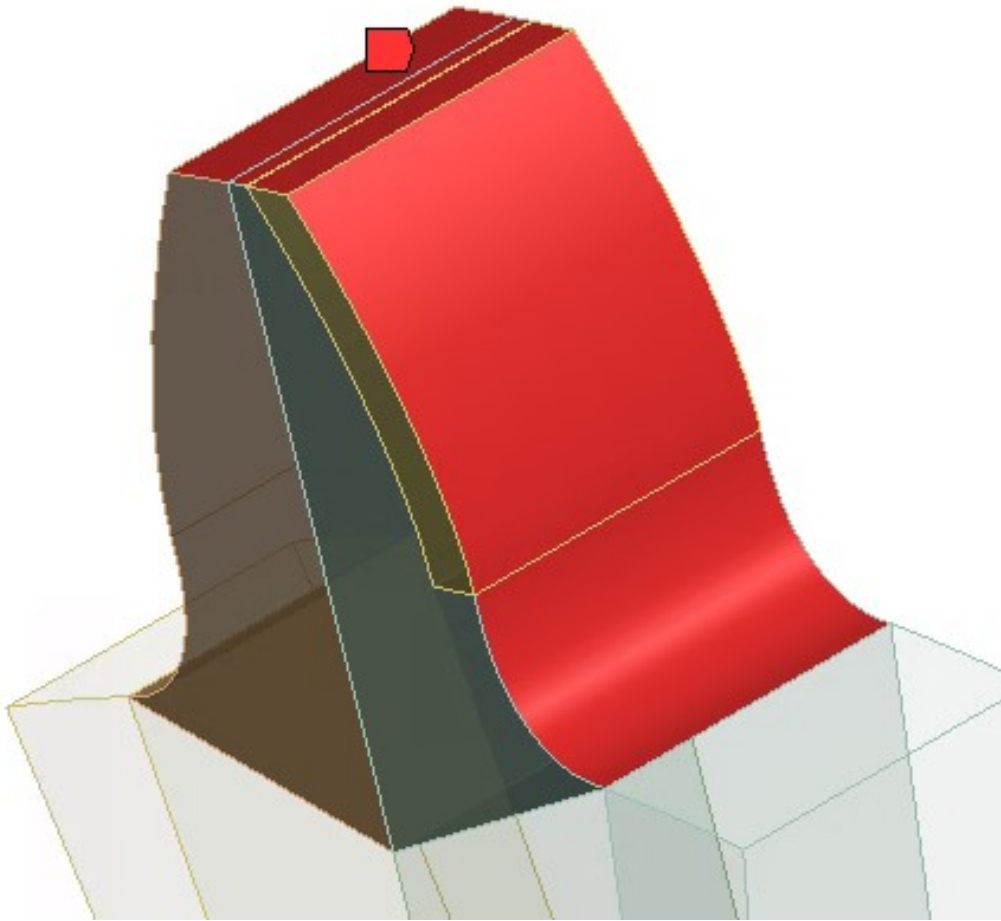


Figure 4.21 Contact Selection.

This method's condition is better than that of the penalty method and shows less sensitivity to the magnitude of the contact stiffness. A drawback in the method resides in its need for additional iterations, specially in cases when the deformed mesh shows significant distortion. The method is better than the pure Lagrangian method in terms of computational cost.

Given the nature of how the initial contact is established, a proper detection method must be selected. Contact detection at Gauss points is a very poor choice due to the fact that one of the surfaces has a corner, which is the edge at the tooth tip, when the contact begins. Although contact detection at nodes improves the quality of the simulation when compared to the previous option, with smoother plots, it shows longer convergence times and some instabilities for some surface combinations. Therefore, the latest added option to the software and that also proves to be a major improvement is the Nodal-Projected Normal from Contact, which overcomes the mentioned limitations. This option provides good results without significant contact pressure spikes at nodes, a better convergence

behavior if the contact surfaces are adequately meshed and the mesh is properly discretized and leads to an overall better performance if both the surfaces in contact are meshed with a similar mesh size, which is the case.

The normal penalty contact stiffness, known as FKN, plays a major role in the convergence behavior of the model: lowering its value will ease the convergence. However, the software provider recommends certain values depending on the problem at hands:

- FKN = 0.1 for problems dominated by bending deformation;
- FKN = 1.0 for problems dominated by bulk deformation;
- FKN = 10 for bonded surfaces.

The value of the normal penalty contact stiffness, Normal Stiffness Factor in the contact details, is then chosen to better accommodate the effects that dominate this problem, 0.1, and has its value fixed to mitigate any effect on the mesh stiffness that is being determined [23,24].

The contact stabilization damping, destined to nonlinear contacts (in this case, frictionless), handles oscillations that may occur associated with the dynamic nature of the problem, even though the speeds are kept quite small to achieve a quasi-static behavior. If the value is kept at 0, which is the default value, the damping only activates under certain circumstances and in the first load step only. If a value greater than 0 is used, the damping applies to all the load steps. It is worth mentioning that the damping factor selected applies only to the normal direction. The Tangential damping factor is not directly shown in *ANSYS Mechanical*, but it is unnecessary in this particular case. To avoid some common convergence failures in non-linear problems involving contact, mainly caused by initial gaps and oscillation between the two bodies, an initial contact is established through the Adjust to Touch definition in the interface treatment. Mesh discretization often creates artificial gaps between surfaces, even when the CAD model is built to have them touching one another. This option removes the gap numerically by assuming that the surfaces are in fact touching.

Given the nature of the problem in hands, alongside the boundary conditions defined, the initial contact must be properly defined to avoid rigid body motion by making the surfaces touch when handling the CAD model, which may jeopardize the whole analysis. Even if the geometrical model appears to be touching, several issues may keep it from converging or even begin simulating:

- the complexity of the profiles may make it harder to pinpoint the first point of contact;
- the mesh may have small gaps between the elements on both sides of the element pair, resulting from numerical round-off;

- small gaps may exist between the integration points of the contact and target surfaces elements.

However, there is also the possibility that the opposite may occur: too much initial penetration between the contact and target surfaces can lead to an overestimation of the contact forces and result in nonconvergence or even breaking-away of the contacting components.

It is, then, recommended to always verify the initial contact status in order to prevent crashes that may be time consuming and quickly find out if adjustments need to be made to the model.

4.3.3 Meshing

4.3.3.1 Element Order

Initially, the whole model was meshed with quadratic elements. The first geometries did not allow for a structured mesh to be employed, so the model was completely meshed with quadratic tetrahedral elements. This resulted in a large number of nodes that quickly would exceed the node number limitation of the software. It was also present, from the beginning, that the whole model did not require the same kind of refinement as the contact area and work was done to decouple, as best as possible, the region that needed the refinement and the region where the refinement would bear no benefit and would misspend the additional nodes [25]. The quadratic elements did not pose an advantage towards saving on the amount of nodes and a different choice was made. That being said, the whole model, aside from the tetrahedral partition and the contact surfaces was meshed with linear elements and the regions mentioned were meshed with quadratic elements.

4.3.3.2 Convergence

Convergence studies were employed to both the gear body and the refinement region. The aim of this study was to establish:

- the number of elements in the body after which the increase in the density of the mesh would not provide any benefit;
- the degree of refinement on the refined region beyond which the results would bear little to no change;
- the amount of substeps that would lead to fewer numerical errors;
- the value of the torque that would lead to smoother results and no *contact chattering*.

Regarding the body mesh, several numbers of nodes were employed while the refinement region mesh remained unchanged. Fig. 4.22 shows the overall number of nodes of each mesh employed and the TE obtained, for a torque of 75 N·m. It becomes clear that the number of nodes of the body bears little to no effect on the behavior of the TE curve.

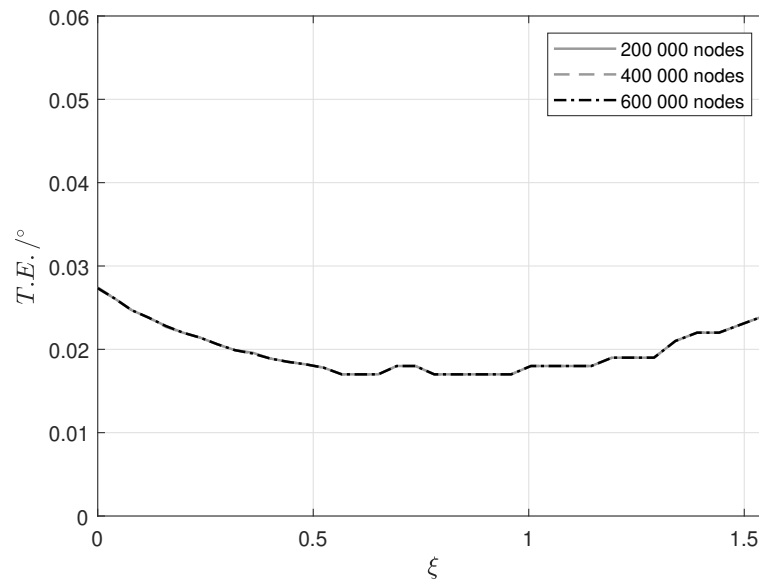


Figure 4.22 Body mesh convergence study.

The lowest density value was chosen to save as much elements/nodes as possible for the refinement region, keeping in mind that reducing the body number of nodes further could lead to numerical errors.

Then, the number of nodes on the refined region was studied. Although in some cases the overall number of nodes was the same as the previous study, the majority of elements was now concentrated on the surface where the contact would occur throughout the line of action. Fig. 4.23, unlike the previous study, shows discrepancies between the different numbers of nodes employed. Since the differences between the mesh with 550 thousand

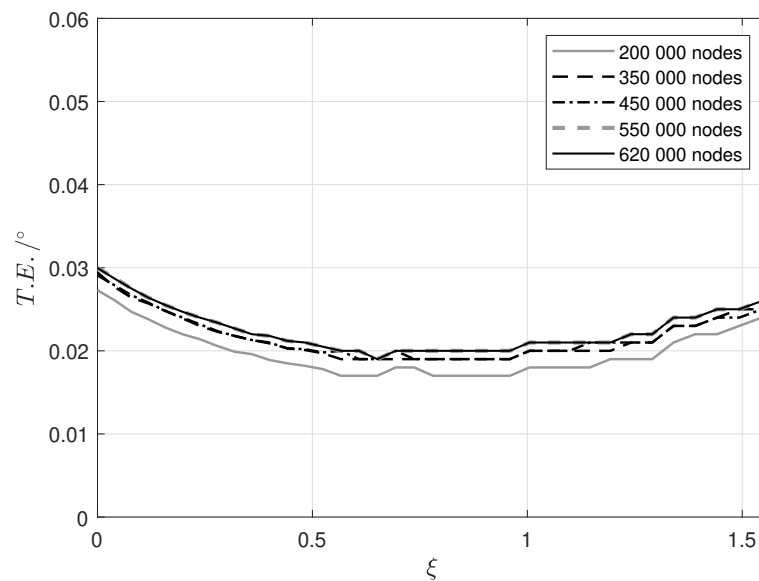


Figure 4.23 Refined mesh convergence study.

nodes and the one with 620 thousand nodes are negligible, the mesh with the lower amount

of elements/nodes was chosen to reduce simulation time.

The number of substeps was studied, with the amounts set to those shows in Fig. 4.24. As the amount of substeps increased, so did the numerical errors, corresponding to the

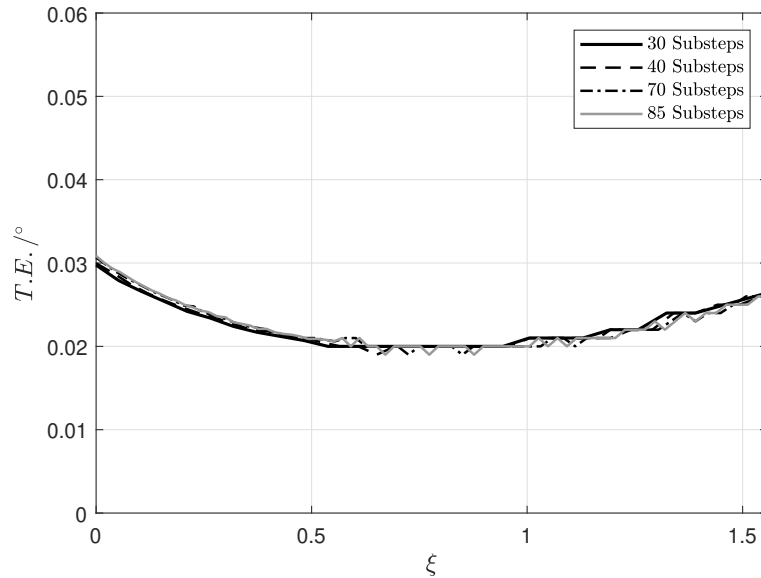


Figure 4.24 Substep number study.

peaks that deviate from the expected parabolic behavior of the curve. It was then decided that 30 substeps would be the most appropriate choice. Finally, several values of torque were studied, being the results obtained in Fig. 4.25. From the obtained results, the value

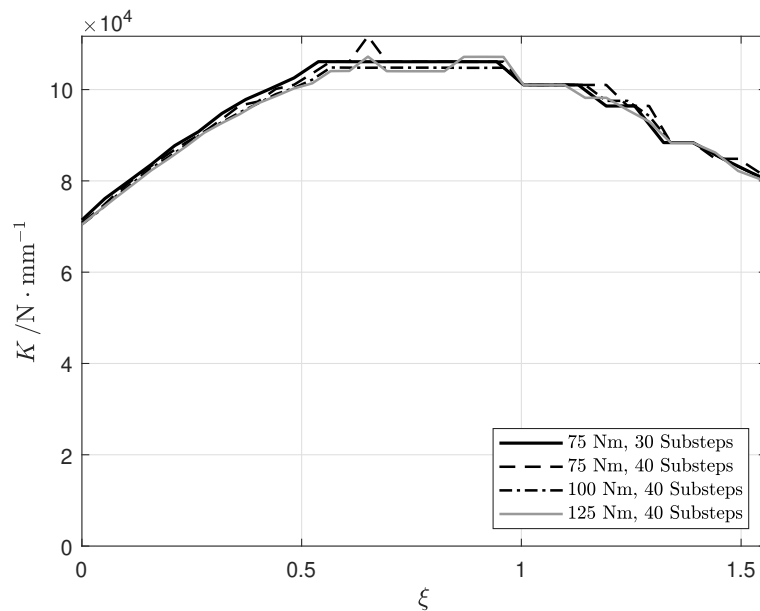
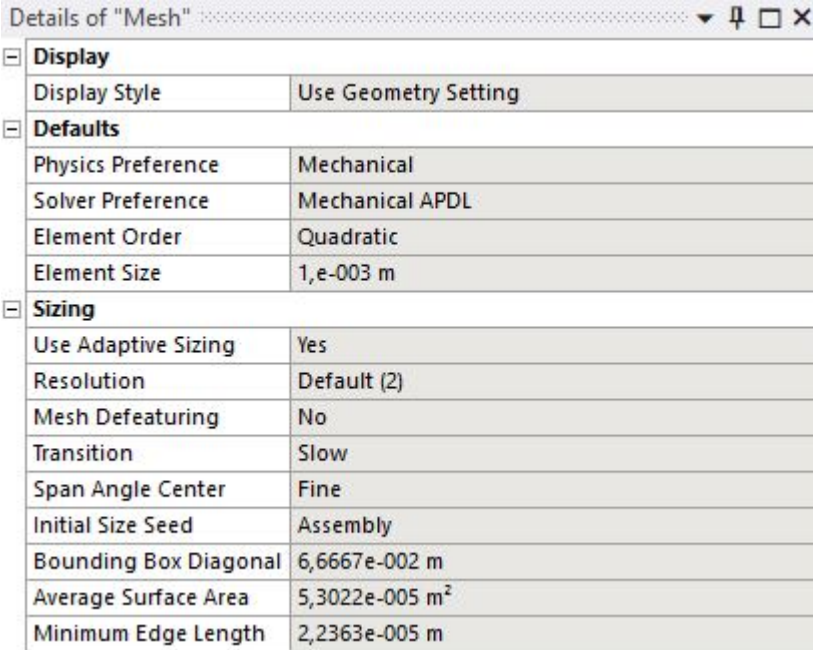


Figure 4.25 Torque value study.

of 100 N·m, for the standard gear, proved itself to be promising regarding the mitigation of numerical errors and the possibility of contact shattering.

4.3.3.3 Final Configuration

In this section, the final mesh adopted, how it looks and some additional regards concerning how it is obtained are presented. In Fig. 4.26, the relevant mesh details employed are shown. To avoid distorted elements, which is common in cases where the magnitude



Details of "Mesh"	
Display	
Display Style	Use Geometry Setting
Defaults	
Physics Preference	Mechanical
Solver Preference	Mechanical APDL
Element Order	Quadratic
Element Size	1,e-003 m
Sizing	
Use Adaptive Sizing	Yes
Resolution	Default (2)
Mesh Defeaturing	No
Transition	Slow
Span Angle Center	Fine
Initial Size Seed	Assembly
Bounding Box Diagonal	6,6667e-002 m
Average Surface Area	5,3022e-005 m ²
Minimum Edge Length	2,2363e-005 m

Figure 4.26 Mesh Details.

of refinement necessary is considerable, it is mandatory to make the Span Angle Center fine.

Given the geometry of the involute profile and its curvature, Mesh Defeaturing, which would remove features smaller than the value selected, is disabled. A Defeature Size option would appear otherwise, but it is not relevant here [26].

It is widely known that complex geometries benefit from tetrahedral elements to be fully and more easily discretized. However, a structured mesh is much harder to obtain in such cases and these elements are more susceptible to problems such as shear locking. Throughout the testing phase, the simulations manifested a better behavior in the transition between the refined and non-refined zone by generating a tetrahedral mesh, which justifies the patch conforming method adopted and that will be discussed alongside the remaining choices for the mesh generation. The refined zone, which includes the contact elements presented earlier, consists of hexahedral elements only: this leads to an even discretization of the contact surface both along the line of action and along the width of the gear and greatly improves the results output and their post processing and analysis, if discrete lines or points on the model are the object of analysis.

However, throughout the testing phase, a mesh consisting of quadratic tetrahedral elements and linear hexahedral elements was implemented to provide a better understanding

on whether this measure would compromise the results or end up saving resources. The output desired manifested little to no deviation and the stress distribution on the model was acceptable. Provided the aim of the study is not the value of stresses developed throughout the contact, this mesh configuration was adopted. This led to the appearance of quadratic pyramid elements. These elements establish the connection between linear hexahedra and quadratic tetrahedra. Studies [25] show that these elements provide much better transitions and allow a conforming mesh. This measure grants a quality mesh despite the lower order of the majority of the hexahedral elements. The applied mesh features, Edge Sizings, to provide better control of the number of elements and guaranteeing a structured mesh by keeping opposite sides of the partition with the same amount of divisions is shown in Fig. 4.27. The model is then meshed with:

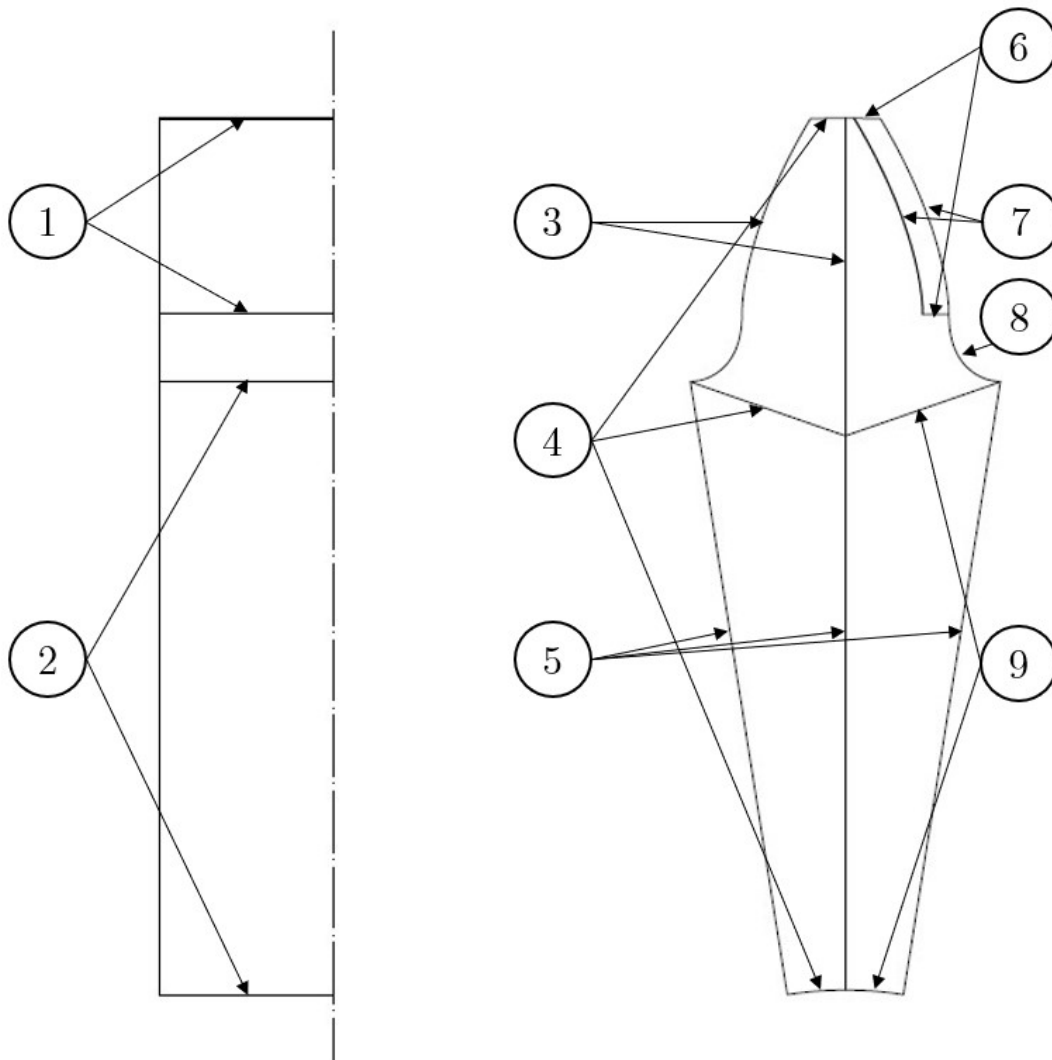


Figure 4.27 Edge sizings applied to generate the mesh.

1. Non refined region width sizing, 14 divisions;

2. refined region width sizing, 35 divisions;
3. Edge sizing with 55 divisions;
4. Edge sizing with 15 divisions;
5. Edge sizing with 30 divisions;
6. Edge sizing with 35 divisions;
7. Edge sizing with 85 divisions;
8. Edge sizing with 25 divisions;
9. Edge sizing with 30 divisions.

The final configuration of the mesh is shown, in Fig. 4.28. Each separate partition is shown in Fig. 4.29. In Fig. 4.29a, the upper left partition is shown, being meshed with linear hexahedral elements. In Fig. 4.29b, the upper right partition, which is meshed with tetrahedral quadratic elements is shown. Fig. 4.29c shows the lower left partition, meshed with linear hexahedral elements and Fig. 4.29d shows the lower right partition, meshed with the same type of elements. The extra part, added to all the models through Revolution, is shown in Fig. 4.30 and is also meshed with linear hexahedral elements. In the final mesh configuration, the hub and tooth flank without contact are left with rather bigger elements. Fig. 4.31 shows the final mesh on the refined region. Since the bias factor that was initially applied to the refined region lead to aspect ratios that compromised simulations, it was completely removed. As such, no edge sizing on the model has bias in the number of divisions. Fig. 4.32 shows the improvement of the aspect ratio when the bias is removed. The existing bias leads to a maximum aspect ratio on the refined region of 16.591, which is excessive on the most loaded area of the model, and removing the bias leads to an aspect ratio of the elements of about 6.6 throughout the whole refined region.

Fig. 4.33 shows the stress distribution in one of the starting models. For comparison, Fig. 4.34 shows the stress distribution on one of the final models. Even though the stresses are not a focus of this study, a superficial comparison of the developed contact stresses was employed and the relative error when compared to the Hertzian contact model changed from about 80% in the earlier stages to about 5% in the final stages.

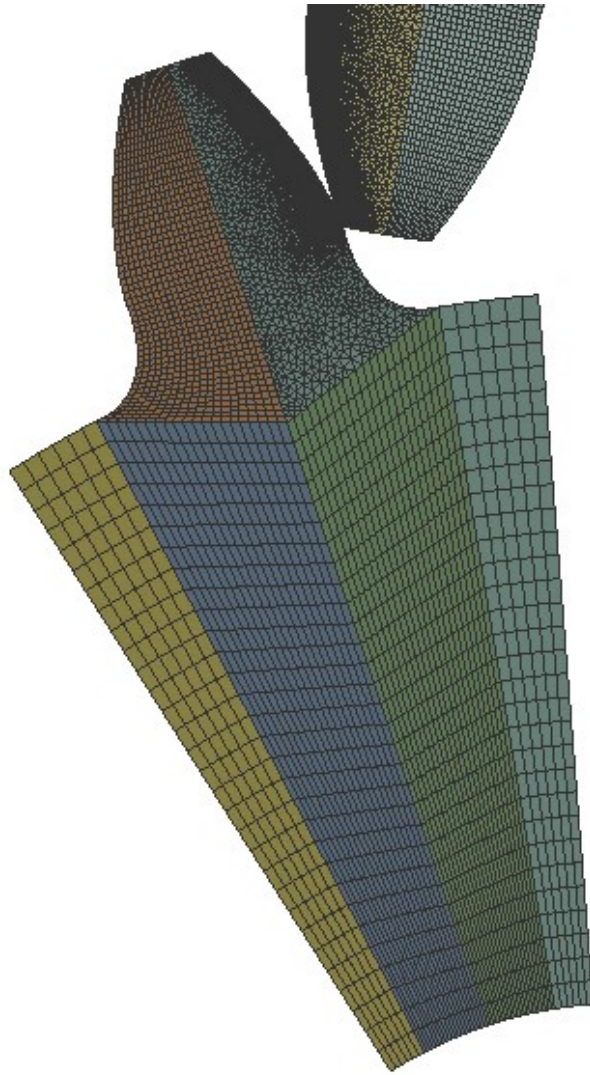
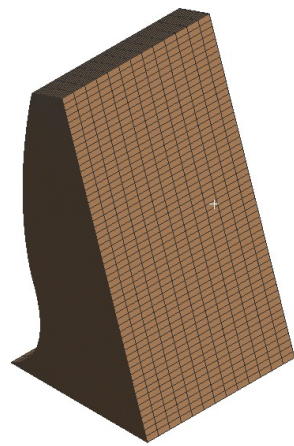
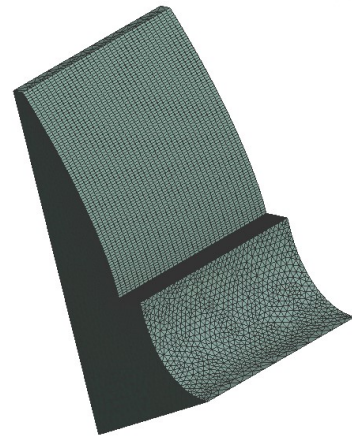


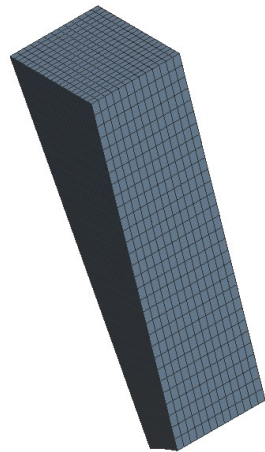
Figure 4.28 Final mesh configuration on the pinion.



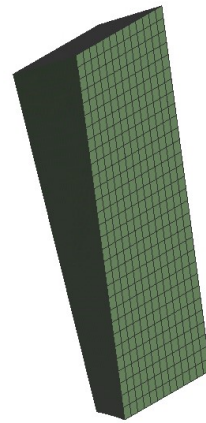
(a) Top left partition



(b) Top right partition



(c) Bottom left partition



(d) Bottom right partition

Figure 4.29 Different partitions into which the geometry is divided.

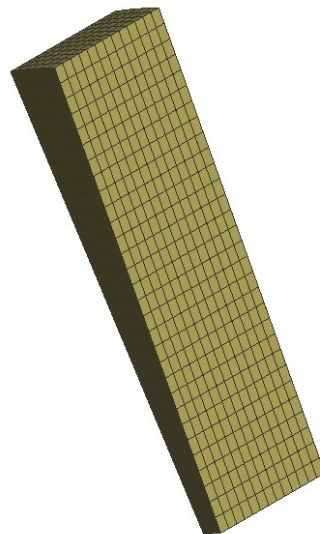
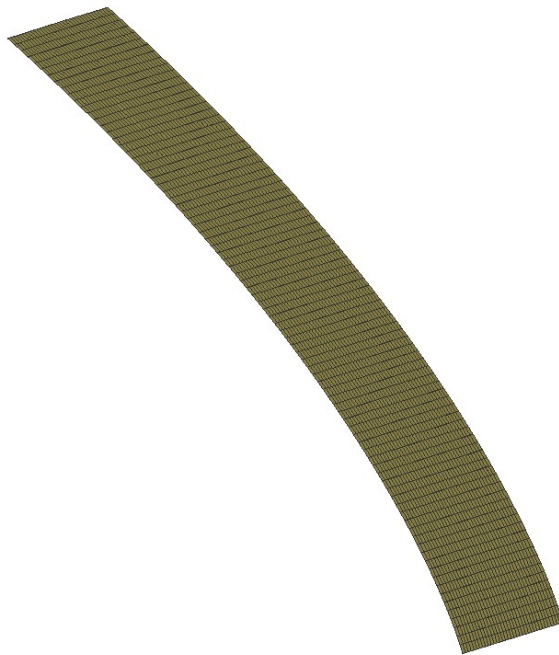


Figure 4.30 Additional partition added through revolution.

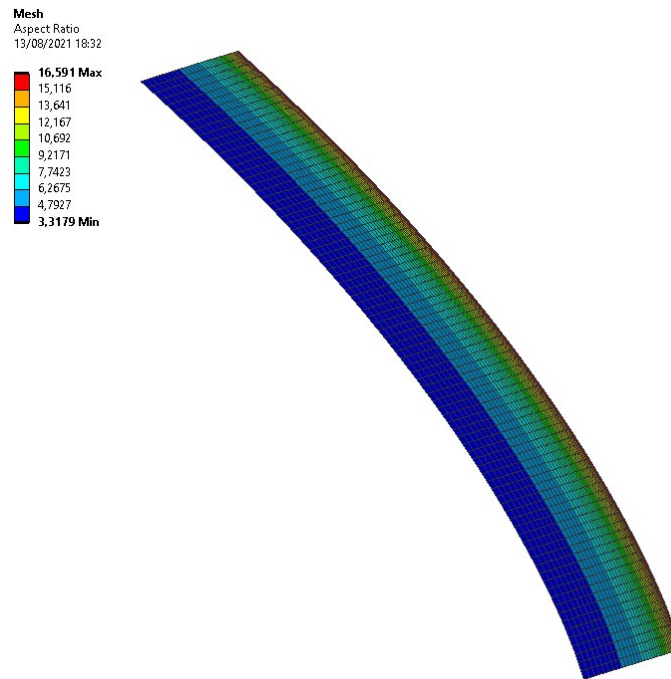


(a) Isometric view of the discretized refined region

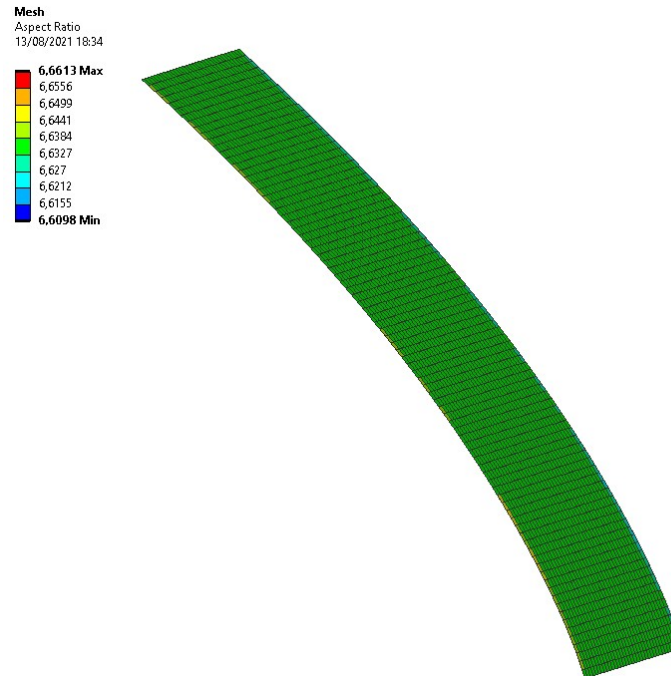


(b) Side view of the discretized refined region

Figure 4.31 Refined region mesh.



(a) Side view of the refined region with a bias factor of 5



(b) Side view of the refined region without bias

Figure 4.32 Influence of the bias factor on the aspect ratio of the elements.

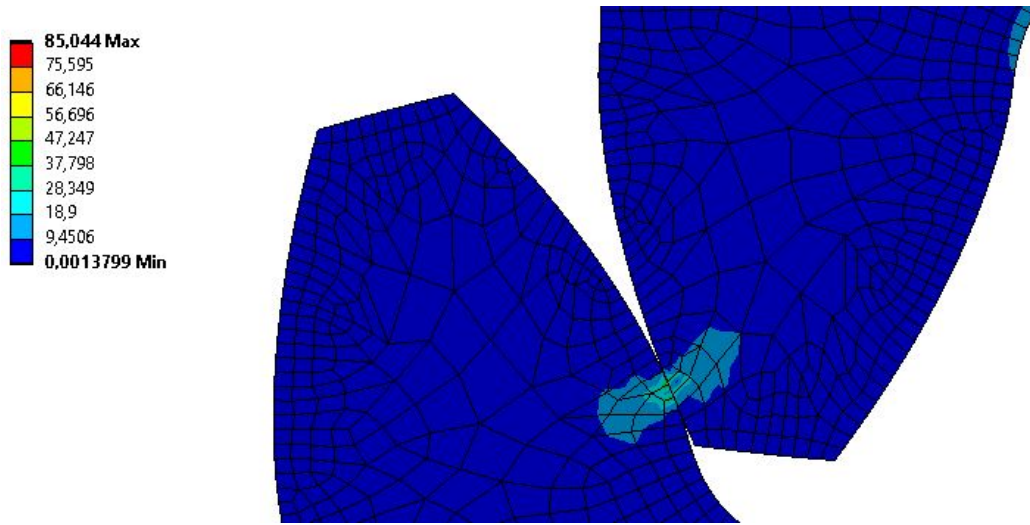


Figure 4.33 Von-Mises Stress distribution on the initial models in MPa.

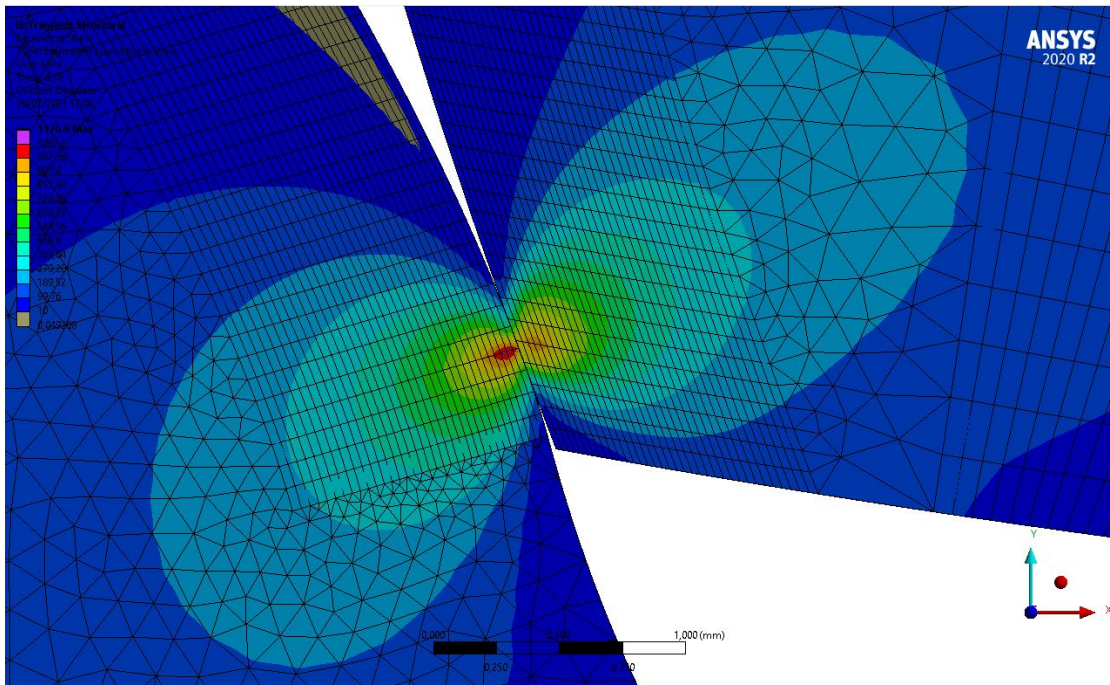


Figure 4.34 Von-Mises Stress distribution on the final models.

4.3.4 Solution and Results

Before running the simulation, the Analysis Settings adopted are summarized in Fig. 4.35. Since the boundary conditions and applied loads do not change throughout the simulation, a single step is enough. Its definition should be set to Substeps, allowing the number of substeps to be manually chosen by disabling the Auto Time Stepping. The Time Integration is turned off to accomplish the same goal as the simplification employed in the equations 3.24 and 3.25. Alongside this adjustment, the Large Deflection option is enabled and the Weak Springs are turned off, being useful and necessary only in particular cases. The *Software* provider recommends keeping Large Deflection option activated at all times except in the few cases when the deflection phenomena are considerably small. The Moderate Speed Dynamics option is selected, making it necessary to add a damping coefficient in the contact details, with a value of 0.05. This value was kept constant for all the simulations.

Finally, depending on the desired results, the Output Controls ought to be adjusted to properly provide the data that better fits the user's goals. In this study, Surface Stresses, Contact Data and Nodal Forces play a major role in the parametric analysis that follows the numerical simulation. The value of the rotation speed and torque are only assigned at this stage. Figs. 4.36a and 4.36b show the details of the joints at the point where these values must be introduced.

In order to fully analyze the contact evolution, an appropriate value of the rotational speed is required. The angular velocity, associated with the value of the Step Time, must match the angle of the arc associated with the length \overline{AB} , keeping in mind the involute geometry and its inherent relations. This angle can be calculated exactly as shown in Eqs. 4.1 to 4.4,

$$\gamma = \phi - \phi_1 \quad (4.1)$$

$$\phi = \arctan\left(\frac{\overline{T_1B}}{r_{b1}}\right) \quad (4.2)$$

$$\overline{T_1B} = \overline{T_1A} + \varepsilon_\alpha \cdot p_b \quad (4.3)$$

$$\gamma = \arctan\left(\frac{\overline{T_1A}}{r_{b1}}\right) \quad (4.4)$$

Fig. 4.37 shows the schematic that allows the quantities to be visually understood. For a rotational speed of 0.09 rad/s, Eq. 4.5 allows the determination of the total simulation time.

$$\omega = \frac{\phi_1}{t} \quad (4.5)$$

The value of the rotation speed must be kept very low to validate a quasi-static analysis, which is the case in the present work. The value of the simulation time must be adjusted for each geometry, seeing that γ is calculated with parameters that depend on the changes verified for many models. It is advised to keep the chosen Step Time value slightly smaller

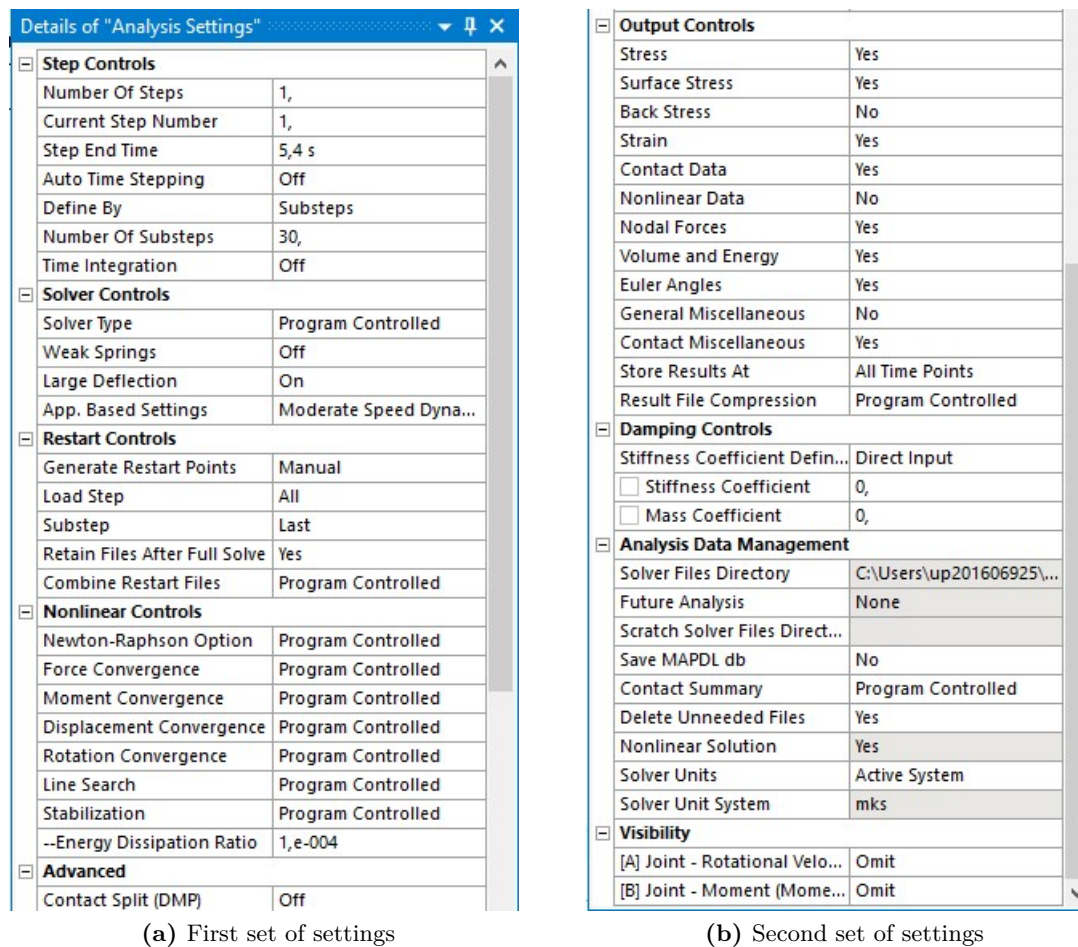


Figure 4.35 Analysis settings.

than that which is calculated in order to prevent unrestricted motion in the final instants of the simulation and lead to failure of the simulation. Fig. 4.38 shows the consequences of neglecting such detail in the developed model.

It is not uncommon for the total structure error to reach values of about 20 mJ in cases where this happens.

The selection of the resistant torque is a crucial aspect of the setup. If the value chosen is too small, numerical problems, namely *contact chattering*, may occur. This problem is also associated with the normal penalty contact stiffness, **FKN**, values being too high. This problem may often compromise the whole analysis. A very common error, elements turning inside out, occurs when the load, locally, induces loads that distort the elements excessively. Those elements would, then, lose their shape, which would compromise the simulation. There are several possible causes: either the boundary conditions are not properly defined, the element quality, mainly in respect to aspect ratio, is poor or not high enough to withstand the effects of the load and/or the number of nodes is lower

Details of "Joint - Rotational Velocity"	
Scope	
Joint	General - Ground To Pinion Hub
Definition	
DOF	Rotation Z
Type	Rotational Velocity
<input type="checkbox"/> Magnitude	-9,e-002 rad/s (step applied)
Lock at Load Step	Never
Suppressed	No

(a) Pinion joint

Details of "Joint - Moment"	
Scope	
Joint	General - Ground To Gear Hub
Definition	
DOF	Rotation Z
Type	Moment
<input type="checkbox"/> Magnitude	-100, N·m (step applied)
Lock at Load Step	Never
Suppressed	No

(b) Gear joint

Figure 4.36 Assigning values of torque and rotation speed.

than what was necessary. Having aspect ratios lower than 10 for the elements that make up the refinement region prevented it from happening at that location. The rest of the model, having a lower local load applied than the previously mentioned elements, showed a better tolerance to that mesh metric. A maximum empirical threshold value of 30 was preserved as the simulations were progressing as a result of the number of them that failed to converge and the debugging process they necessarily went through. Naturally, the *Software Provider* highly recommends that the unconverged solutions are strictly used for debugging purposes, which renders them useless for any other goal than to finally reach convergence.

The results for post processing are then obtained in spreadsheet form in the Workbench environment/window when the adequate probe was selected, where a value of the relative rotation for each body is obtained for each substep and a value of the torque is obtained the same way for the same substeps. The main values that the model is implemented to provide can be obtained from the Probe option, selecting the Relative Rotation. Two different Probes are created: one for the pinion relative rotary displacement and a similar one for the gear. The probes should be defined as shown in Fig. 4.39, selecting the other joint for the gear case. To evaluate the stresses associated with the transmission error, an extra Probe is created for the Equivalent Stress. A probe for the torque in the pinion is also necessary to allow the calculation of the gear mesh stiffness.

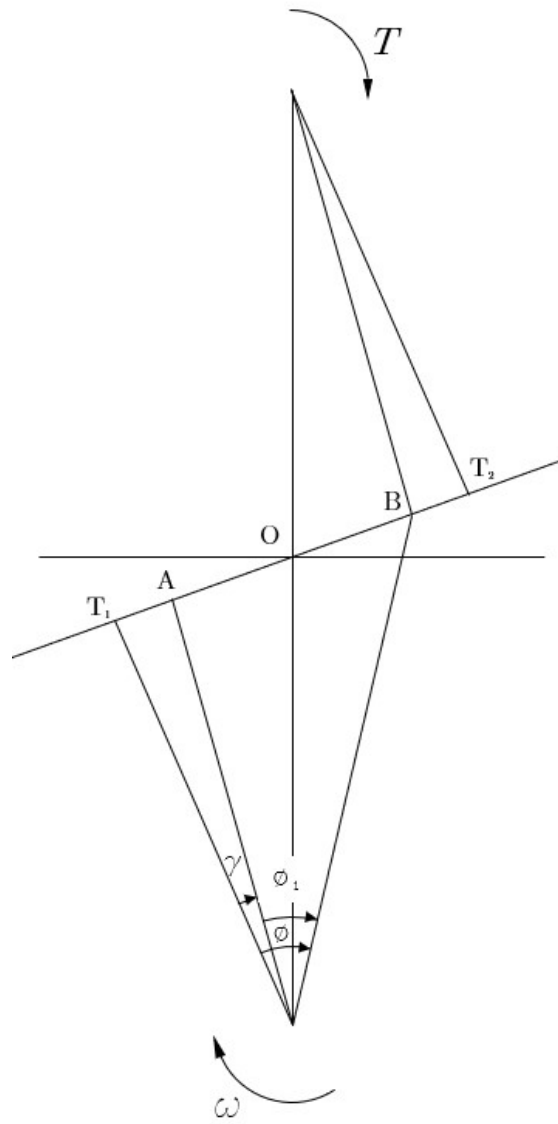


Figure 4.37 Meshing schematic.

4.3.5 Special Cases

For the models with a transmission ratio different than 1, I2 and I3, the error that occurred in the zone shown in Fig. 4.10 happened even when a small amount of additional material was added. After many values of torque tested, refined region configurations and local refinements on the error zone, the only way of achieving convergence was keeping the whole hub, as shown in Fig. 4.40. Although this measure solved the convergence problem, it can be seen in Fig. 4.41 that the structural error has its maximum value at the location where the convergence error occurred. This is an indicator that, if this region was being analyzed, the refinement of the mesh, locally, should be enough to lower value of this structural error. Some models, having a smaller thickness at the tooth tip, namely K02 and PROF112, had their refined region reaching the vertical line dividing the

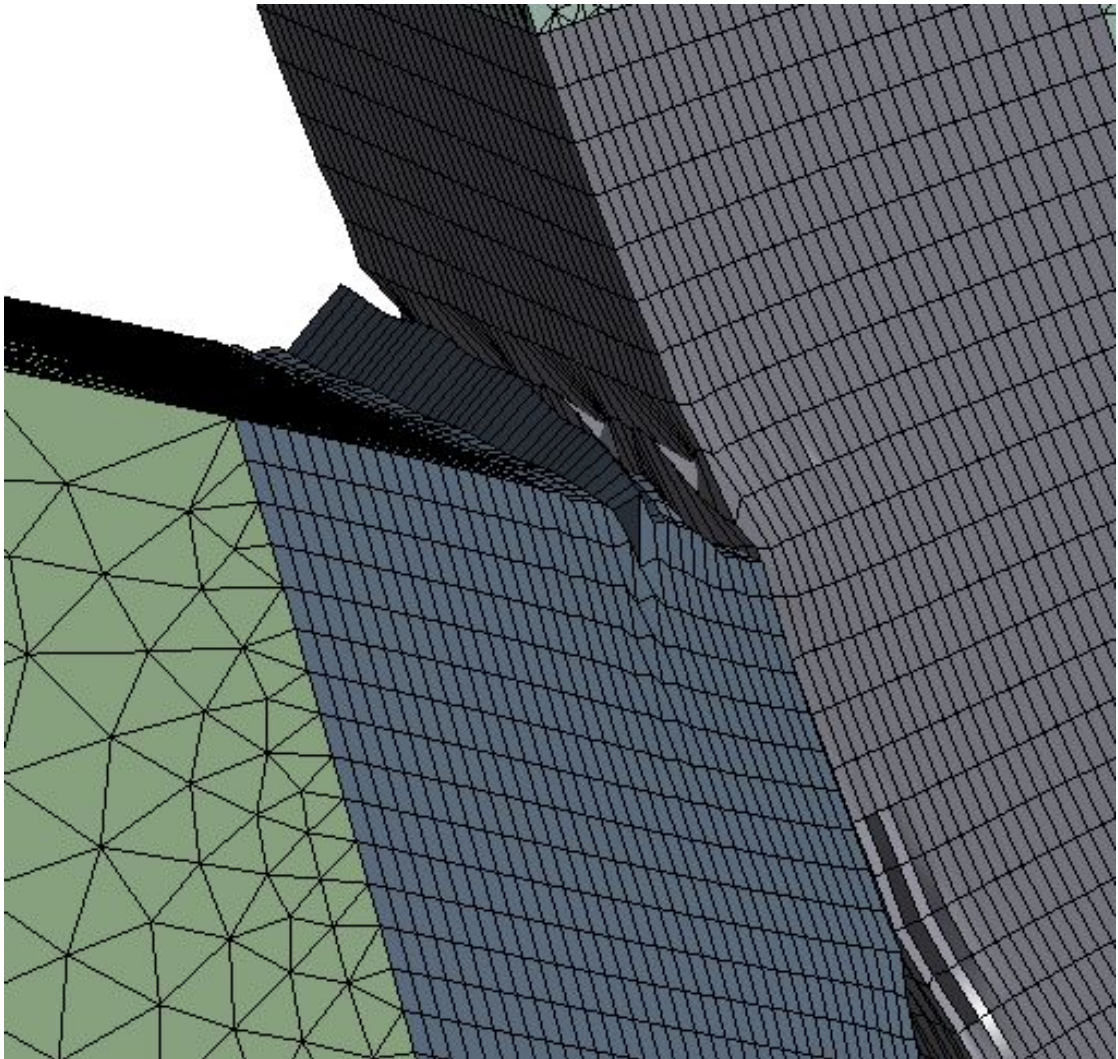


Figure 4.38 Abnormal distortion of the mesh.

Details of "Relative Rot. Pinion"	
Definition	
Type	Joint Probe
Boundary Condition	General - Ground To Pinion Hub
Orientation Method	Joint Reference System
Orientation	Reference Coordinate System
Suppressed	No
Options	
Result Type	Relative Rotation
Result Selection	Z Axis
<input type="checkbox"/> Display Time	End Time

Figure 4.39 Relative rotation probe details for the pinion.

partitions of the tooth, like the example shown in Fig. 4.42. In such cases, the aspect ratios of the tetrahedral elements on the partition close to the refined region would reach unacceptable values (empirically, over 35 on a non directly loaded region). To overcome that problem, the refined region was adjusted as shown in Fig. 4.43. This way, most of the

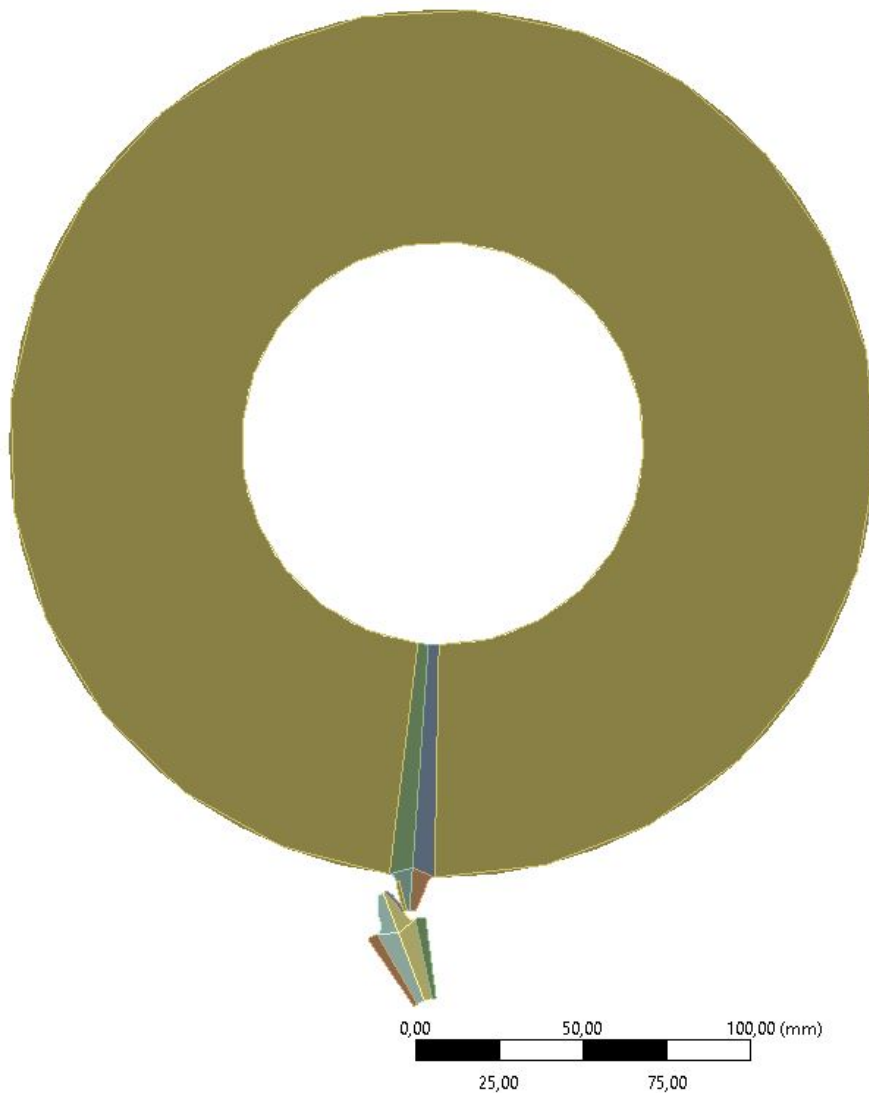


Figure 4.40 Preserved body of the gear with 60 teeth.

high stresses would still fall on the refinement region and the aspect ratio of the elements would remain acceptable. The modified refined region can be obtained from the original refined region in the Design Modeler by merely cutting the original and merging the top cut part with the tetrahedral mesh partition. The cut can be performed through a plane that is perpendicular to the tooth flank and contains the top edge on the side of the refined region.

4.3.6 Validation

The validation requires a verification of the developed contact stresses and their comparison with the values calculated through the Hertzian contact model, which was presented earlier. As said, the final models reached relative errors with values around 5%, which is enough to validate the model. Another metric is the structural error.

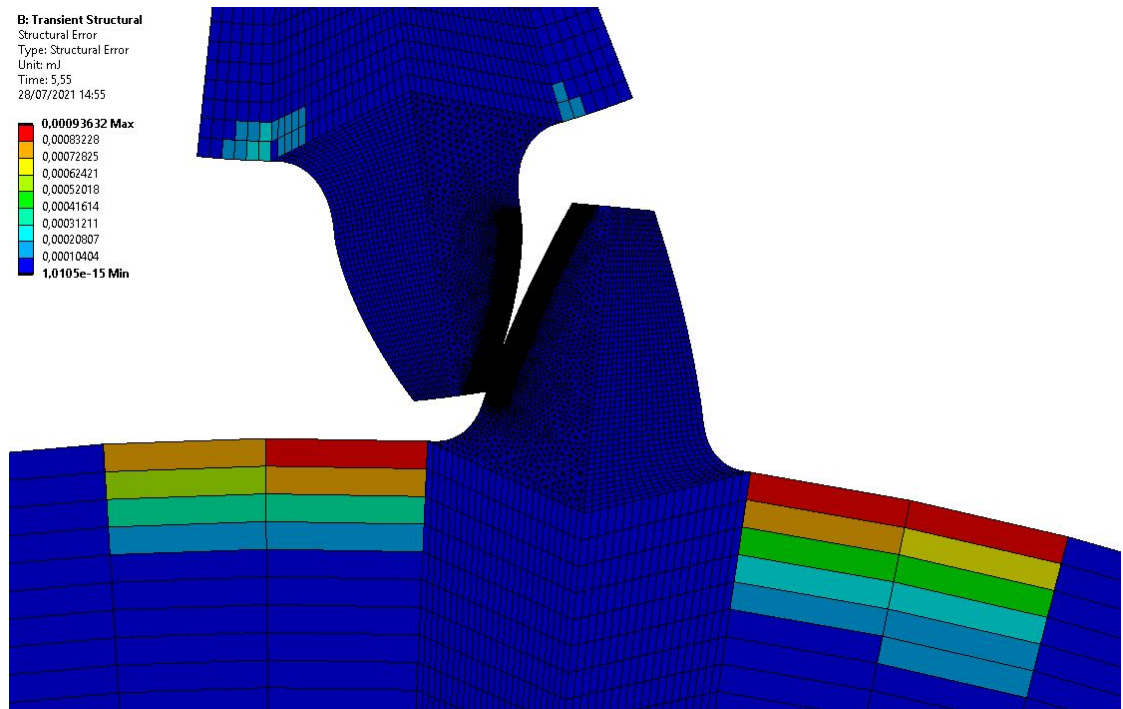


Figure 4.41 Structural error of the body of the gear with 60 teeth.

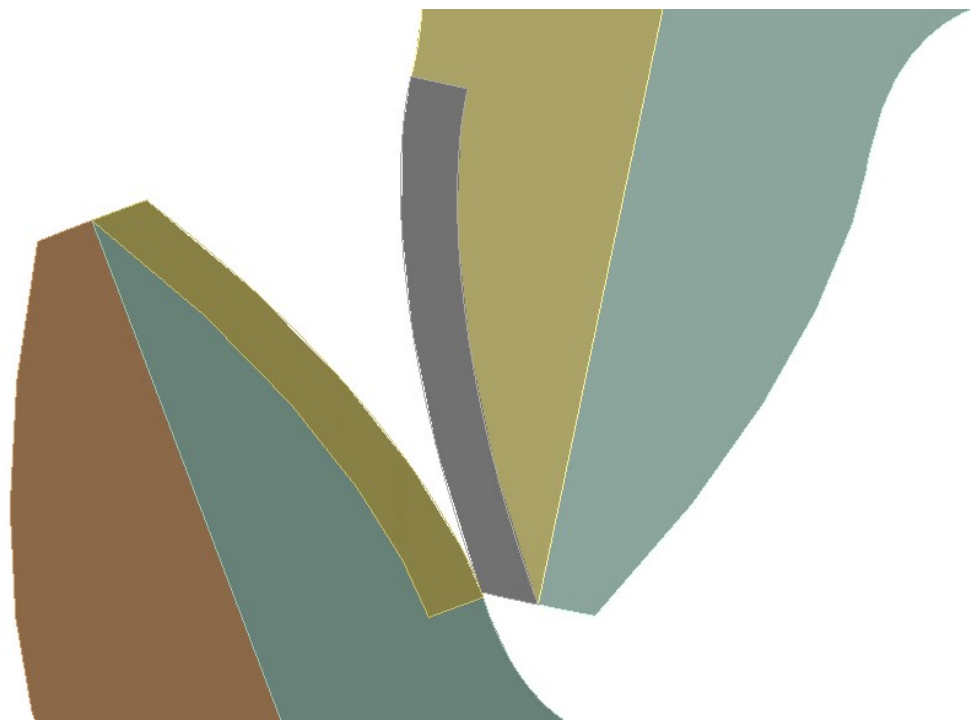


Figure 4.42 Model with a refined region intersecting the central partition section.

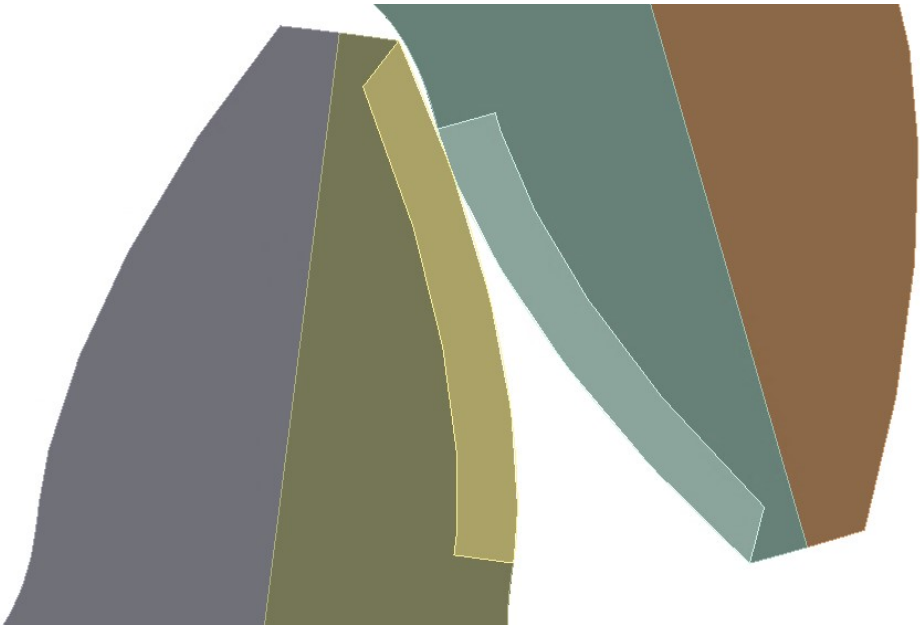


Figure 4.43 refined region modification.

4.3.6.1 Structural Error

For Displacement-Based problems, category into which the problem at hands fits, the *ANSYS* software approximates error with a similar technique to the one given by Zienkiewicz and Zhu [27] and the theory behind it is presented in Appendix A.

Empirically, it was seen that models that converged without issues had total values of this error that did not exceed 10^{-1} mJ.

Models that converged but did require some attention or had previous convergence errors have values of about 1 mJ or slightly higher, to which is recommended some attention. This became the maximum tolerable value for all the models.

Finally, models that did not converge or behaved abnormally manifested total errors of about 20 mJ. This value is unacceptable and the simulations where they occurred were discarded. Those were altered until the error value was within tolerable limits, the two mentioned above.

The validation also requires a verification of the developed contact stresses and their comparison with the values calculated through the Hertzian contact model, which was presented earlier. As said, the final models reached relative errors with values around 5%, which is enough to somewhat validate the model.

This page was intentionally left blank.

Chapter 5

Results and Discussion

In this chapter, the results and their respective discussion are included. Abnormal results and the influence of the input parameters are evaluated in order to reach some conclusions regarding the setup implemented and proposed values of \mathcal{R} in the literature analyzed. The result treatment is handled at first, including a relevant coordinate shift. Finally, the discussion of the obtained results is presented.

5.1 Results

The results for the standard gear are presented to exemplify what kind of curves are expected to be obtained. Some other results are presented since they require further explanation or discussion. The curves corresponding to models that behaved according to the expectations and did not manifest relevant particularities are contemplated in Appendix B.

5.1.1 Coordinate Shift

To maintain consistency, the time coordinate must be converted into the ξ coordinate presented alongside the analytical model to be calibrated. This can be easily done by trigonometric relations on the gearing schematic shown in Fig. 5.1. Both x and t are linear quantities and therefore a relation can be established. By analyzing the triangle defined by the points T_1 , A and the center of rotation of the pinion, the relation presented in Eq. 5.1 can be established.

$$\tan(\gamma + \omega t) = \frac{\overline{T_1 A} + x}{r_b} \quad (5.1)$$

Recalling that the ξ coordinate can be associated to x , length along the line of action, through Eq. 5.2,

$$x = \xi \cdot p_{bt} \quad (5.2)$$

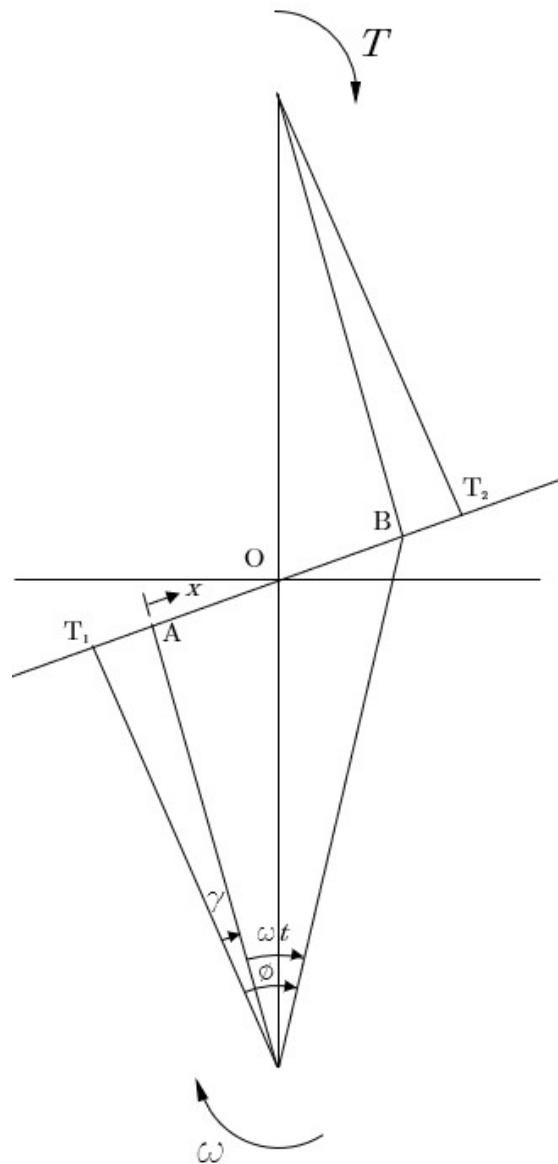


Figure 5.1 Schematic for the coordinate shift.

the variable ξ can be obtained through t by the expression presented in Eq. 5.3.

$$\xi = \frac{r_b \tan(\gamma + \omega t) - \overline{T_1 A}}{p_{bt}} \quad (5.3)$$

5.1.2 M4_5

Fig. 5.2 shows the transmission error and mesh stiffness distributions with the ξ coordinate for the M4_5 model and Fig. 5.3 shows its normalized mesh stiffness distribution in relation the maximum value verified. The mesh stiffness is calculated from the transmission error through the relations established in Eqs. 3.27 and 3.28. Since the pinion is equal to the gear, which happens to most of the studied models, a symmetric behavior of

the transmission error and mesh stiffness is expected. Regarding the numerical errors, the selections made during the convergence study should keep them under control, but not make them disappear completely.

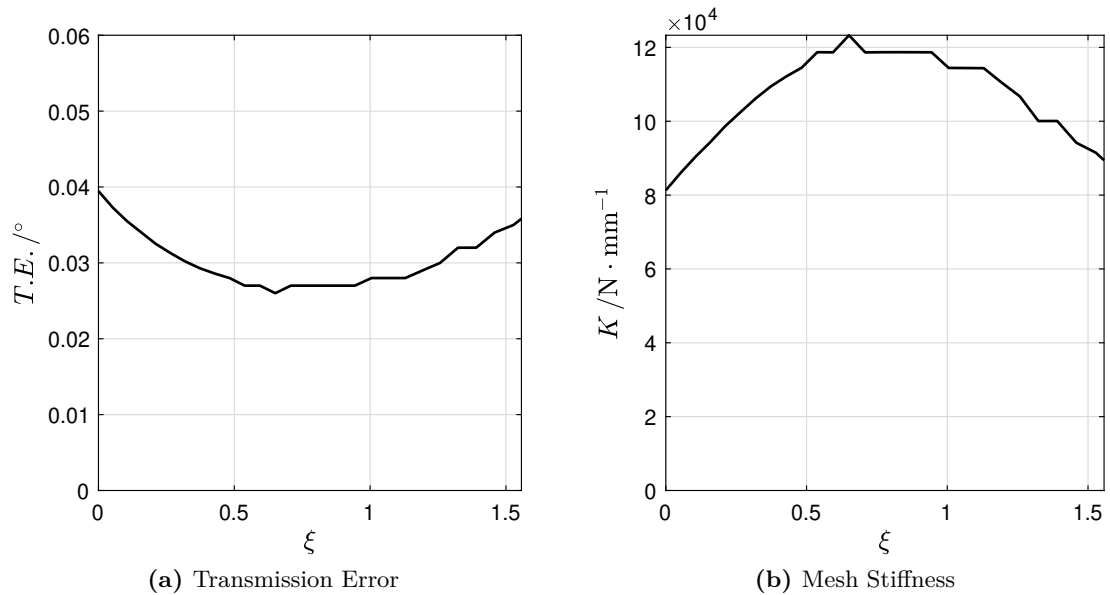


Figure 5.2 Numerical results of the M4_5 model.

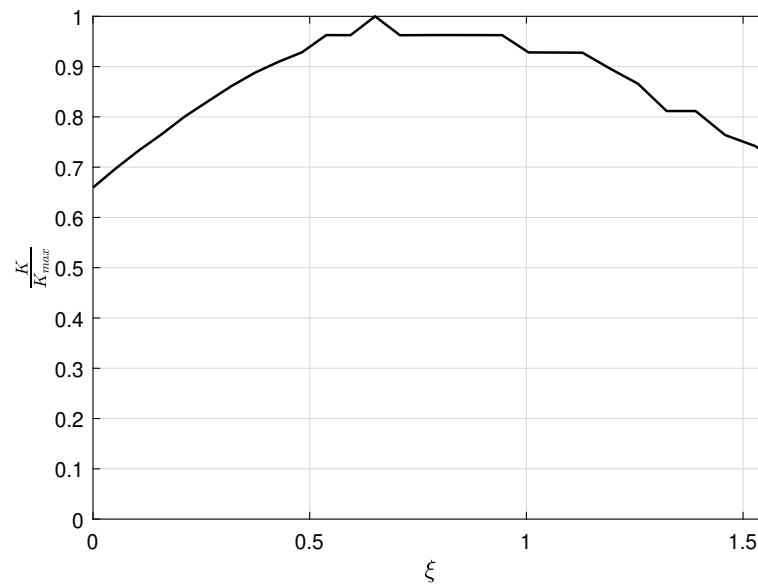


Figure 5.3 Normalized mesh stiffness of the M4_5 model.

5.1.3 ER1

Fig. 5.4 shows the transmission error and mesh stiffness distributions with the ξ coordinate for the ER1 mode and Fig. 5.5 shows the normalized mesh stiffness distribution

for that same model. From the presented curves and in comparison to the other curves

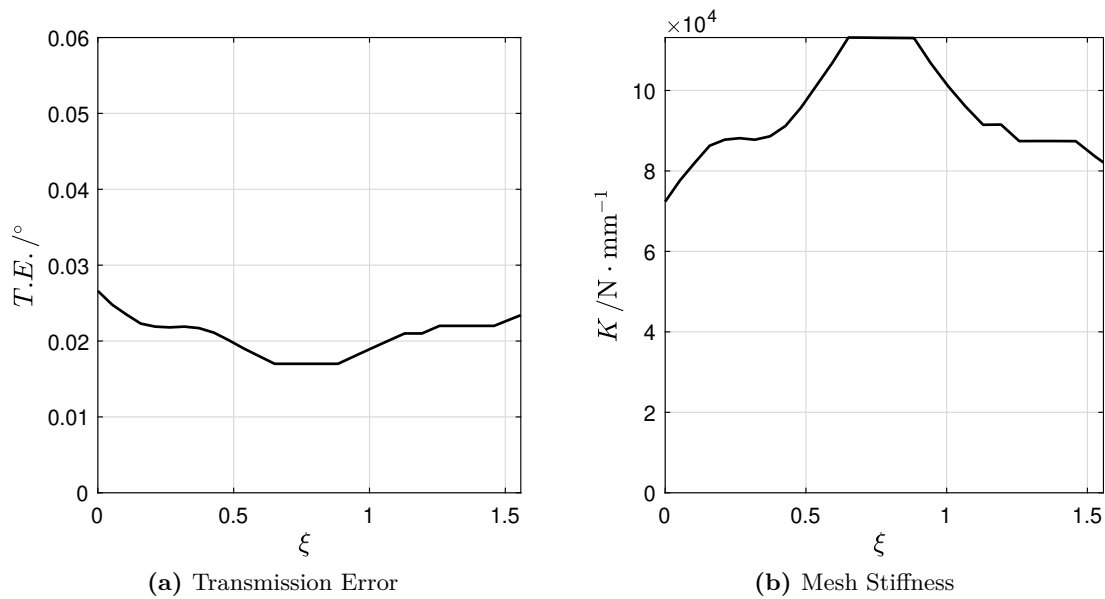


Figure 5.4 Numerical results of the ER1 model.

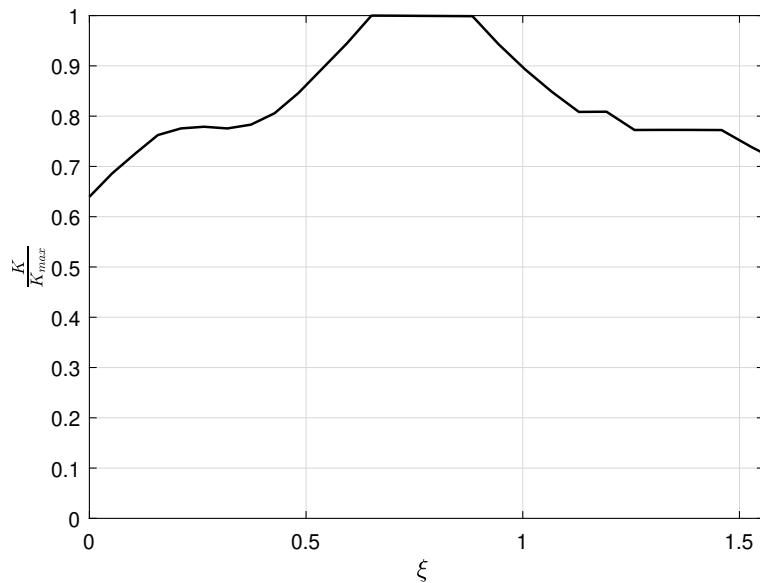


Figure 5.5 Normalized mesh stiffness of the ER1 model.

obtained, or rather the ones obtained for the standard gear, this result deviated from the expectations. Instead of a parabolic behavior, the transmission error and consequently the mesh stiffness followed a curve with a trapezoidal shape in the middle of the contact path. The first step towards verifying its validity was the value of the structural error. The models that converged properly, up to this point, had structural errors that did not exceed 10^{-3} mJ. Since the same happened to this model, something else was causing the inaccuracy, in case this behavior was not realistic. By checking the torque, its values

along X and Y were not zero, as shown in Fig. 5.6, which is not the expected result. In

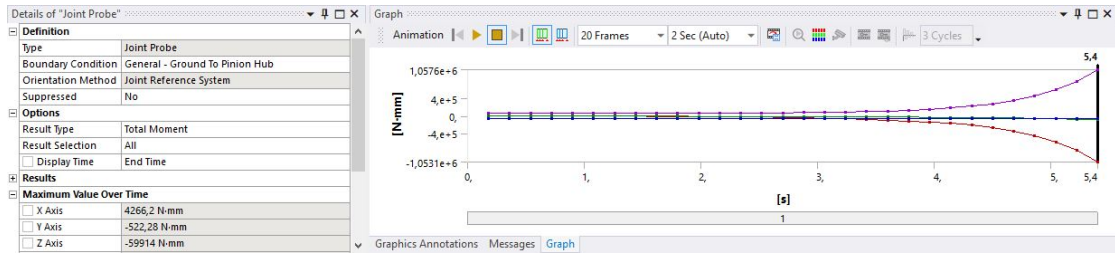


Figure 5.6 Torque along the X, Y and Z directions for the initial simulation.

the same model, the contact status, as shown in Fig. 5.7 showed that there was a region without contact between two other regions where contact was happening. The red region shows where the contact between the two bodies is happening and the green region shows where the the contact is not happening. To understand the origin of these issues, an-

B: Transient Structural

CONTSTAT

Expression: CONTSTAT

Time: 5,055

30/07/2021 11:58

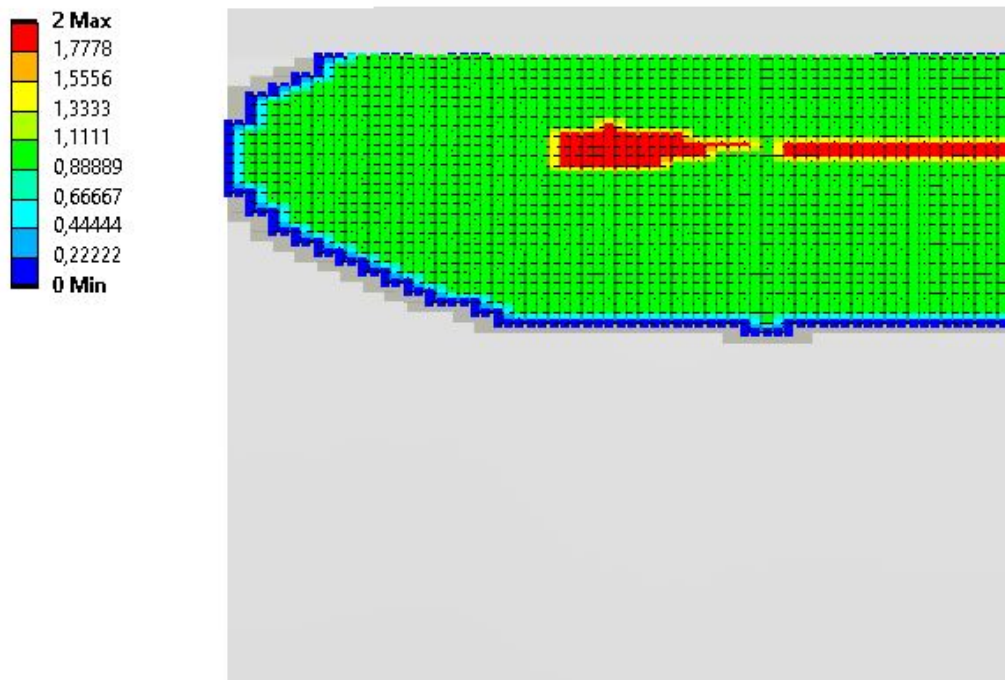


Figure 5.7 Contact status of the initial simulation of the ER1 model.

other model was prepared, with a more refined mesh on the refinement region For that model, the torque values on the pinion are shown in Fig. 5.8. Since the values are significantly lower, one can safely, to some degree, say that the previous issues were due to some numerical problem in the mesh. The contact status also improved, as can be seen in Fig. 5.9.

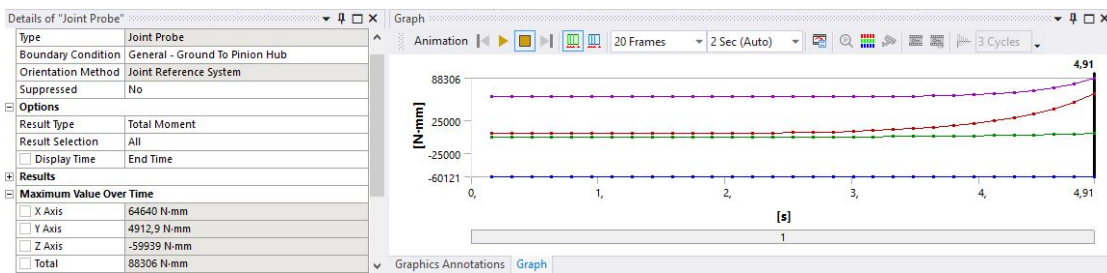


Figure 5.8 Torque along the X, Y and Z directions for the refined simulation of the ER1 model.

B: Transient Structural
 CONSTAT
 Expression: CONSTAT
 Time: 4,91
 30/07/2021 15:10

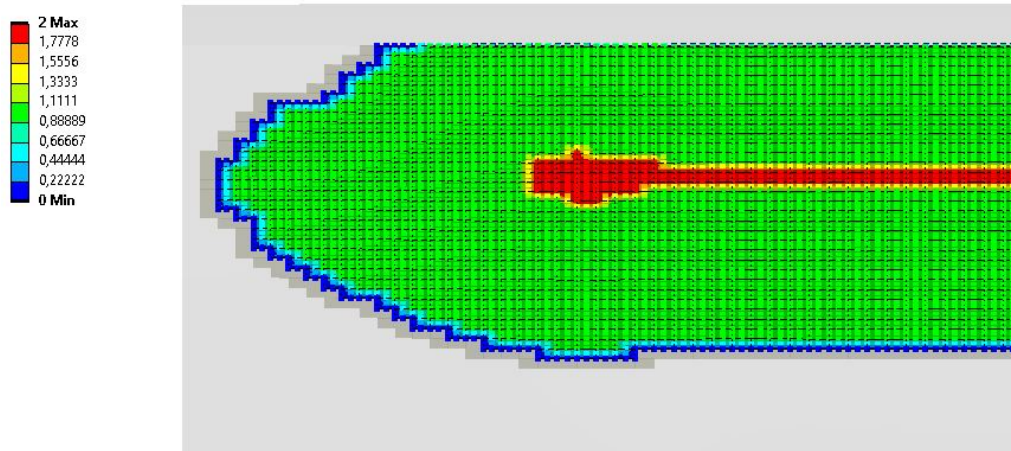


Figure 5.9 Contact status of the refined simulation of the ER1 model.

That being said, the results obtained may depict what happens in models with end relief modifications applied. As follow up, it is important to explain this behavior and understand why it happens. A gear pair with a width equal to that of the width in contact when end relief is applied would behave in a different way, necessarily. This happens because there is a convective effect associated with the excess material that exists when in the end relief case, even though it plays no active part in the contact region. In a FEM model, this would be a consequence of elements in the stiffness matrix outside its main diagonal.

5.1.4 ER2

This model showed a very similar behavior to the ER1 model. Once again, Fig. 5.10 shows the transmission error and mesh stiffness curves and Fig. 5.11 shows the normalized mesh stiffness distribution also in relation the maximum value verified.

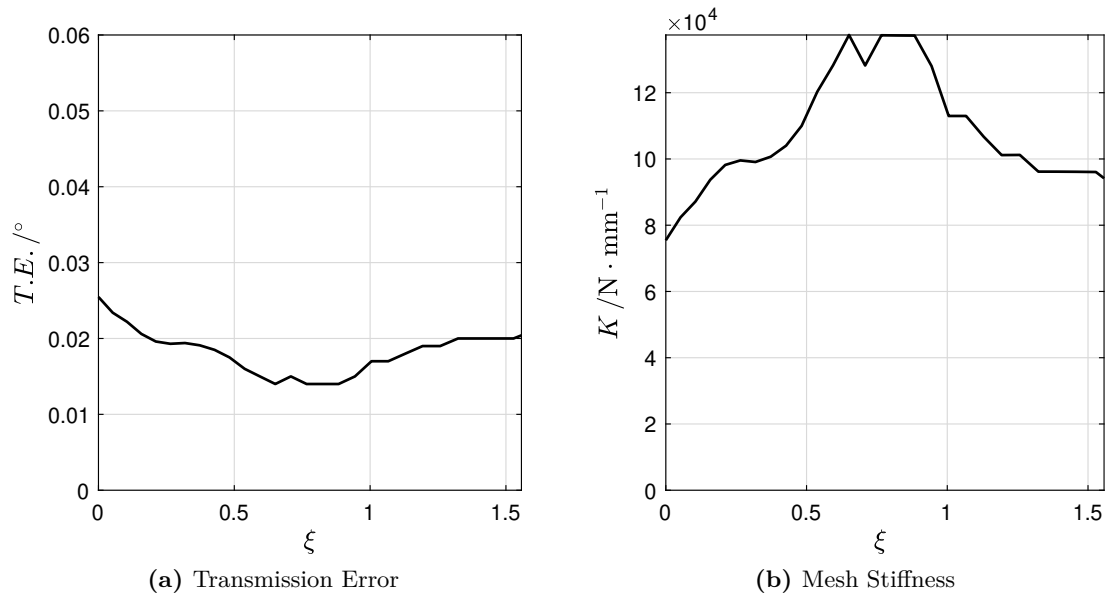


Figure 5.10 Numerical results of the ER2 model.

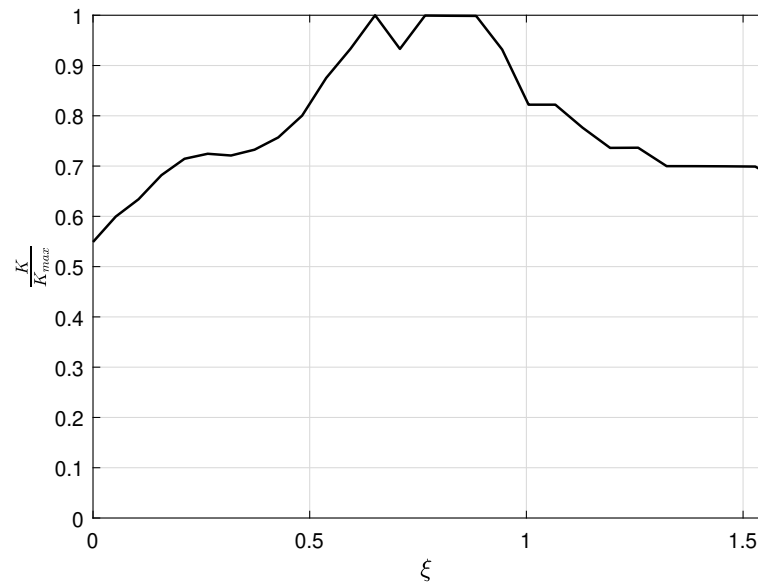


Figure 5.11 Normalized mesh stiffness of the ER2 model.

5.1.5 ER1M45

To further investigate this abnormal behavior, a model containing a gear with an end relief on the pinion position and a gear with the dimensions of the standard gear on the gear position was implemented. Figs. 5.12 and 5.15 show the same curves presented for the previous models. The curves show a behavior that resembles the models with end relief on both gears, but closer to a parabola than both of them. A gear pair with a width equal to that of the width in contact when end relief is applied would behave in a different way, necessarily. This happens because there is a convective effect associated with the excess

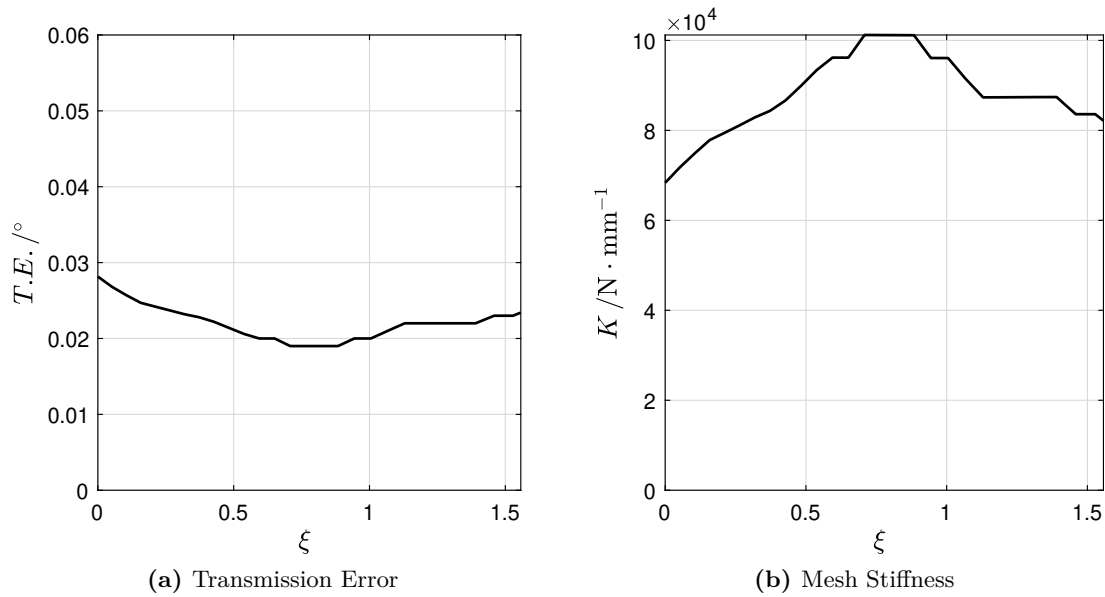


Figure 5.12 Numerical results of the ER1M45 model.

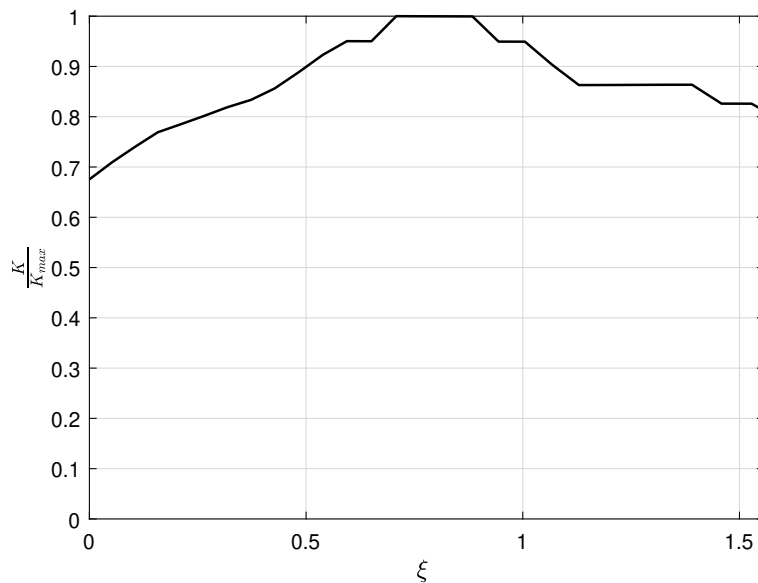


Figure 5.13 Normalized mesh stiffness of the ER1M45 model.

material that exists when in the end relief case, even though it plays no active part in the contact region. Since the structural error was within the empirically established reasonable values, this is, for now, the most plausible explanation for the abnormal behavior. The torque along the X and Y directions was also negligible, which did not appear as a possible issue. Further information concerning this hypothesis can be found in reference [28].

5.1.6 Summary

Table 5.1 summarizes the main results taken from the simulations done. The curves that served as a source for these values are presented in Appendix B.

Table 5.1 Relevant values of the stiffness distributions for the simulated models.

Model	$\alpha_k(\xi = 0)$	$\alpha_k(\xi = \varepsilon_\alpha)$	$K_{\max} \times 10^{-5} / \text{N}\cdot\text{mm}^{-1}$
M1_75	0.6606	0.6804	1.2325
M2_5	0.6620	0.6870	1.2328
M4_5	0.6594	0.6802	1.2329
M8	0.6548	0.7334	1.2328
M12	0.6632	0.7334	1.2328
PROFI11	0.6023	0.6735	1.2791
PROFI12	0.5537	0.7135	1.2768
PROFI21	0.6720	0.7468	1.1050
PROFI22	0.6824	0.7465	1.0018
PROFI31	0.6719	0.7398	1.1448
PROFI32	0.6781	0.7475	1.1448
I2	0.6005	0.7406	2.6940
I3	0.5777	0.7856	4.3244
C20	0.6826	0.7727	1.3108
CORR1	0.7121	0.7177	1.2374
CORR2	0.6909	0.7300	1.2741
K01	0.6023	0.6735	1.2791
K02	0.5530	0.7135	1.2768
ER1	0.6395	0.7256	1.1316
ER2	0.549	0.6804	1.3742
ER1M45	0.6754	0.8117	1.0121
CR1	0.7450	0.8194	0.5963
CR2	0.7297	0.8403	0.4713

The symmetry of the curves can be analyzed considering the proximity of the values of α_k at each value of ξ considered. Some models, made of equal gears on the pinion and gear positions, do present a fairly symmetric behavior. However, some models that share the same property do not, and that may be something worth analyzing, as effects not taken into account may be responsible for such results. Models where material is *added* in comparison to the standard gear manifest a higher mesh stiffness. This does not happen to the gears where the module is changed because everything is scaled, including the load, leading to the same results. It is also worth noting that the value of α_k for $\xi = \varepsilon_\alpha$ suffers some changes throughout these models when it was expected to remain the

same. The increase in mesh stiffness in the models with a different gear ratio is a result of a bigger overall volume without having the teeth overall size varying accordingly. The crowning profile modification models, having a different contact type than all of the other models, may not be analyzed under the same scope. It is believed that in this case, the penetration plays some part in the obtained results and more models with the crowning profile modification should be developed to mitigate this effect and establish a closer comparison. However, the present results are already insightful regarding the expected behavior of models containing this profile modification and are a very useful tool in order to start studying this case with more detail. The end relief profile modification is the aspect that requires the most attention, regarding the geometrical parameters, given the fact that its behavior is the most abnormal. Regarding the remaining models, the results do not deviate much from the expectations concerning the symmetry and maximum stiffness values. As such, the results for all of the models are presented for further analyses and the maximum stiffness is presented for quick comparisons and possible validations.

5.2 α_k parameter

The values presented give valuable information concerning the symmetry of the obtained curves and the maximum values of the gear mesh stiffness. These obtained values can be used for further comparison with other methods, highlighting ISO 6336-1 Method B in this matter. The gears pairs made of equal gears shows a more symmetric behavior, whereas the gear pairs where the pinion is different than the gear show a more asymmetric behavior, which was believed that would happen. Understanding the influence of each parameter on the value of the second column of the Table 5.1 is crucial. From Eq. 5.4, a linear regression of the numerical point for each studied parameter is presented in Fig. 5.14.

$$\alpha_k = a_0 \cdot Y^* + a_1 \quad (5.4)$$

The first information towards determining the influence of each parameter on α_k should be the value of the slope of the linear regression of the numerical values. Then, looking at the numerical values themselves, determine if the information of the linear regression is accurate enough concerning the influence of the parameter. While for most cases the first information is enough, looking at the discrete numerical values for both cases where axial profile modifications are applied, the parameter studied in each of them plays a significant role and therefore its influence must be taken into account.

From this information, it can be seen that:

- the module;
- the root radius factor;

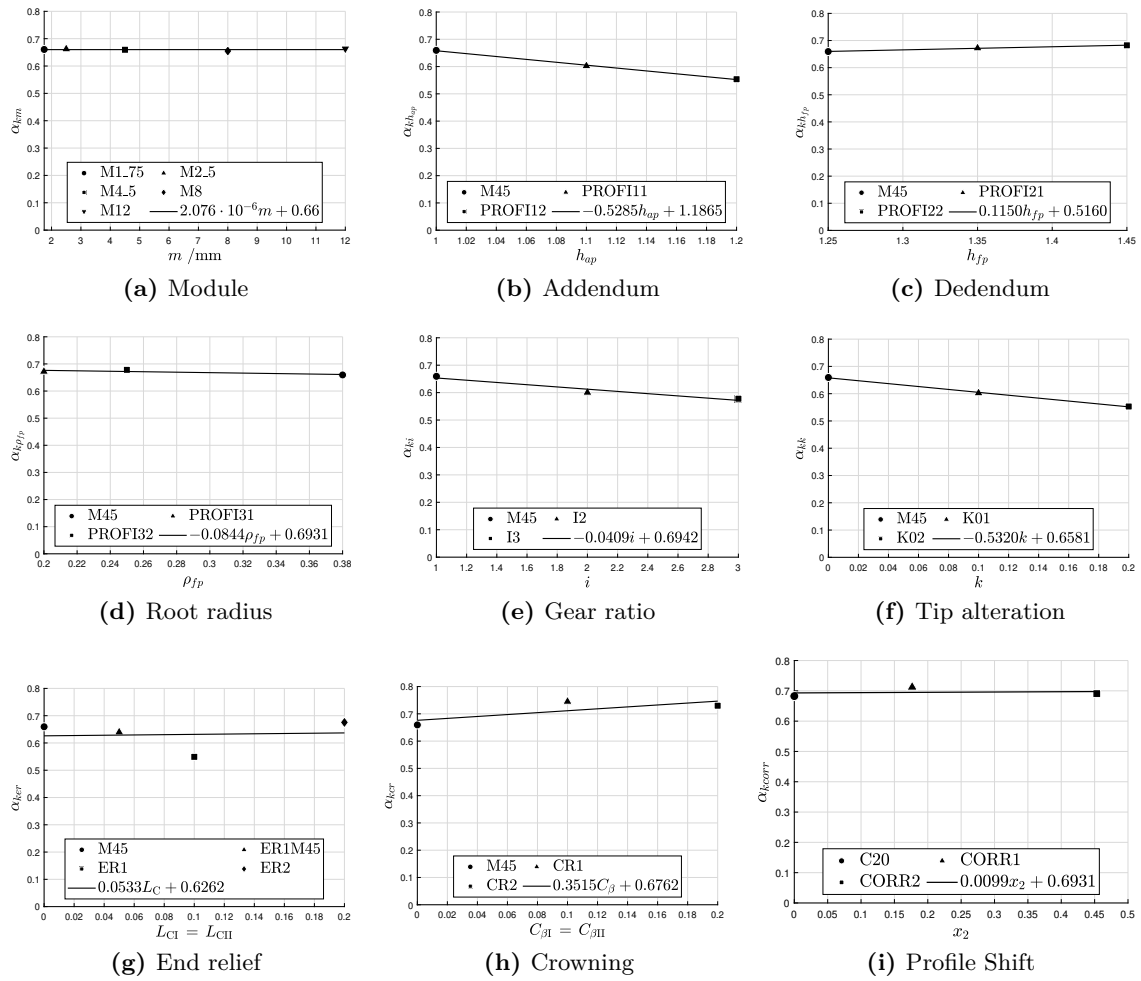


Figure 5.14 Influence of the geometrical parameters on the α_k parameter.

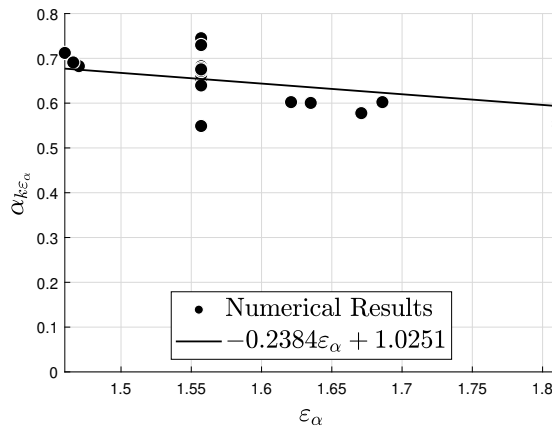


Figure 5.15 Influence of the contact ratio on the α_k parameter.

- the gear ratio;
- the dedendum factor;

Table 5.2 Coefficients for the approximations for the first set of numerical points.

Parameter	a_0	a_1
m	$2.076 \cdot 10^{-6}$	0.6600
h_{ap}	-0.5285	1.1865
h_{fp}	0.1150	0.5160
ρ_{fp}	-0.0844	0.6931
i	-0.0409	0.6942
k	-0.5320	0.6581
L_C	0.0533	0.6262
C_β	0.3515	0.6762
x	0.0099	0.5931
ε_α	-0.2384	1.0251

- the profile shift coefficient,

bear little influence on the value of α_k . On the other hand,

- the addendum factor;
- the tip alteration alteration factor;
- the crowing profile modification;
- the end relief profile modification;
- the contact ratio, possibly as a consequence of other factors,

do play a significant role in its value. From this separation, the follow up measure would be the establishment of a dimensionless parameter, including all the relevant geometrical parameters, of which α_k could be a function of. Later on, the parameters with lower influence could be included, with the exception of the module that evidently has little to no contribution on the matter. Since the profile modifications shift the value of α_k vertically, this function could include a parcel including, exclusively, the parameters that are responsible for the axial profile modifications. Fig. 5.16 shows the numerical results obtained and the curve obtained when replacing the average value of \mathcal{R} for all the numerical points in Eq. 2.87, which has a value of 0.3943. From the presented results, the values of α_k are slightly higher for the gears with corrections, which have lower contact ratios. This behavior contradicts that of the $\alpha_k = f(\varepsilon_\alpha)$ curve for those same values of ε_α . Increasing the contact ratio leads to lower values α_k , and lowering its value leads to higher values of α_k . However, for the same value of ε_α , there are several values of α_k , as seen in Fig. 5.17. This means that, against what is mostly stated in the literature, α_k cannot be a function of ε_α alone, making the previous comment concerning the inclusion of the most relevant geometrical parameters in the definition of α_k even more important. Fig. 5.17 also shows how the numerical results behave in comparison with the other curves proposed.

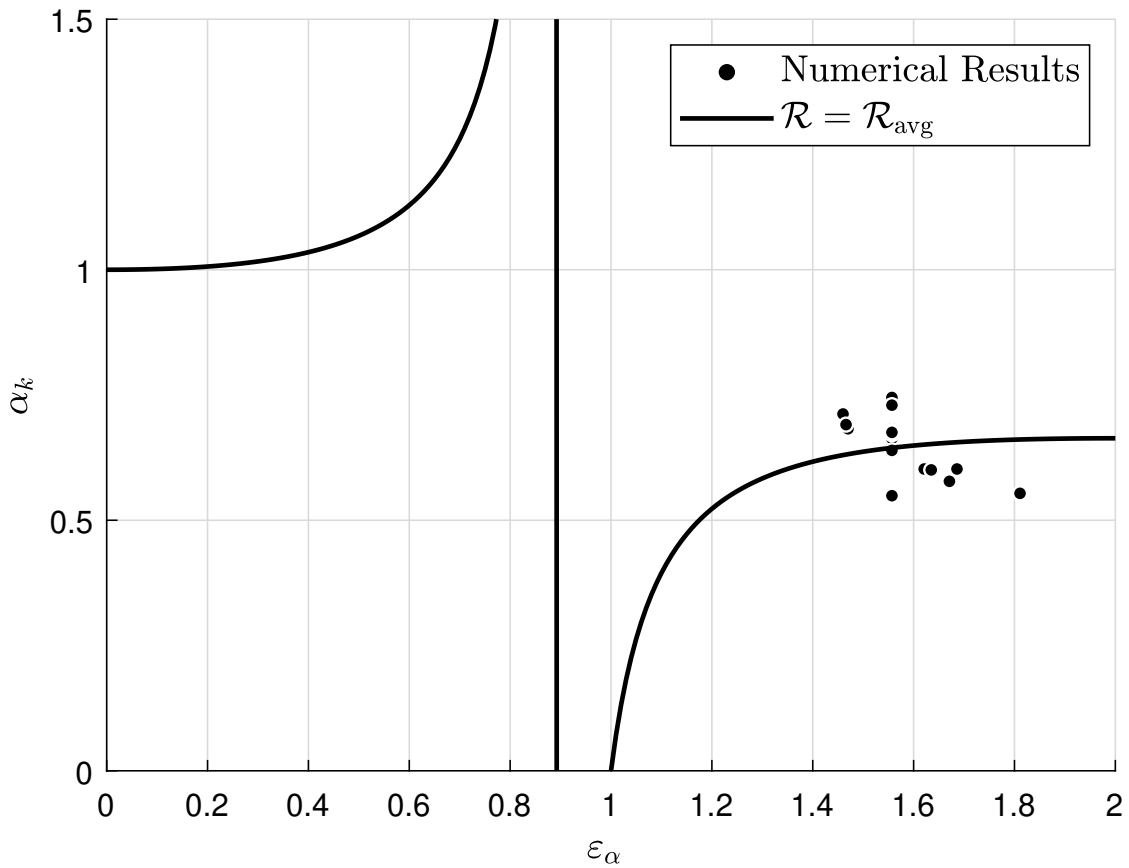


Figure 5.16 Variation of the α_k parameter with the contact ratio in terms of \mathcal{R} [13].

From these results, one can either establish which curves are more appropriate for each case or consider the proposed value of \mathcal{R} for implementations. Nonetheless, this is far from a final stage of the desired state of this work and the focus should remain on the proposed future works.

As an additional regard, the tip alteration modifies the height of the teeth, while keeping the remaining profile parameters the same. In practical terms, this means that the parabola should begin earlier or later and end earlier or later when compared to the parabola of the same tooth, with the same parameters, without the tip alteration. Clearly, this has an impact in α_k and, by varying it with a certain rule, should be something worthy of further investigation. The present results may be the starting point of such investigation, but more models with a wider variety of the discrete values of the geometrical parameter should be simulated for that matter.

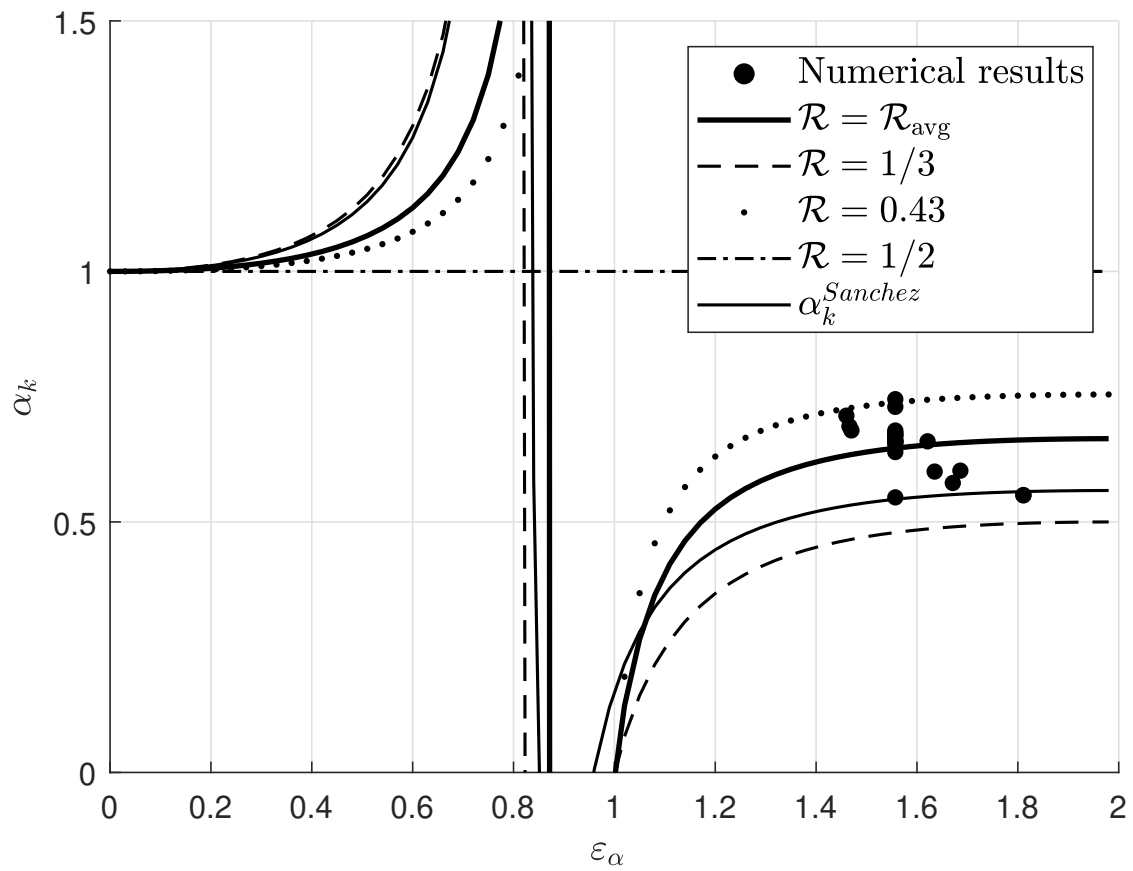


Figure 5.17 Different curves for the determination of α_k [13].

Chapter 6

Conclusions and Future Works

In this final chapter, some conclusions about the obtained results are presented to summarize the information that this work provided. Based on these conclusions, some future works are proposed to enrich the work done here and culminate some results that have no apparent/conclusive cause.

6.1 Main Conclusions

With this work, several conclusions can be reached. First, α_k must be a function of parameters other than ε_α . On that note the addendum factor, the tip alteration factor, the crowing profile modification, the end relief profile modification and the contact ratio have significant influence on the α_k value. The module, the root radius factor, the gear ratio, the dedendum factor and the profile shift coefficient (on the gear, having the biggest variation amplitude) have little to no influence on the α_k value.

It can also be concluded that profile modifications in the axial direction have great influence on both the value of α_k and the shape of the gear mesh stiffness distribution.

It can be hypothesized that tip alteration can be condensed in a personalized starting and ending point of the unaltered gear mesh stiffness curve. However, further work would need to be done to reach tangible conclusions on the definitive influences of the parameter on the mesh stiffness curve and verify if such a rule can be established.

6.2 Future Work

The step that necessarily follows this work is establishing a law of variation of α_k that includes every parameter of relevant influence. Describing the parameter as a function of a dimensionless value comprised by those influential parameters would be an ideal scenario. That way, the limitation of the multiple values of α_k for the same value of ε_α would no longer exist and effects not taken into account until now would be considered. It is

expected that such improvement would allow the model to acquire a wider coverage of cases with smaller approximation errors.

The comparison of the obtained values with the ISO 6336-1 Method B would also provide an insight of the accuracy of the developed model while allowing to estimate how the estimations deviate from one another, while reaching conclusions from that analysis.

As a necessary follow-up, implementing the improved model and comparing it to existing results would be an indicator of whether steps back should be taken or if moving forward is possible.

Even though the range of contact ratios includes the vast majority of applications regarding this value alone (most gears considered here could not be used in real life applications), extending this range would lead to a more elegant and complete definition of the model, which should also be a goal worth consideration.

Extending this analysis to helical gears is of the utmost importance, given the wide variety of applications that benefit from this technology.

The current FEM models contain information regarding the load distribution along the width; however, accessing and handling this information requires significantly more time than the information handled throughout this work. As such, analyzing that already existing information would enrich the work at hands and the approximated analytical model presented, which handles that problem. In addition to that, recent literature stated that the equivalent cylinders approach is not the most appropriate to deal with load sharing problems in spur gears contact. It would be interesting to implement a static model comprised of two cylinders, the equivalent cylinders, and compare the results obtained with the full geometry and the simplification to reach some verification.

References

- [1] S N Doğan, J Ryborz, and B Bertsche. Design of low-noise manual automotive transmissions. *Proceedings of the Institution of Mechanical Engineers, Part K: Journal of Multi-body Dynamics*, 220(2):79–95, 2006.
- [2] Pedro Marques, Ramiro Martins, and Jorge Seabra. Analytical load sharing and mesh stiffness model for spur/helical and internal/external gears – towards constant mesh stiffness gear design. *Mechanism and Machine Theory*, 113:126–140, 2017.
- [3] Süreyya Nejat Dogan, J Ryborz, and B Bertsche. Design of low-noise manual automotive transmissions. *Proceedings of The Institution of Mechanical Engineers Part K-journal of Multi-body Dynamics - PROC INST MECH ENG K-J MUL D*, 220:79–95, 06 2006.
- [4] Marcello Faggioni, Farhad S. Samani, Gabriele Bertacchi, and Francesco Pellicano. Dynamic optimization of spur gears. *Mechanism and Machine Theory*, 46(4):544–557, 2011.
- [5] H. Nevzat Özgüven and D. R. Houser. Dynamic analysis of high speed gears by using loaded static transmission error. *Journal of Sound Vibration*, 125(1):71–83, August 1988.
- [6] M. S. Tavakoli and D. R. Houser. Optimum Profile Modifications for the Minimization of Static Transmission Errors of Spur Gears. *Journal of Mechanisms, Transmissions, and Automation in Design*, 108(1):86–94, 03 1986.
- [7] João Marafona, Pedro Marques, Ramiro Martins, and Jorge Seabra. Towards constant mesh stiffness helical gears: The influence of integer overlap ratios. *Mechanism and Machine Theory*, 136:141–161, 06 2019.
- [8] Vincenzo Vullo. *Gears: Volume 3: A Concise History*. 01 2020.
- [9] João D.M. Marafona, Pedro M.T. Marques, Ramiro C. Martins, and Jorge H.O. Seabra. Mesh stiffness models for cylindrical gears: A detailed review. *Mechanism and Machine Theory*, 166:104472, 2021.
- [10] Xiuquan Sun, Tie Wang, Ruiliang Zhang, Fengshou Gu, and Andrew D. Ball. A Model for Mesh Stiffness Evaluation of Spur Gear with Tooth Surface Wear. In *Surveillance, Vishno and AVE conferences*, Lyon, France, July 2019. INSA-Lyon, Université de Lyon.
- [11] Miryam B. Sánchez, Miguel Pleguezuelos, and José I. Pedrero. Approximate equations for the meshing stiffness and the load sharing ratio of spur gears including hertzian effects. *Mechanism and Machine Theory*, 109:231–249, 2017.

-
- [12] ISO 6336-1. *Calculation of load capacity of spur and helical gears*. 2006.
- [13] Pedro M.T. Marques, João D.M. Marafona, Ramiro C. Martins, and Jorge H.O. Seabra. A continuous analytical solution for the load sharing and friction torque of involute spur and helical gears considering a non-uniform line stiffness and line load. *Mechanism and Machine Theory*, 161:104320, 2021.
- [14] Christopher G. Cooley, Chunguang Liu, Xiang Dai, and Robert G. Parker. Gear tooth mesh stiffness: A comparison of calculation approaches. *Mechanism and Machine Theory*, 105:540–553, 2016.
- [15] Mengjiao Feng, Hui Ma, Zhanwei Li, Qibin Wang, and Bangchun Wen. An improved analytical method for calculating time-varying mesh stiffness of helical gears. *Meccanica*, 53(4):1131–1145, Mar 2018.
- [16] Rama Thirumurugan and N. Gnanasekar. Influence of finite element model, load-sharing and load distribution on crack propagation path in spur gear drive. *Engineering Failure Analysis*, 110:104383, 2020.
- [17] Jiaxing Zhan, Mohammad Fard, and Reza Jazar. A cad-fem-qa integration technique for determining the time-varying meshing stiffness of gear pairs. *Measurement*, 100:139–149, 2017.
- [18] Kangkang Chen, Yifan Huangfu, Hui Ma, Zhitao Xu, Xu Li, and Bangchun Wen. Calculation of mesh stiffness of spur gears considering complex foundation types and crack propagation paths. *Mechanical Systems and Signal Processing*, 130:273–292, 2019.
- [19] Fatih Karpat, Celalettin Yuce, and Oğuz Doğan. Experimental measurement and numerical validation of single tooth stiffness for involute spur gears. *Measurement*, 150:107043, 2020.
- [20] J. Coy and C. H. Chao. A method of selecting grid size to account for hertz deformation in finite element analysis of spur gears. *Journal of Mechanical Design*, 104:759–764, 1982.
- [21] SDPSI. *Elements of Metric Gear Technology*. 2006.
- [22] KISSsoft. *KISSsoft Release 2020 User Manual*. 2020.
- [23] Yongyi Zhu. *Best Practices for Contact Modeling using ANSYS*. 2017.
- [24] ANSYS. *ANSYS Contact Technology Guide*. 2004.
- [25] Steven Owen, Scott Canann, and Sunil Saigal. Pyramid elements for maintaining tetrahedra to hexahedra conformability. *Trends In Unstructured Mesh Generation*, 220, 01 1997.
- [26] ANSYS. *ANSYS Meshing User’s Guide*. 2010.
- [27] Gerd Kunert and Serge Nicaise. Zienkiewicz-zhu error estimators on anisotropic tetrahedral and triangular finite element meshes. *M2AN. Mathematical Modelling and Numerical Analysis. ESAIM, European Series in Applied and Industrial Mathematics*, 37, 11 2003.

-
- [28] W. Yu and C. K. Mechefske. A new model for the single mesh stiffness calculation of helical gears using the slicing principle. *Iranian Journal of Science and Technology, Transactions of Mechanical Engineering*, 43(1):503–515, Jul 2019.
- [29] ANSYS. *Theory Reference for the Mechanical APDL and Mechanical Applications*. 2009.

This page was intentionally left blank.

Appendices

Appendix A

Zienkiewicz-Zhu estimator

The Zienkiewicz-Zhu (ZZ) estimator is a popular estimator that compares a recovered gradient with the original gradient to compute the error. It computes the improvement of the gradient of the numerical solution through post-processing procedures [27, 29]. Although its applications were limited to isotropic meshes, recent studies have been aiming to widen the window of applicability, extending the ZZ to anisotropic meshes, which have a much less developed error estimation theory. The ZZ estimator's popularity is not for naught:

- the ZZ estimator is relatively cheap, since it uses a recovered gradient which is often computed even when it is not used
- the ZZ estimator, in numerical experiments, is extremely robust, which explains the variety of problems that can profit from this error estimation approach

The Displacement-Based finite element formulation assumes continuity that results in a continuous displacement field from element to element. However, this property is not kept for the stress field, which ends up discontinuous. Obtaining acceptable stresses becomes one extra task, involving the calculation of the elements' nodal stresses average and then returning to a single element's domain. Doing this for every element of the model makes it possible to infer on convergence/quality of the simulation. For context, the formulation on which the error calculation algorithm is based will be briefly presented. First, the stresses at each node of the element are used to compute

$$\{\Delta\sigma_n^i\} = \{\sigma_n^a\} - \{\sigma_n^i\} \quad (\text{A.1})$$

where:

$\{\Delta\sigma_n^i\}$ = stress error vector at node n of the element i;

$\{\sigma_n^a\}$ = averaged stress vector at node n, calculated as stated in Eq. A.2;

$\{\sigma_n^i\}$ = stress vector of node n of the element i.

$$\{\sigma_n^a\} = \frac{\sum_{i=1}^{N_e^n} \{\sigma_n^i\}}{N_e^n} \quad (\text{A.2})$$

Once obtained, the stress error vector is used to determine, for each element,

$$e_i = \frac{1}{2} \int_{Vol} \{\Delta\sigma\}^T [D]^{-1} \{\Delta\sigma\} d(Vol) \quad (\text{A.3})$$

where:

e_i = energy error for the element i ;

Vol = Volume of the element;

$[D]$ = stress-strain/constitutive matrix evaluated at reference temperature;

$\{\Delta\sigma\}$ = stress error vector at the relevant and needed points, evaluated from all the stress vectors, $\{\sigma_n\}$, of the element.

Then, over the whole model, the error is given by

$$e = \sum_{i=1}^{N_r} e_i \quad (\text{A.4})$$

where:

e = energy error over the entire model;

N_r = number of elements in the model.

The program also allows the error to be normalized in terms of the strain energy and the energy error for a single element can be used for adaptive mesh refinement to achieve "error equilibration", a concept that describes a situation where e_i is equal for all elements.

Appendix B

Transmission Error and Mesh Stiffness Curves

In this appendix, the curves with the distribution of the transmission error, mesh stiffness and normalized mesh stiffness for every simulated model are shown in order to provide some complementary information concerning the results presented.

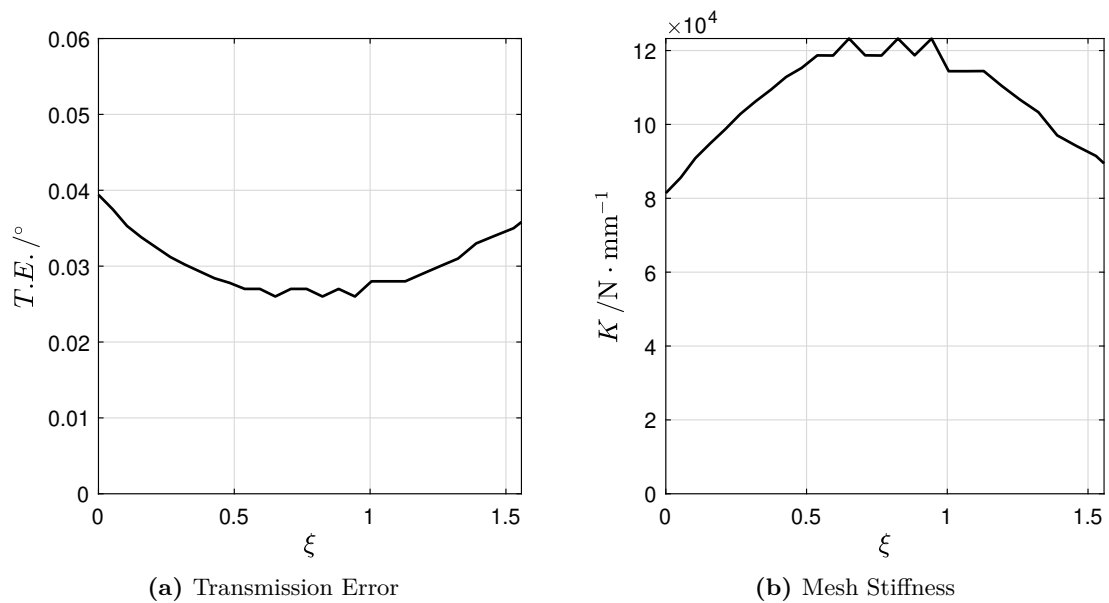


Figure B.1 Numerical results of the M1_75 model.

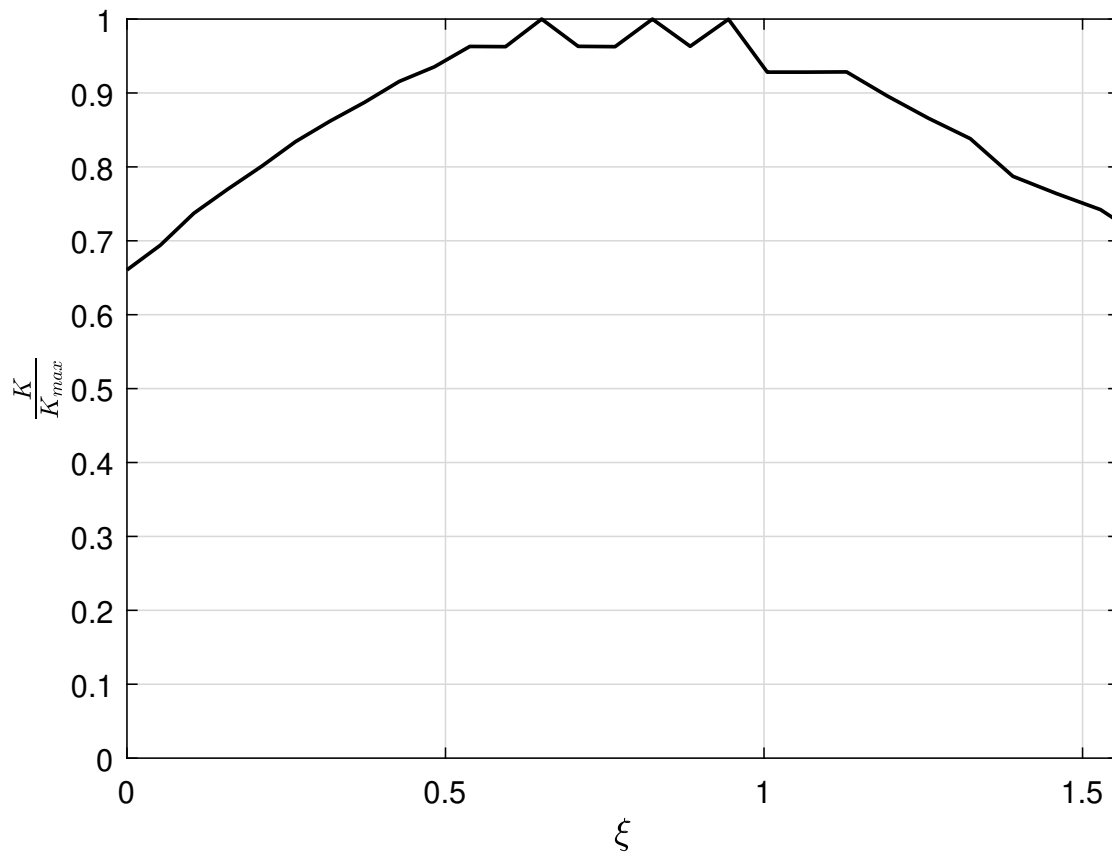


Figure B.2 Normalized mesh stiffness of the M1_75 model.

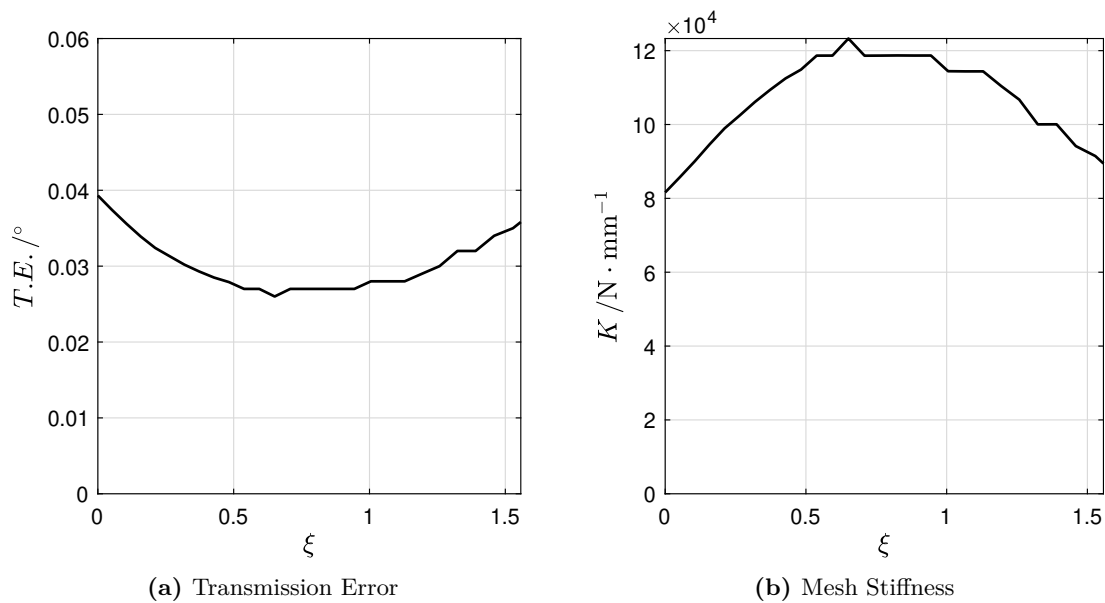


Figure B.3 Numerical results of the M2_5 model.

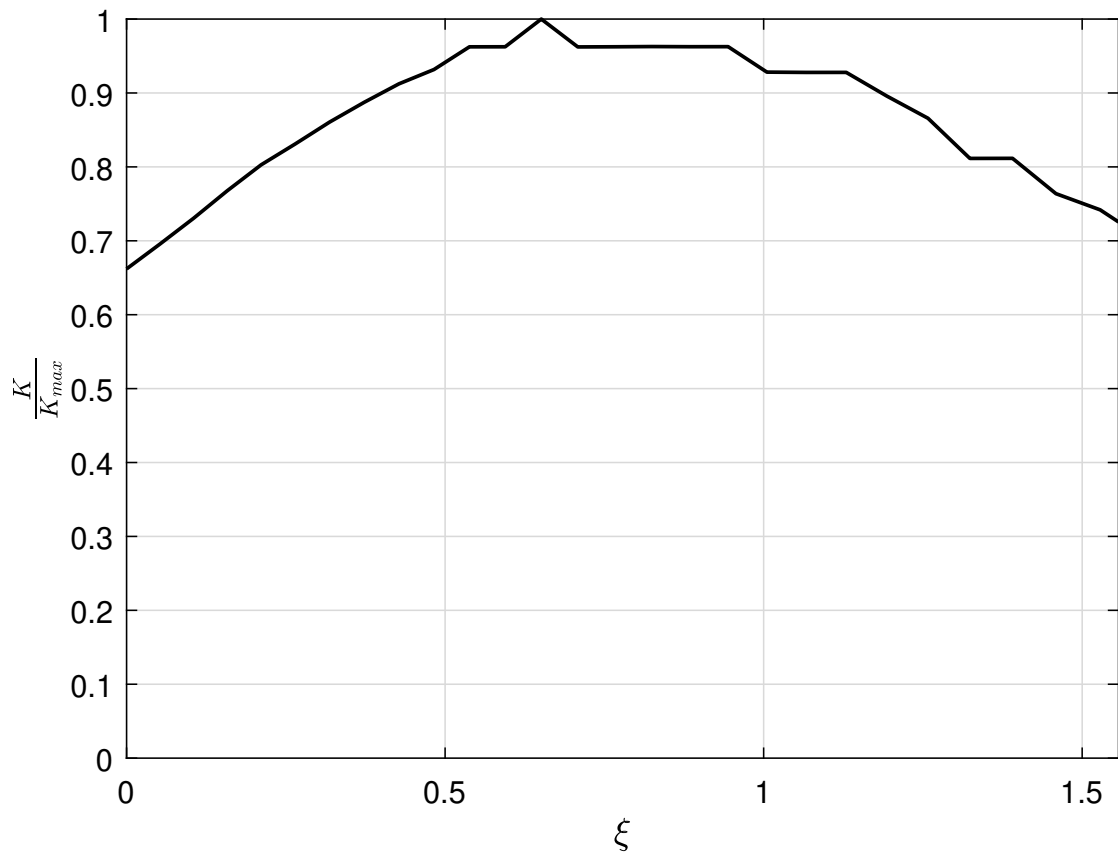
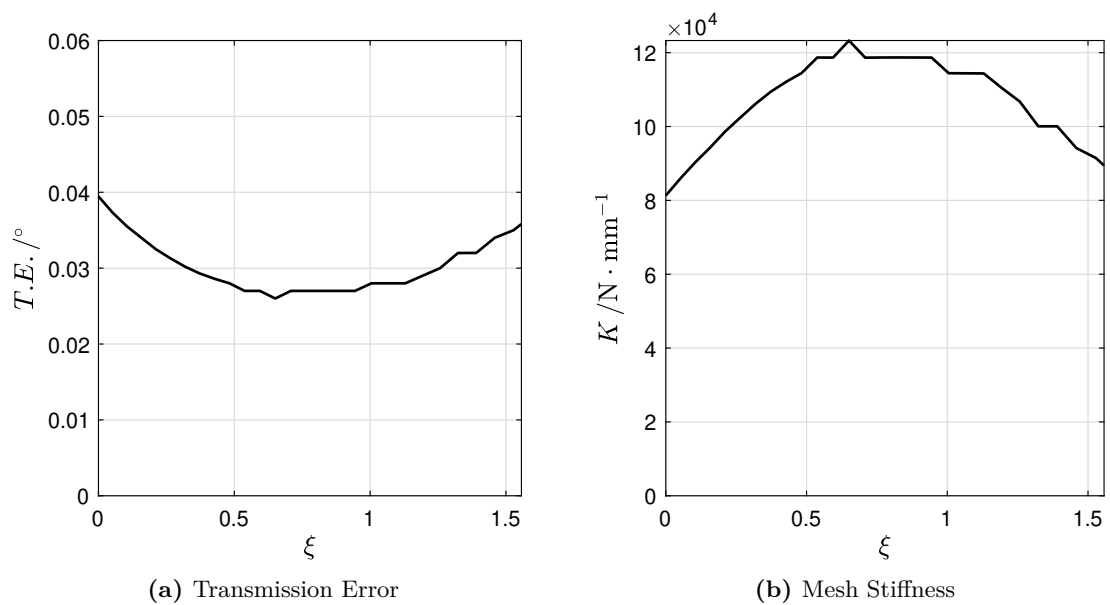


Figure B.4 Normalized mesh stiffness of the M2_5 model.



(a) Transmission Error

(b) Mesh Stiffness

Figure B.5 Numerical results of the M4_5 model.

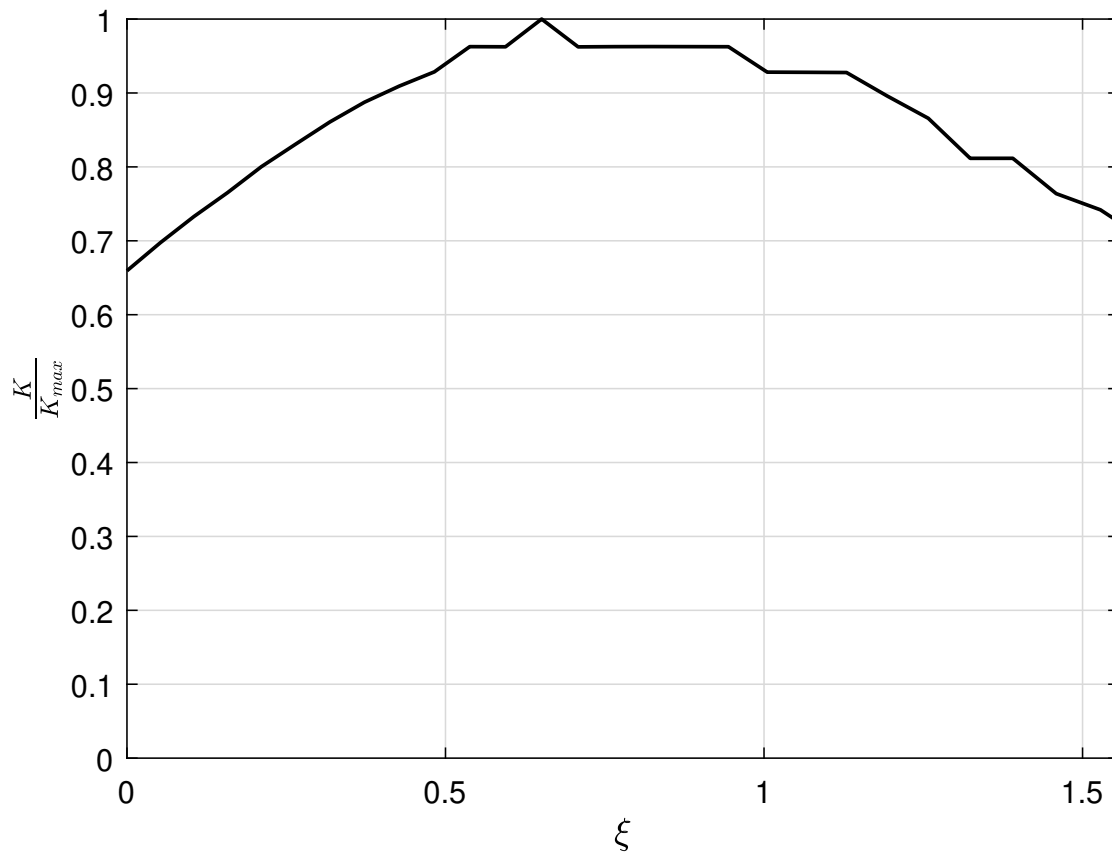


Figure B.6 Normalized mesh stiffness of the M4_5 model.

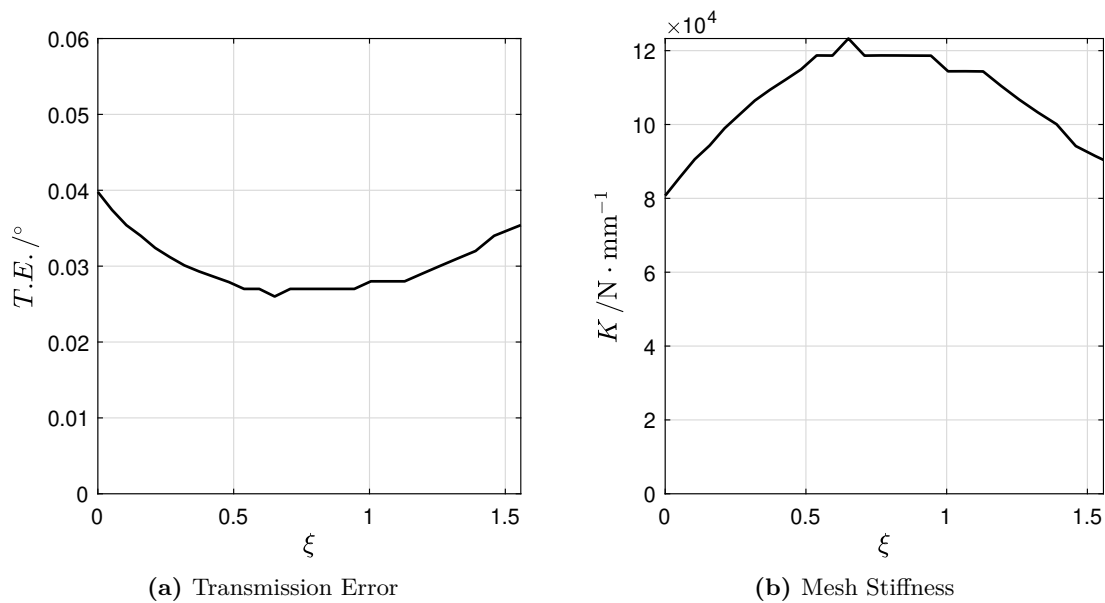


Figure B.7 Numerical results of the M8 model.

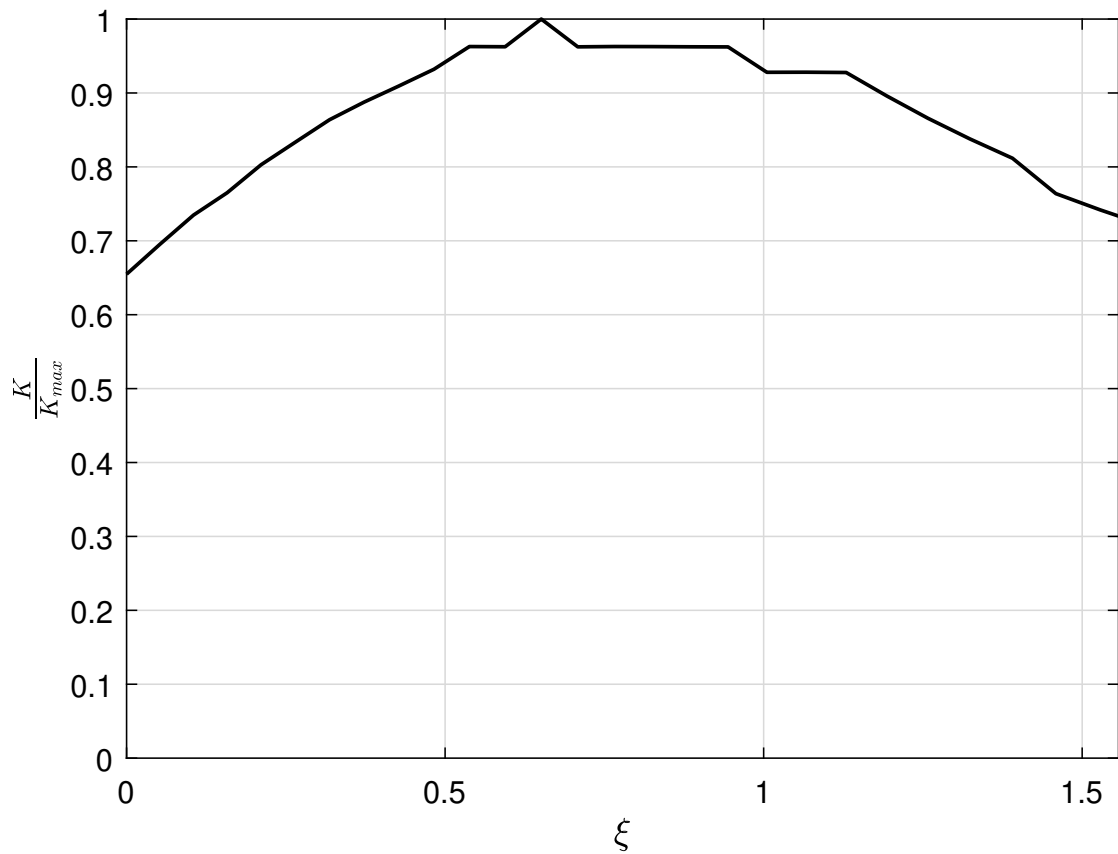
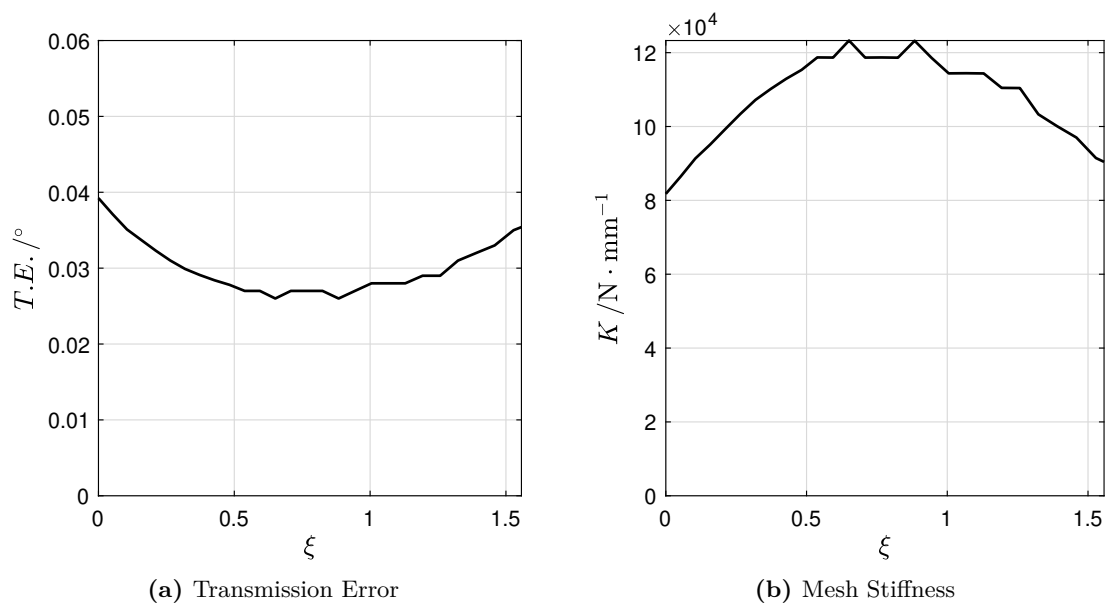


Figure B.8 Normalized mesh stiffness of the M8 model.



(a) Transmission Error

(b) Mesh Stiffness

Figure B.9 Numerical results of the M12 model.

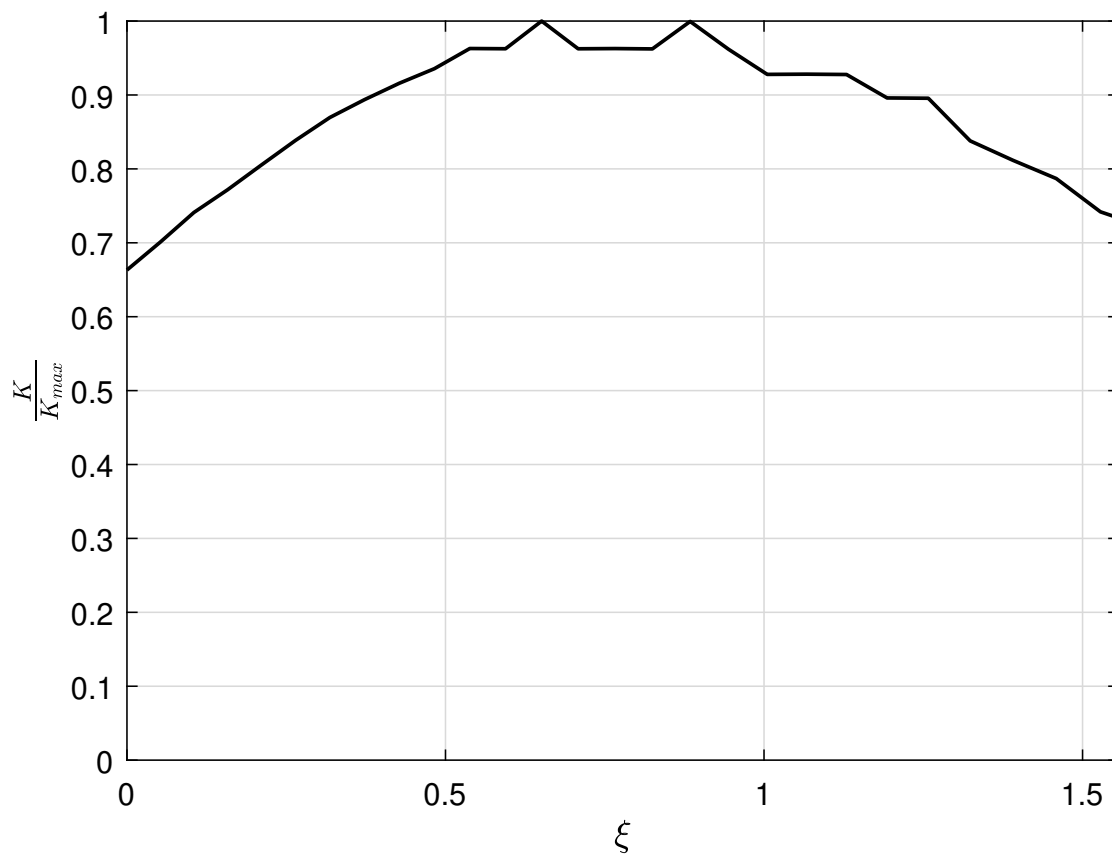


Figure B.10 Normalized mesh stiffness of the M12 model.

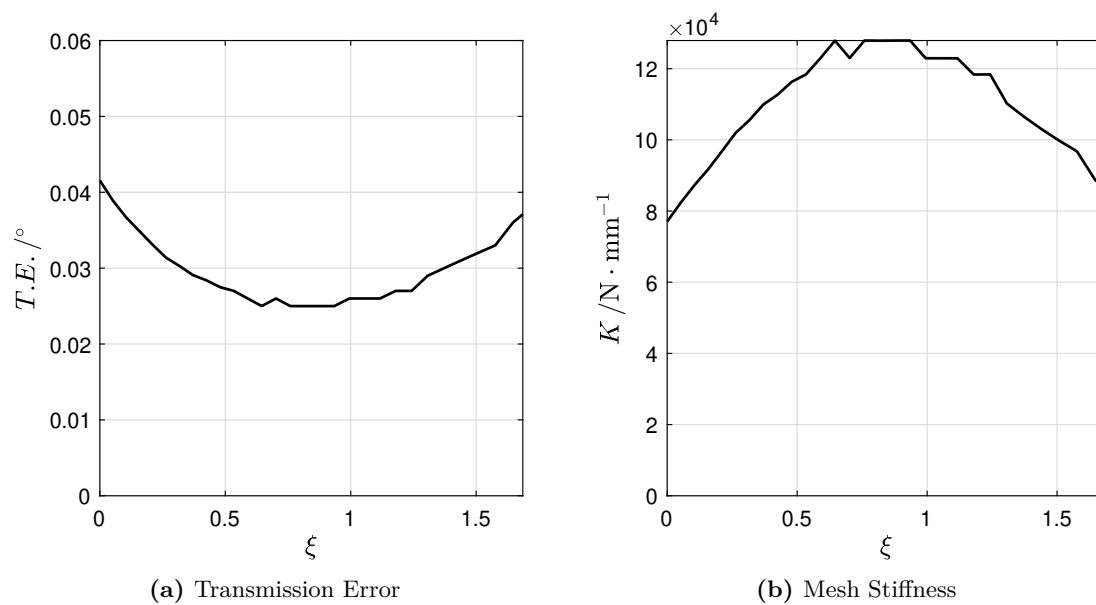


Figure B.11 Numerical results of the PROF111 model.

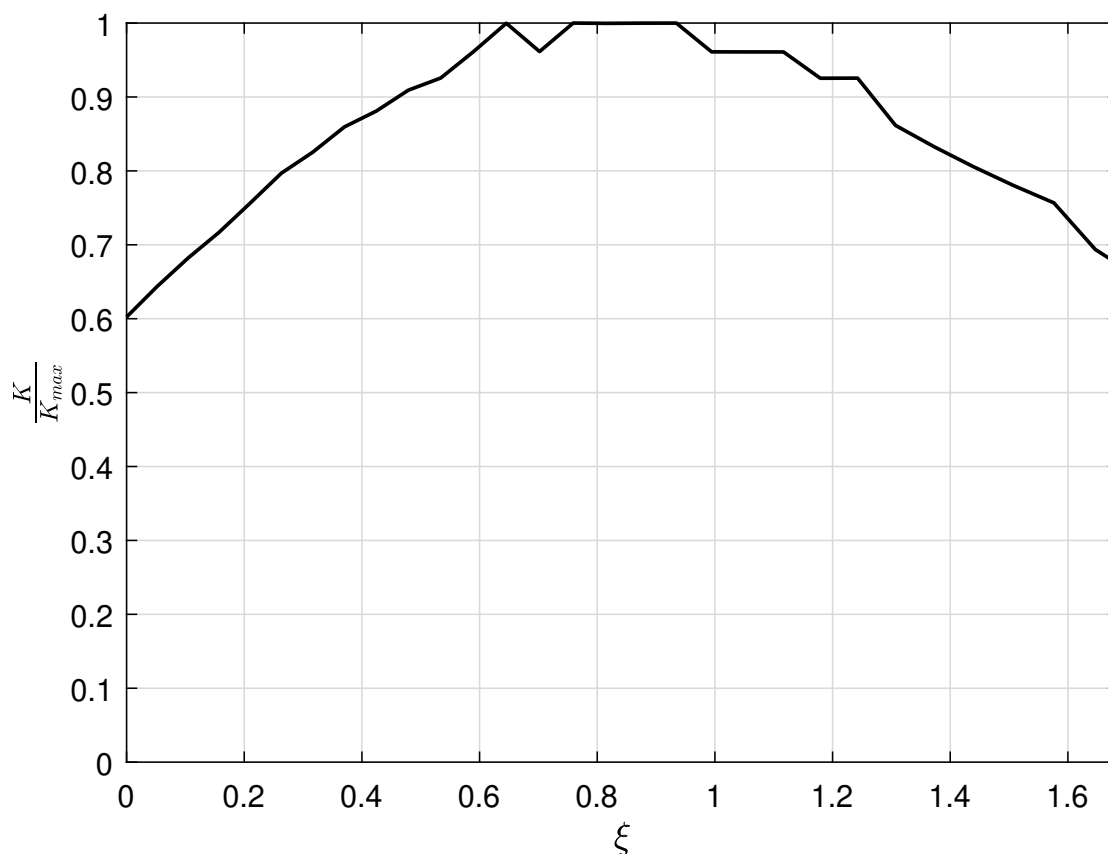
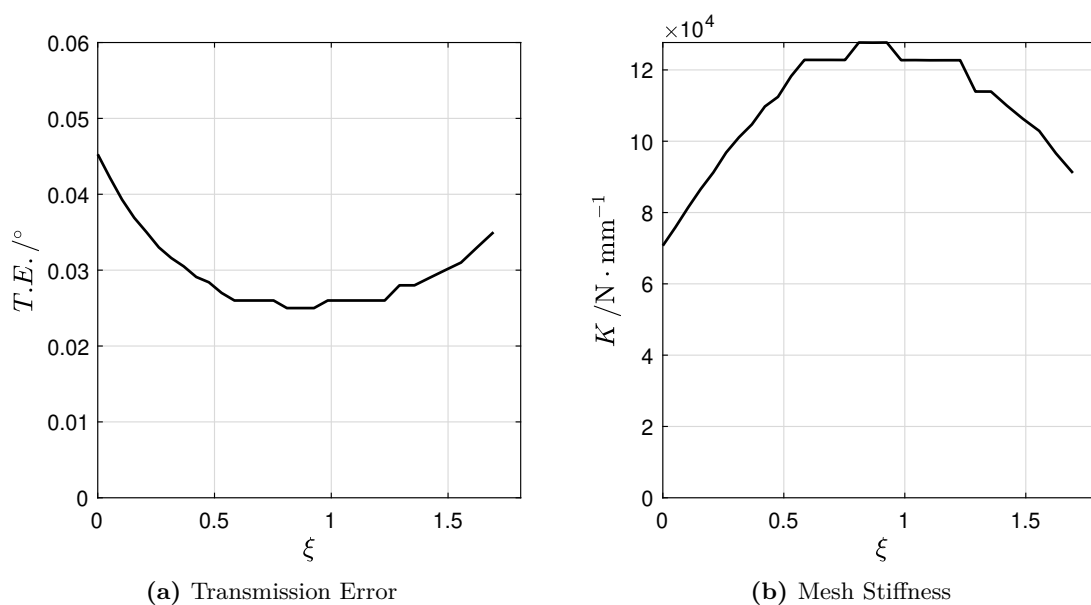


Figure B.12 Normalized mesh stiffness of the PROF11 model.



(a) Transmission Error

(b) Mesh Stiffness

Figure B.13 Numerical results of the PROF12 model.

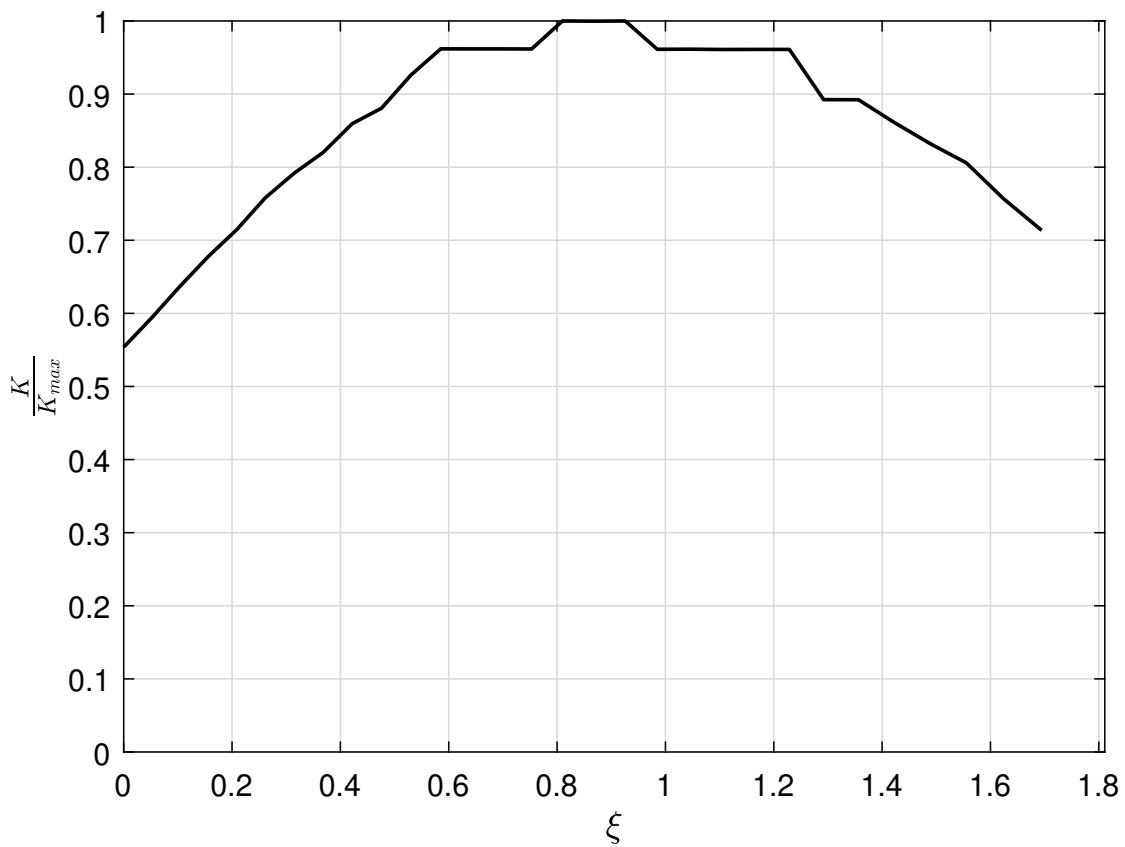


Figure B.14 Normalized mesh stiffness of the PROF12 model.

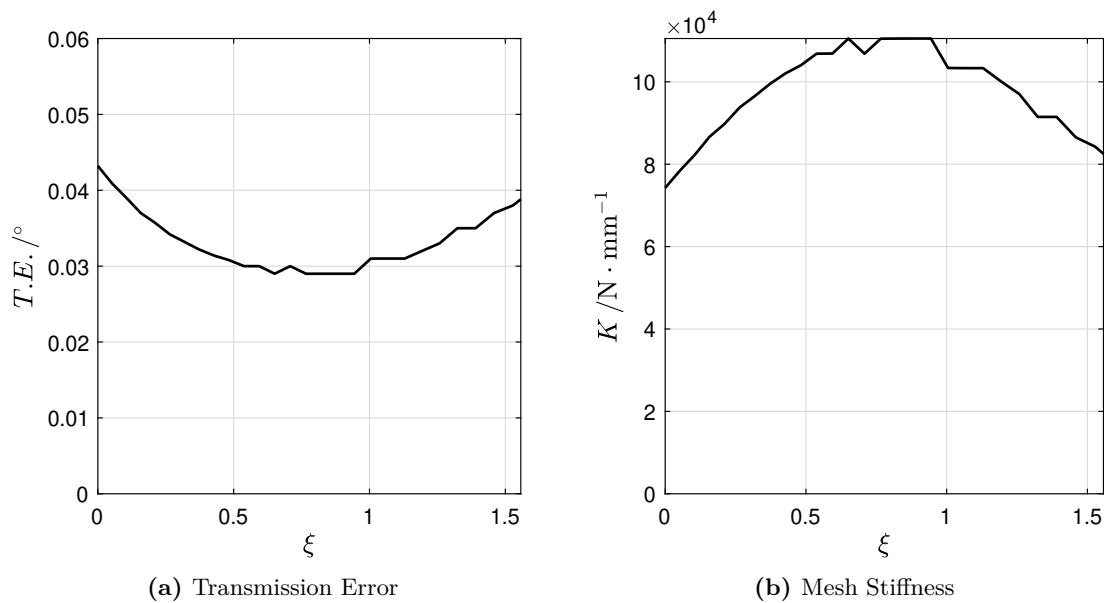


Figure B.15 Numerical results of the PROF121 model.

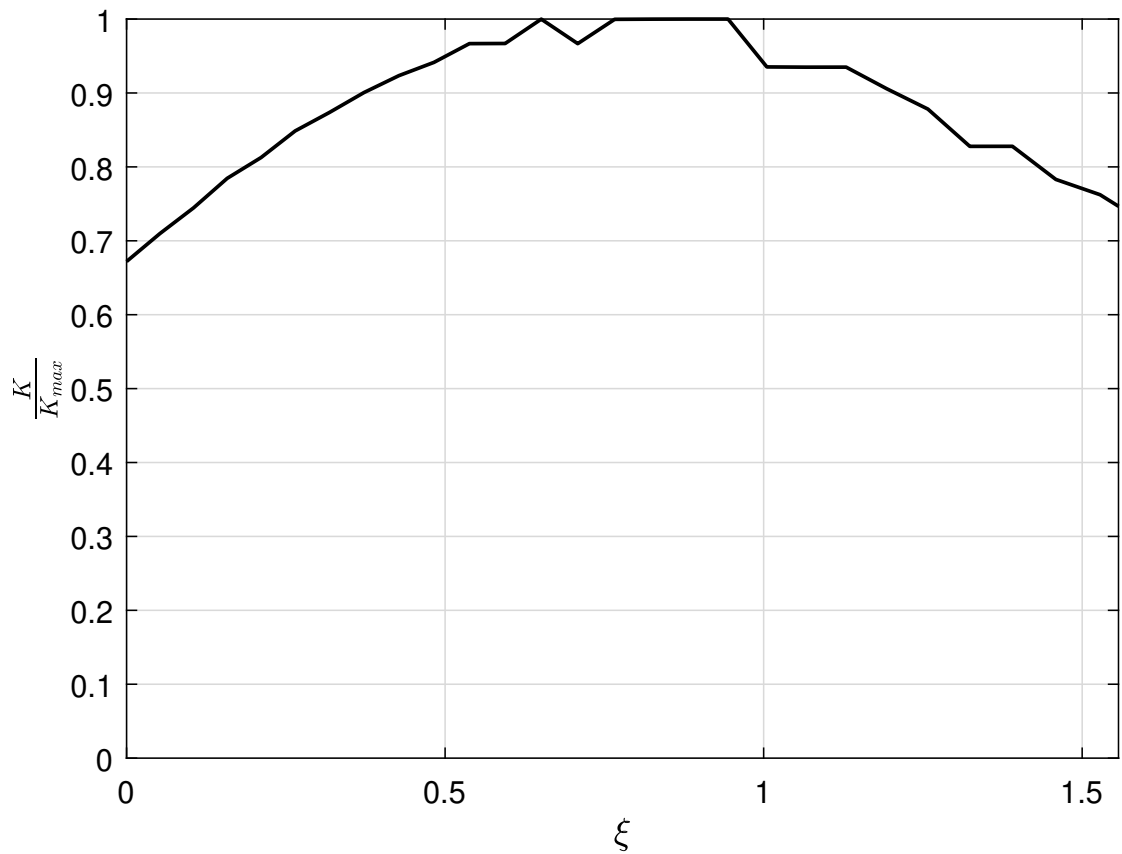
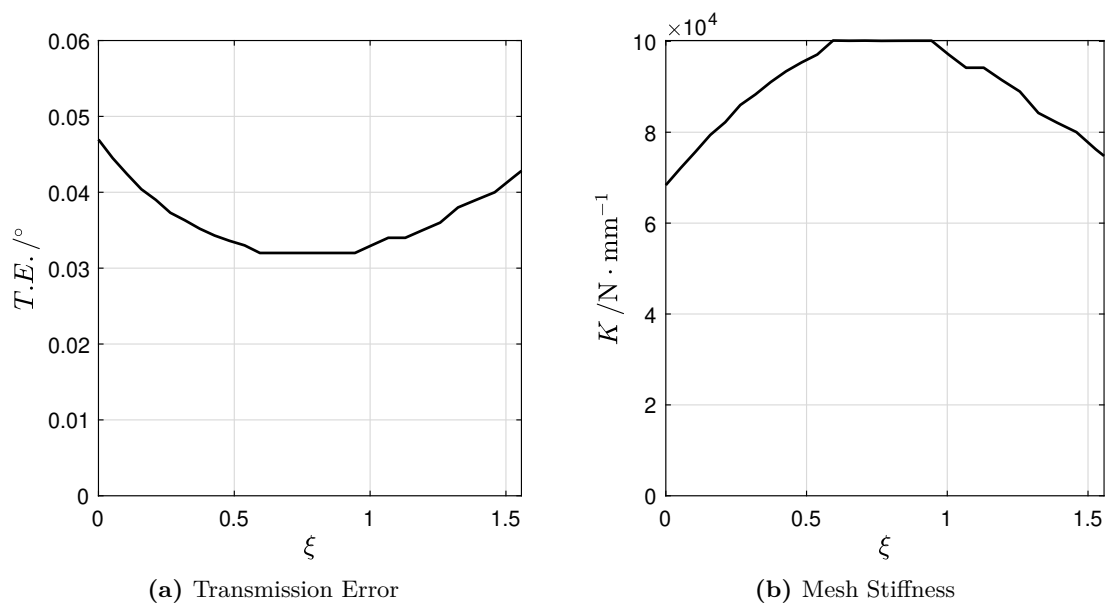


Figure B.16 Normalized mesh stiffness of the PROFI21 model.



(a) Transmission Error

(b) Mesh Stiffness

Figure B.17 Numerical results of the PROFI22 model.

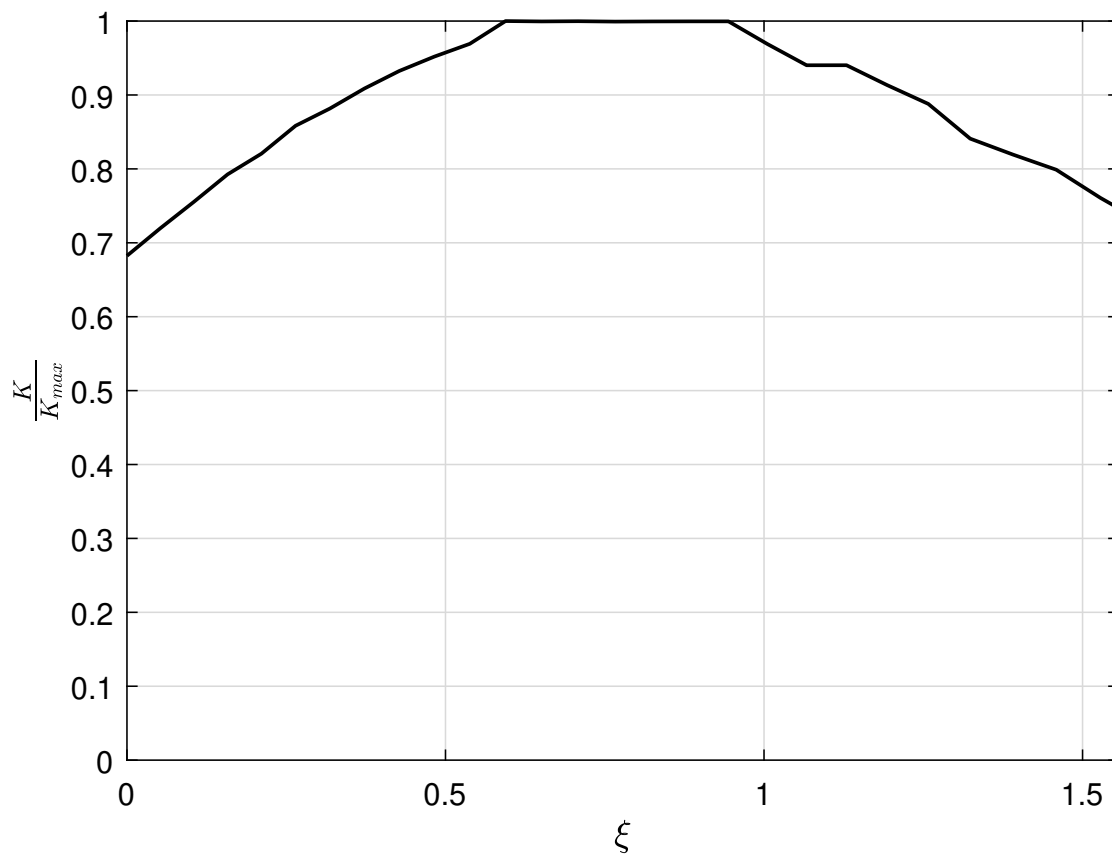


Figure B.18 Normalized mesh stiffness of the PROFI22 model.

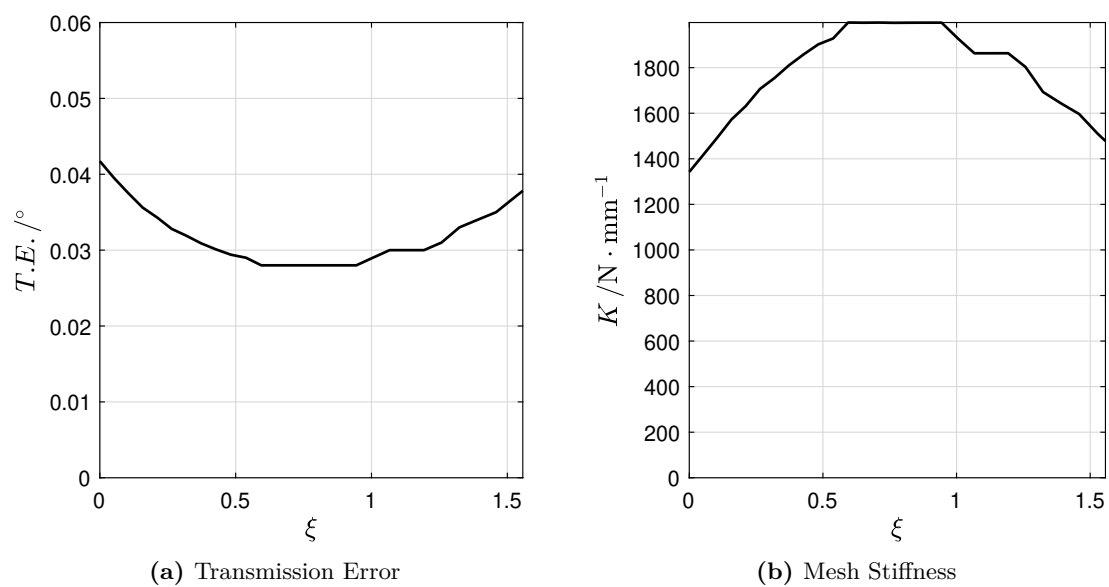


Figure B.19 Numerical results of the PROFI31 model.

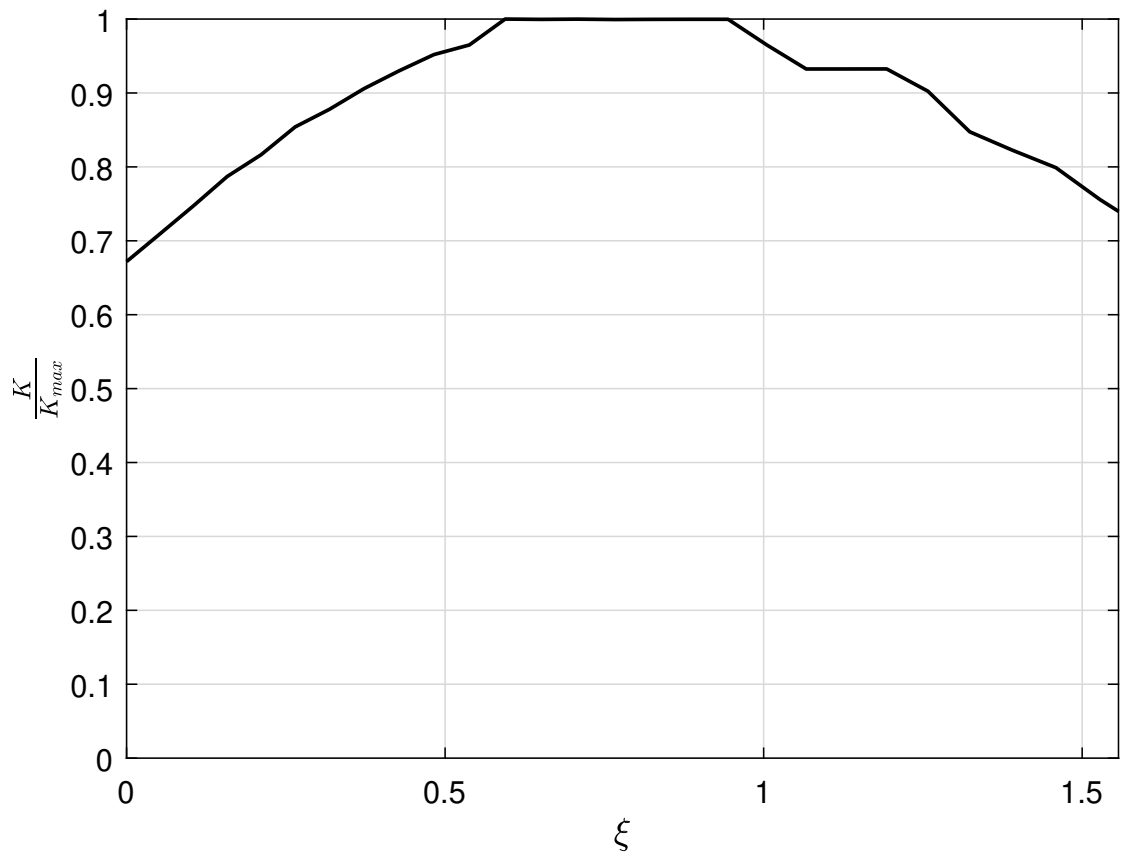
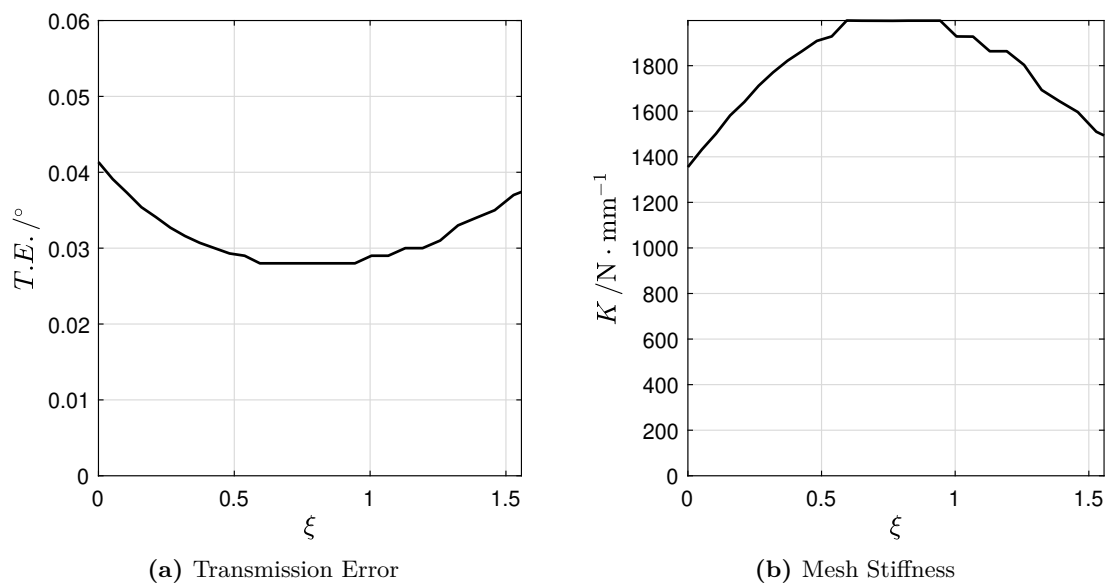


Figure B.20 Normalized mesh stiffness of the PROFI31 model.



(a) Transmission Error

(b) Mesh Stiffness

Figure B.21 Numerical results of the PROFI32 model.

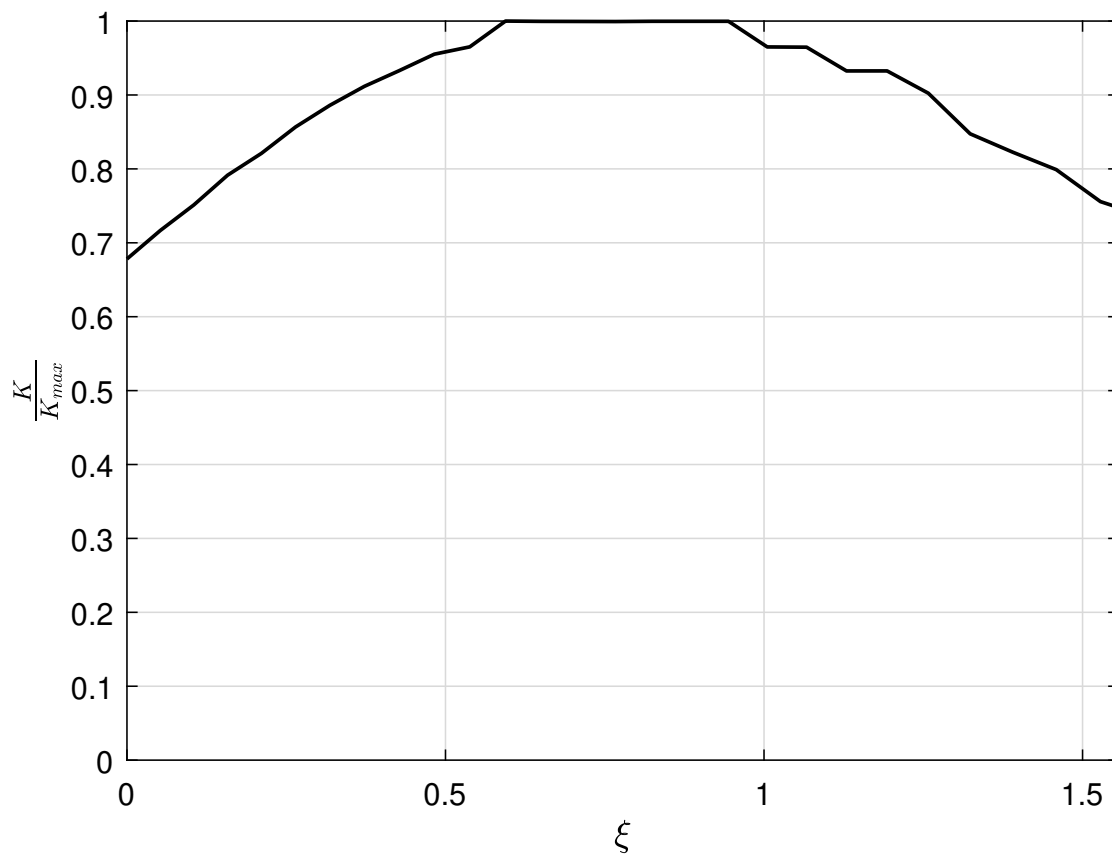
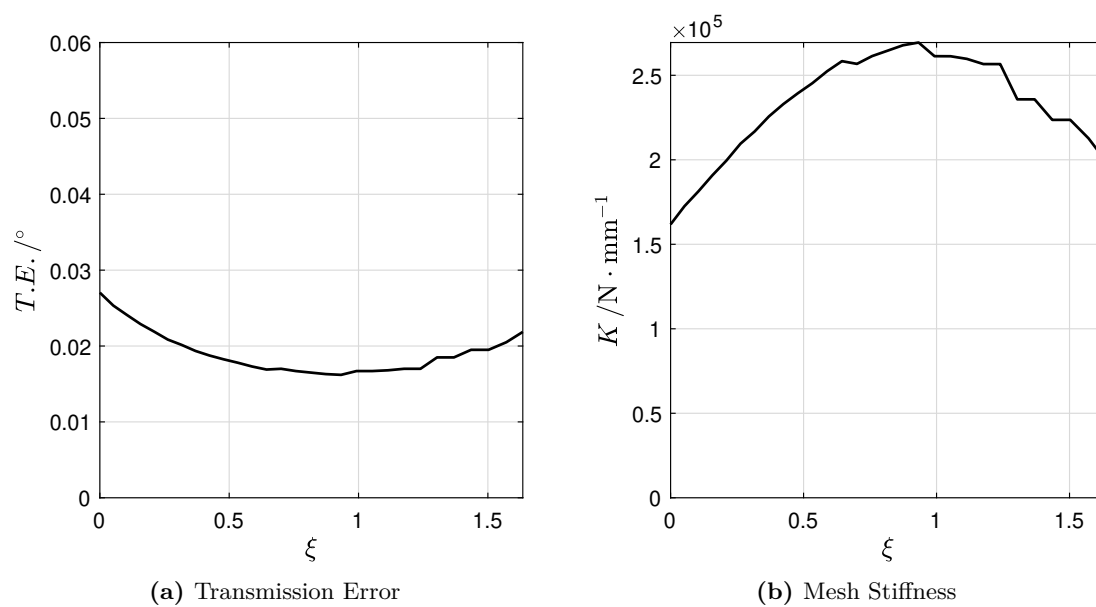


Figure B.22 Normalized mesh stiffness of the PROFI32 model.



(a) Transmission Error

(b) Mesh Stiffness

Figure B.23 Numerical results of the I2 model.

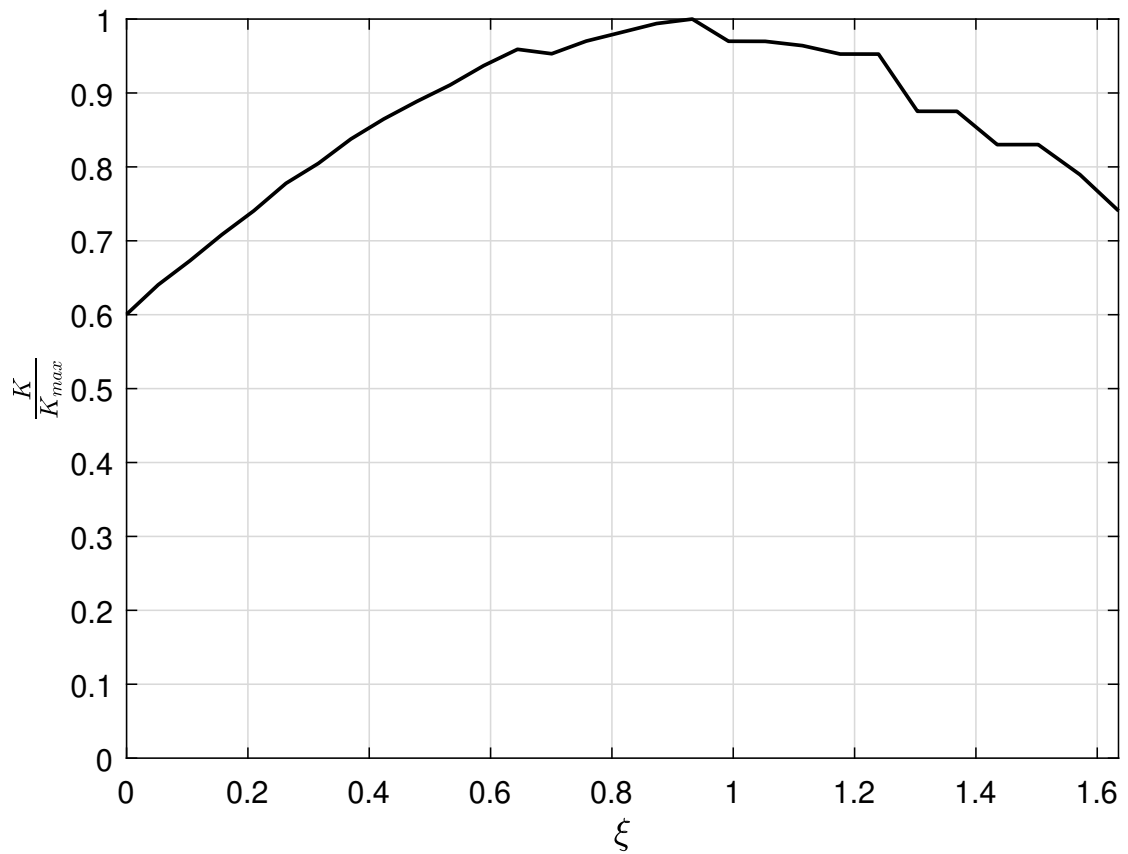
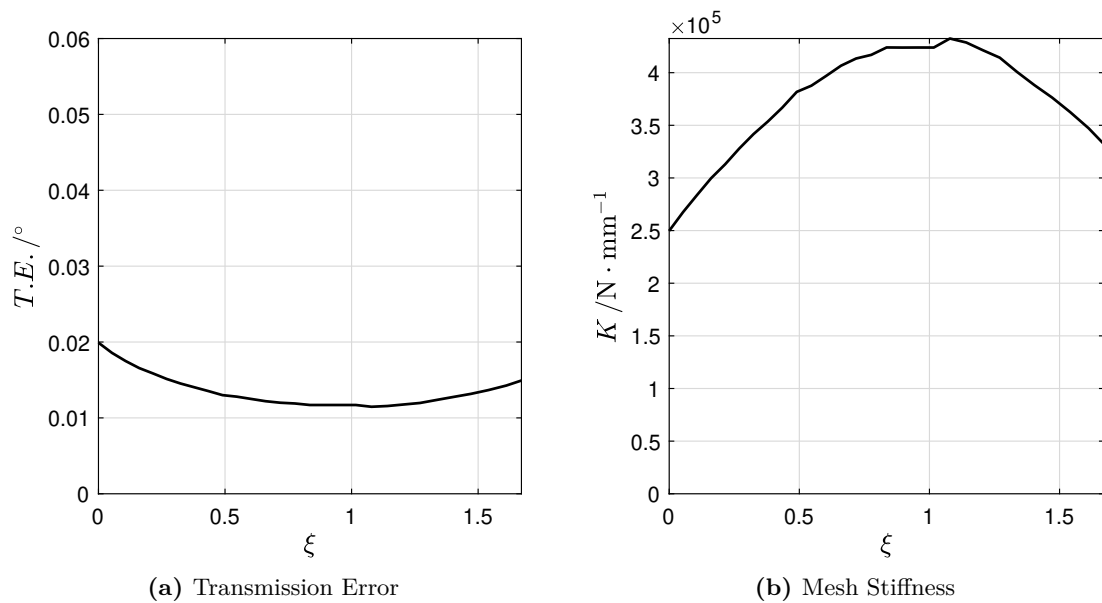


Figure B.24 Normalized mesh stiffness of the I2 model.



(a) Transmission Error

(b) Mesh Stiffness

Figure B.25 Numerical results of the I3 model.

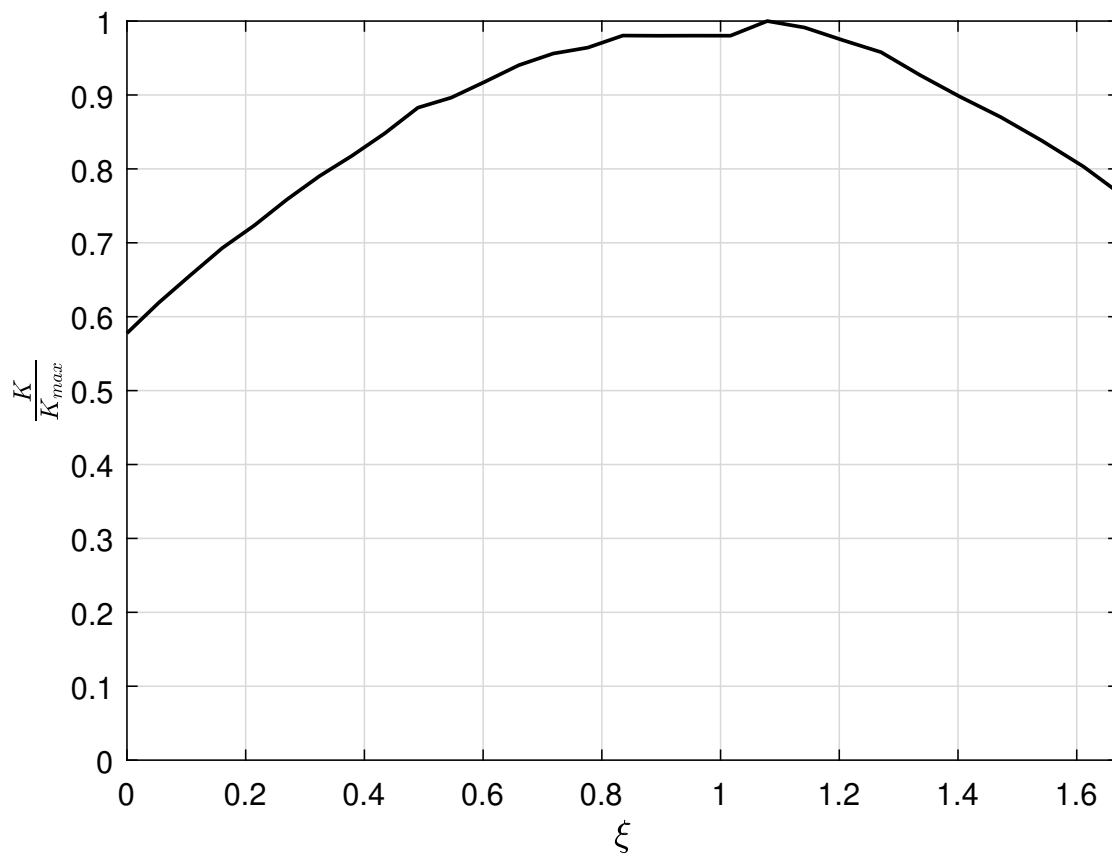
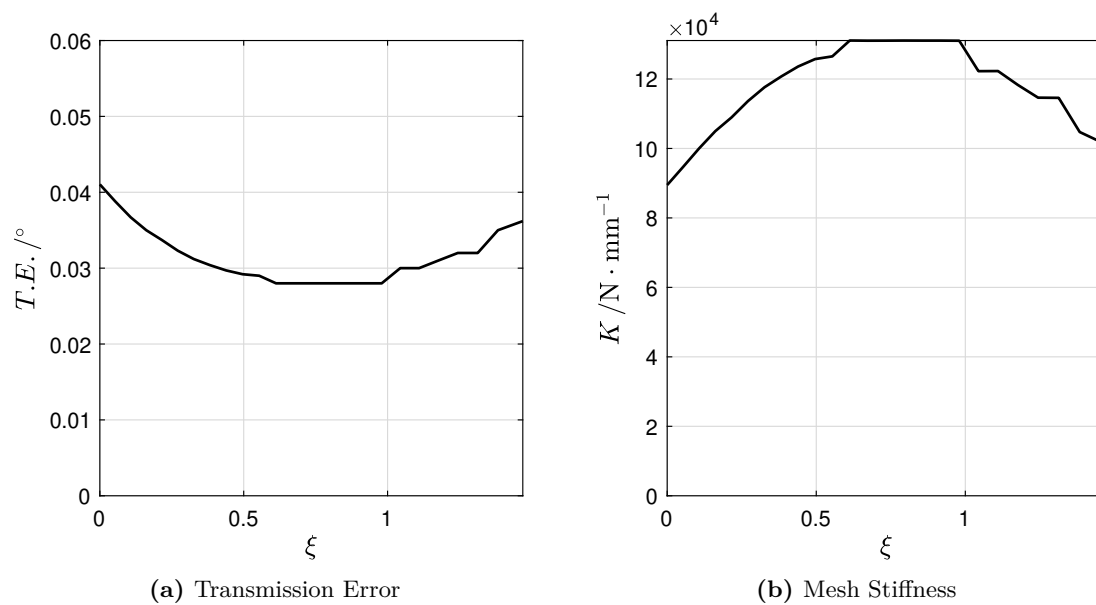


Figure B.26 Normalized mesh stiffness of the I3 model.



(a) Transmission Error

(b) Mesh Stiffness

Figure B.27 Numerical results of the C20 model.

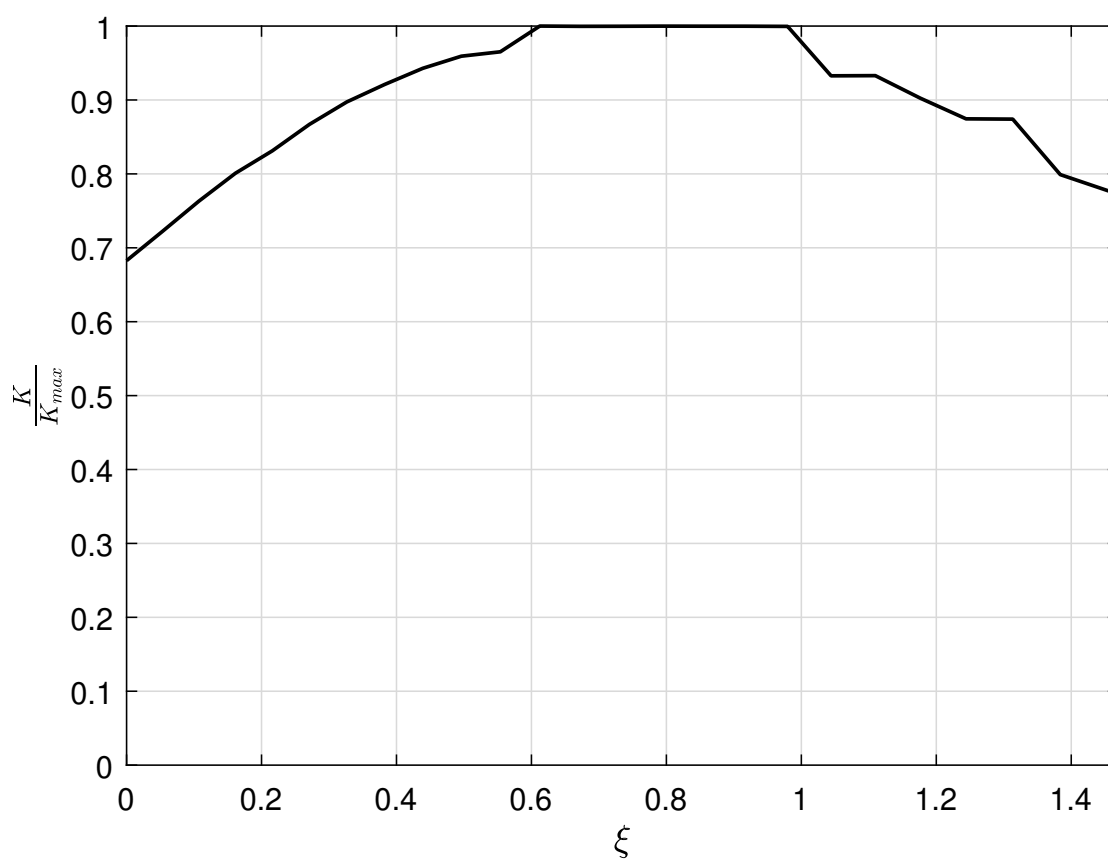
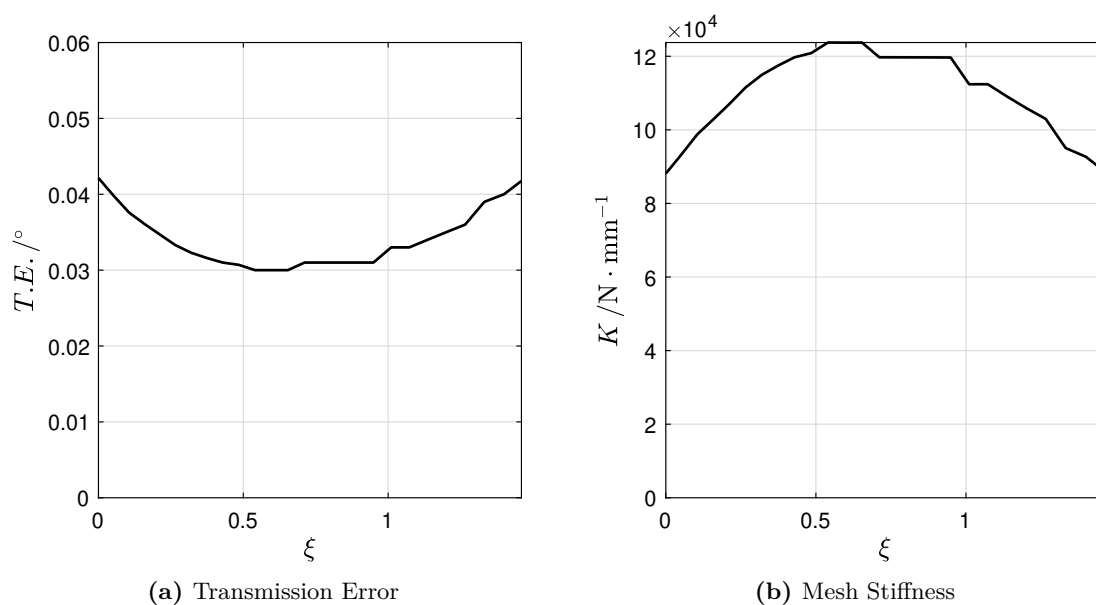


Figure B.28 Normalized mesh stiffness of the C20 model.



(a) Transmission Error

(b) Mesh Stiffness

Figure B.29 Numerical results of the CORR1 model.

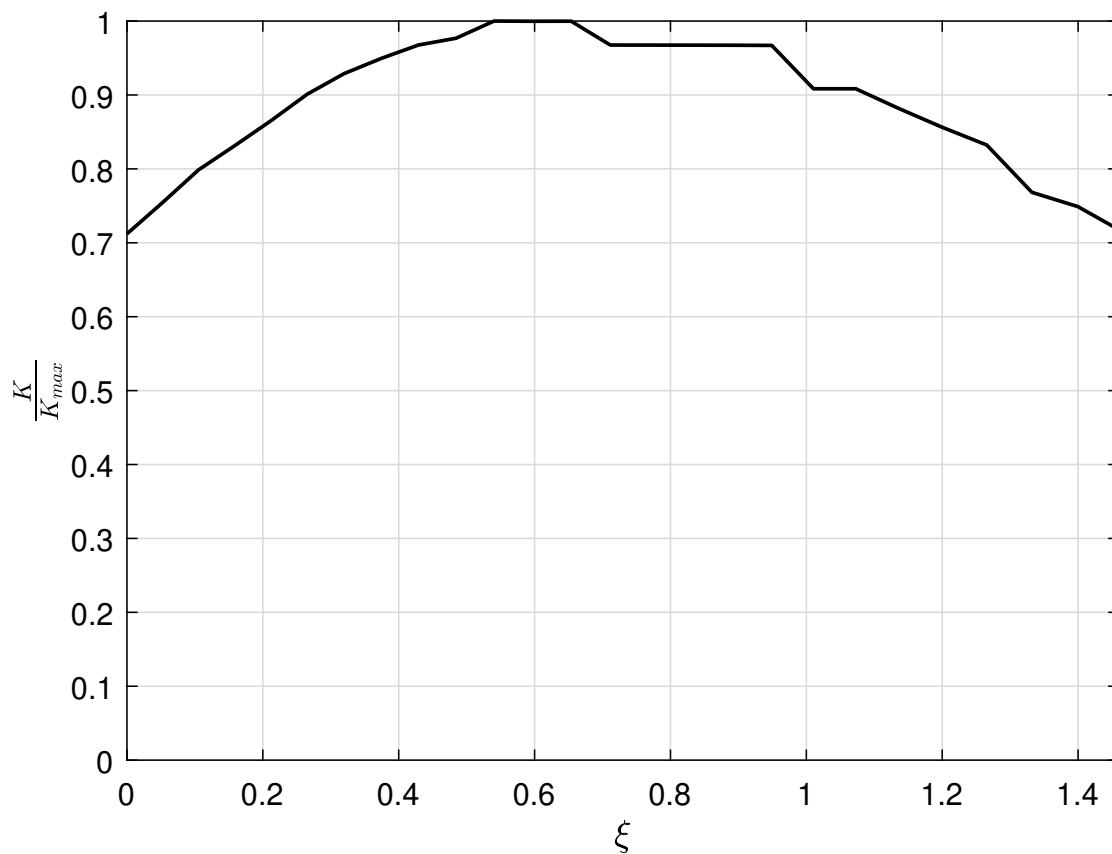
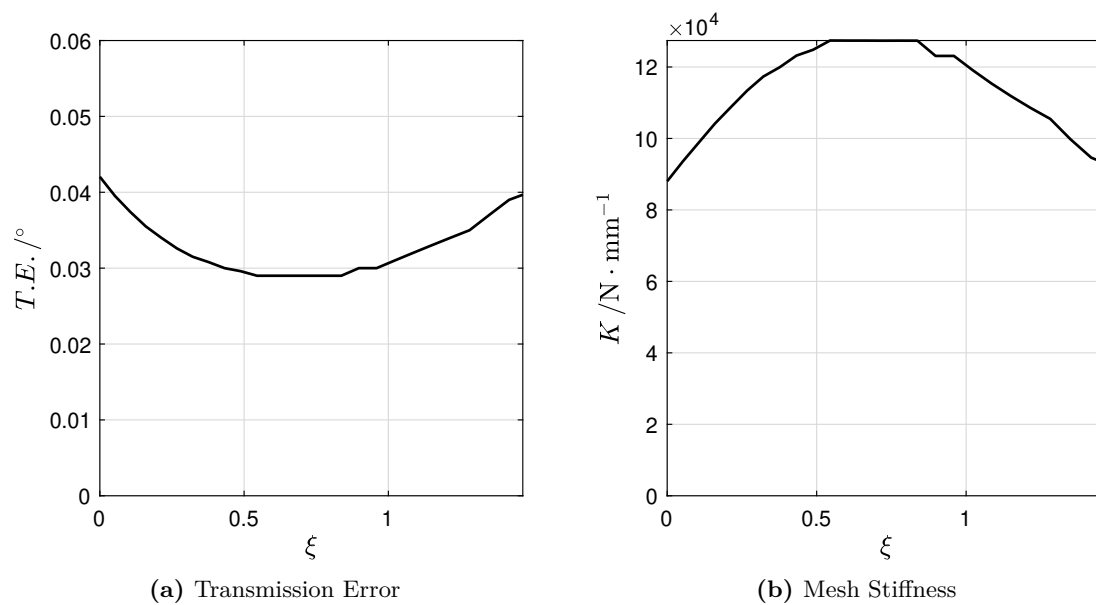


Figure B.30 Normalized mesh stiffness of the CORR1 model.



(a) Transmission Error

(b) Mesh Stiffness

Figure B.31 Numerical results of the CORR2 model.

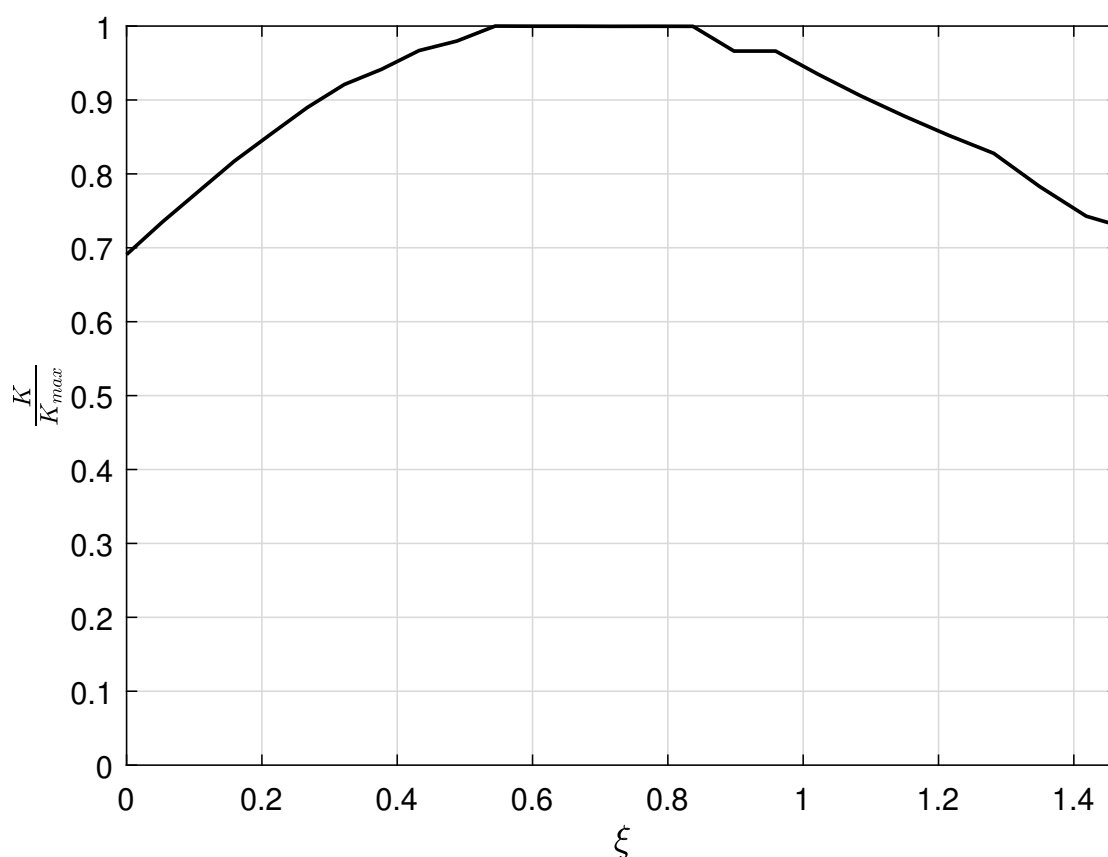
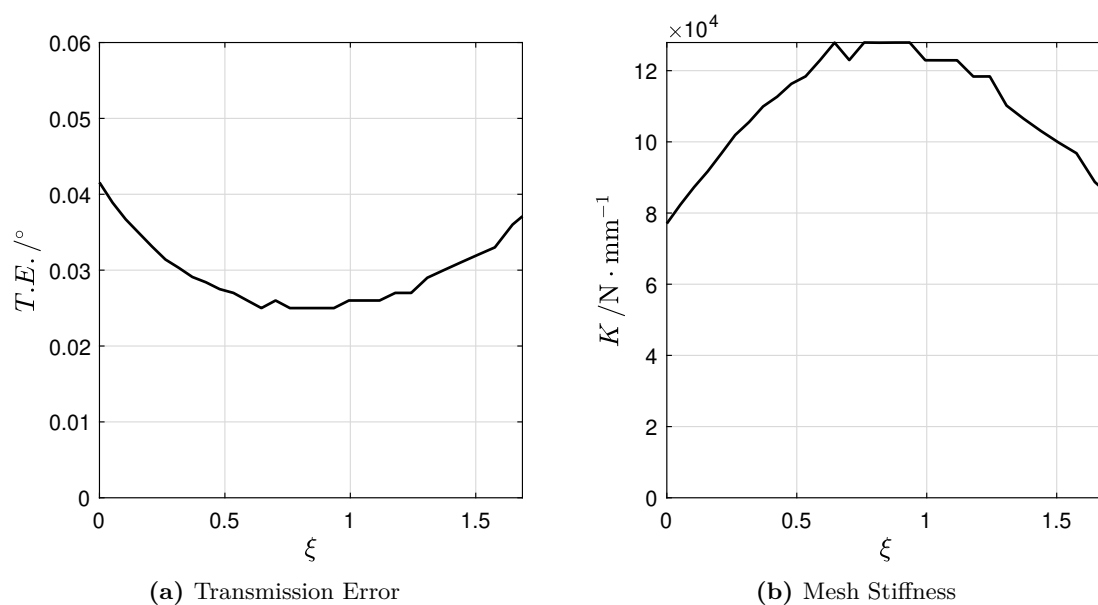


Figure B.32 Normalized mesh stiffness of the CORR2 model.



(a) Transmission Error

(b) Mesh Stiffness

Figure B.33 Numerical results of the K01 model.

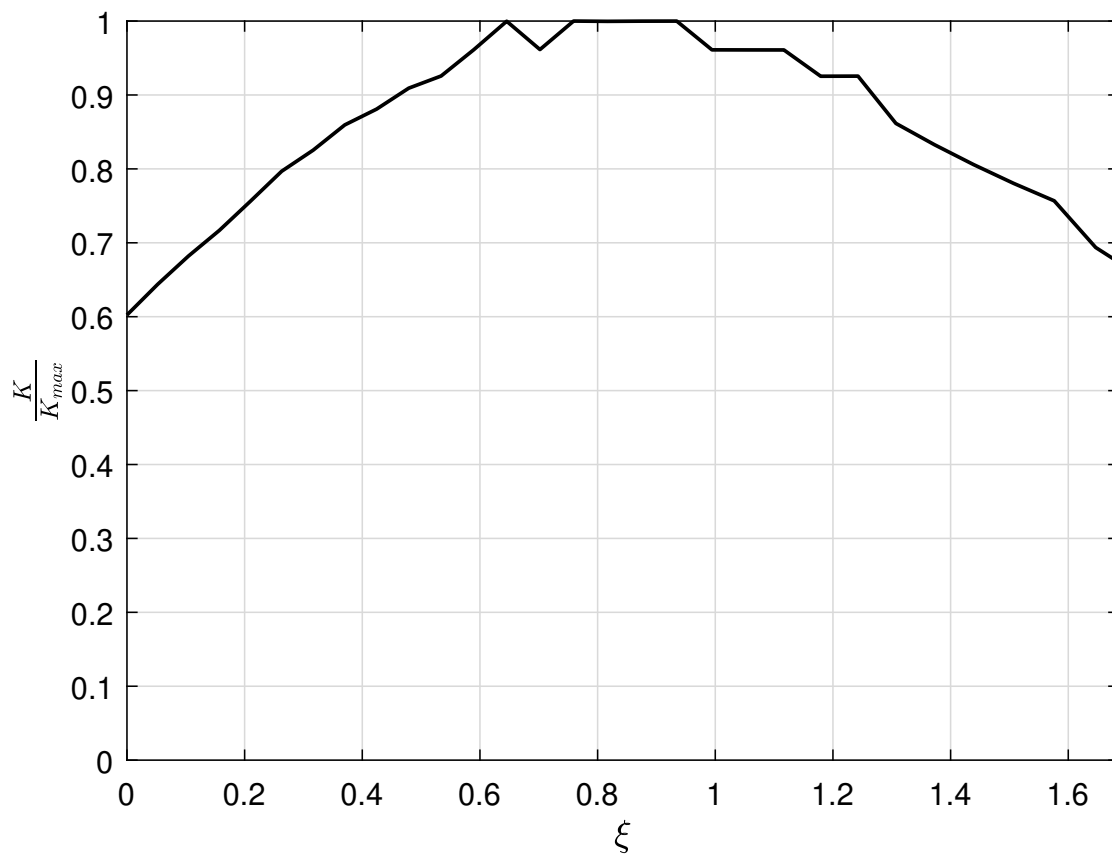


Figure B.34 Normalized mesh stiffness of the K01 model.

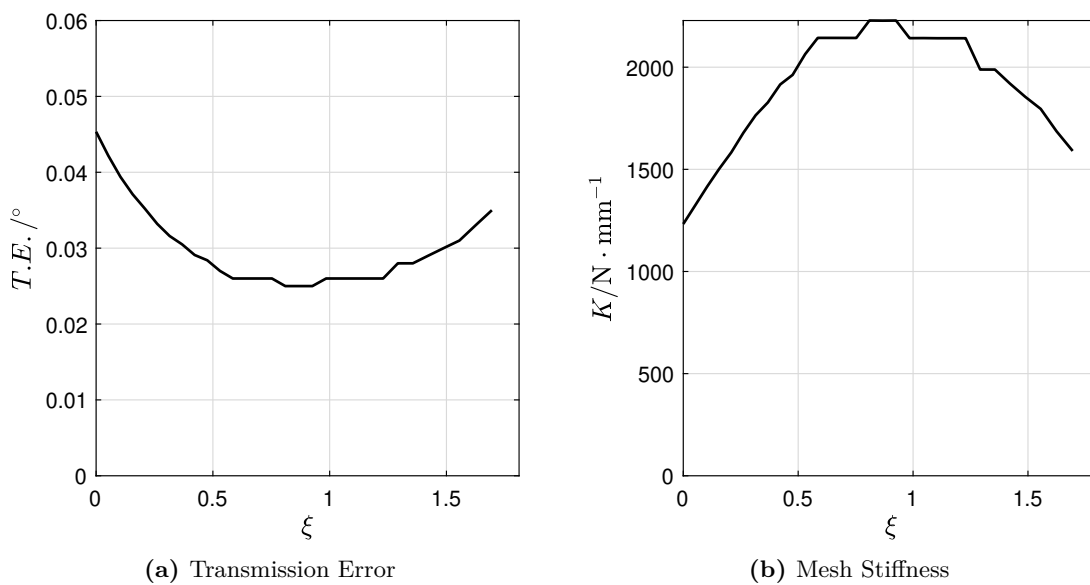


Figure B.35 Numerical results of the K02 model.

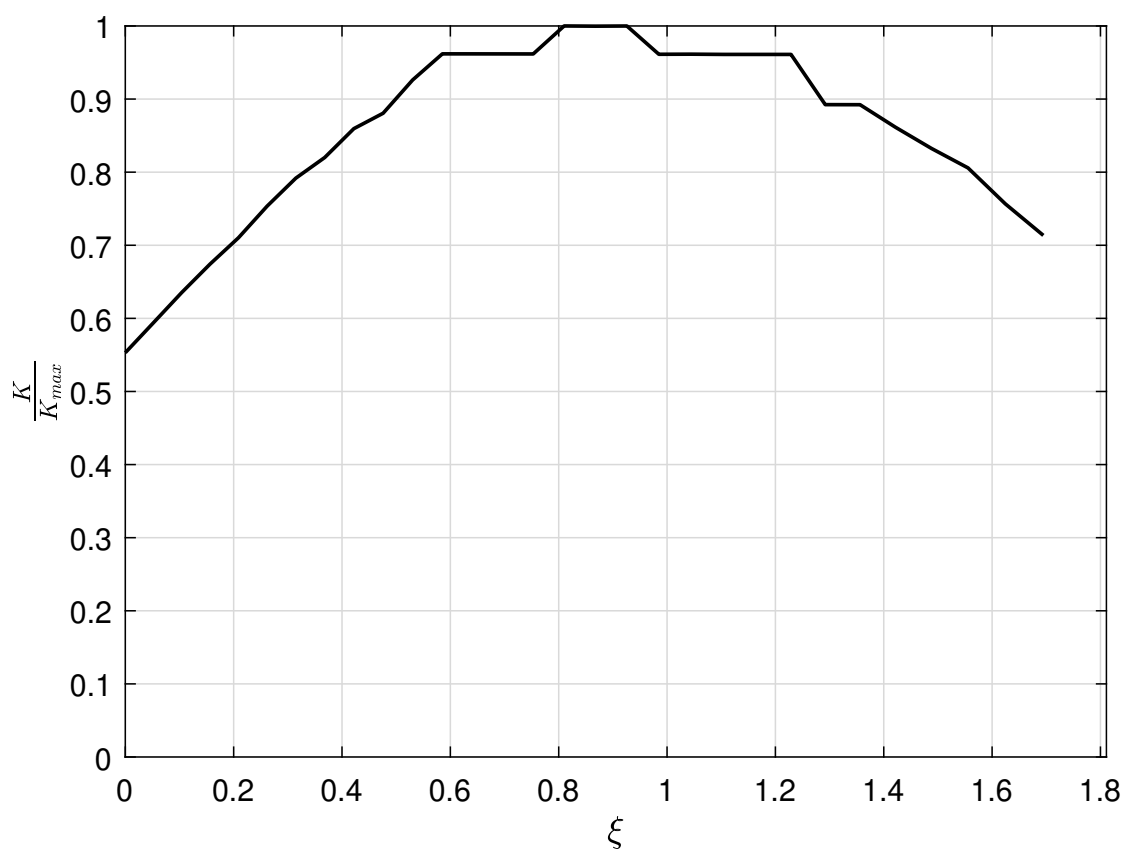
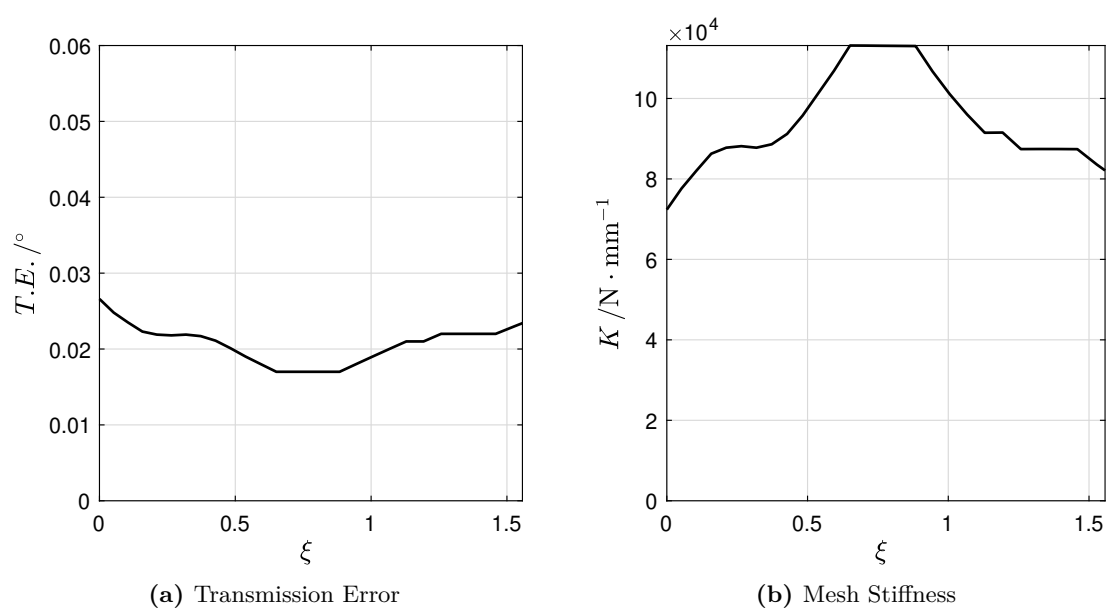


Figure B.36 Normalized mesh stiffness of the K02 model.



(a) Transmission Error

(b) Mesh Stiffness

Figure B.37 Numerical results of the ER1 model.

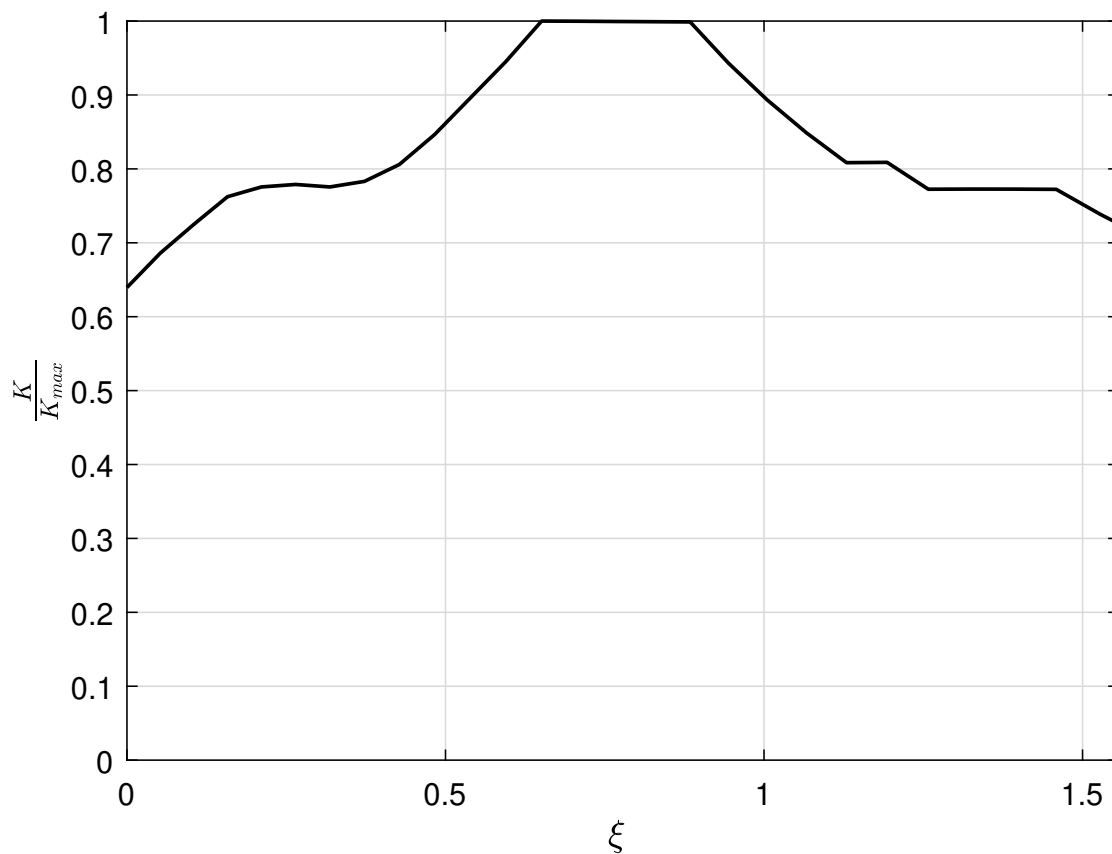


Figure B.38 Normalized mesh stiffness of the ER1 model.

ER2

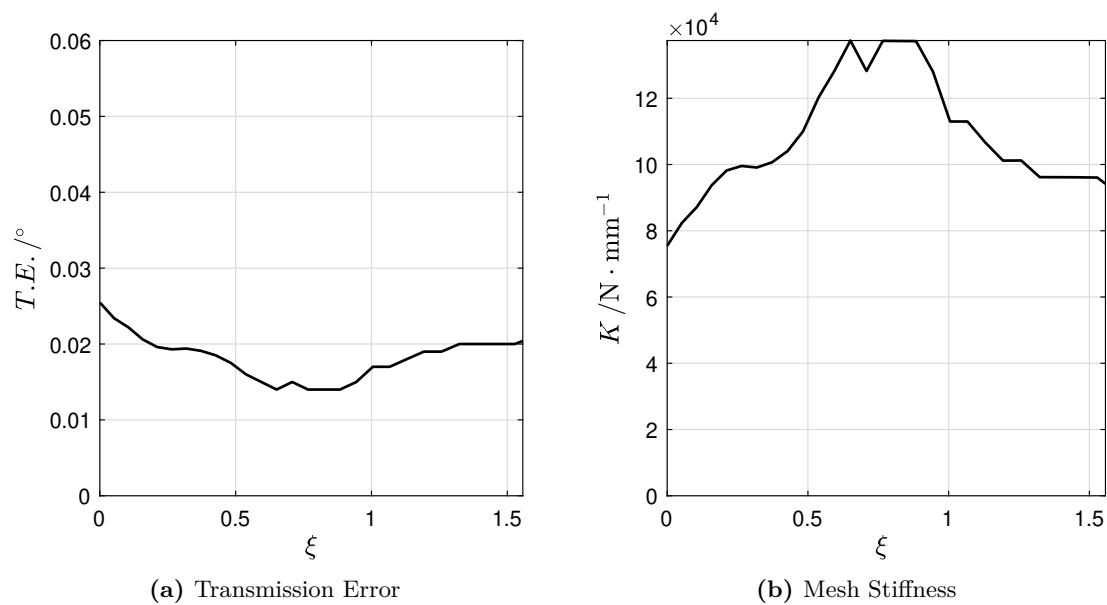


Figure B.39 Numerical results of the ER2 model.

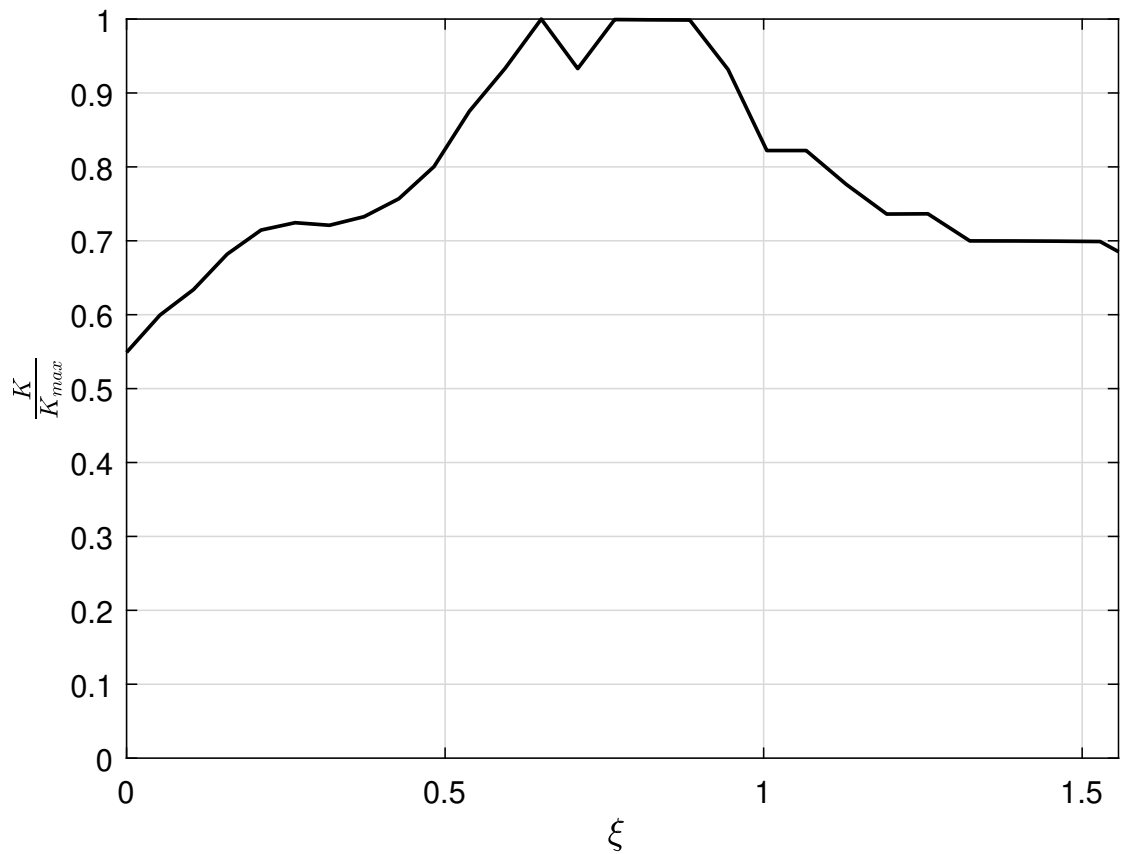
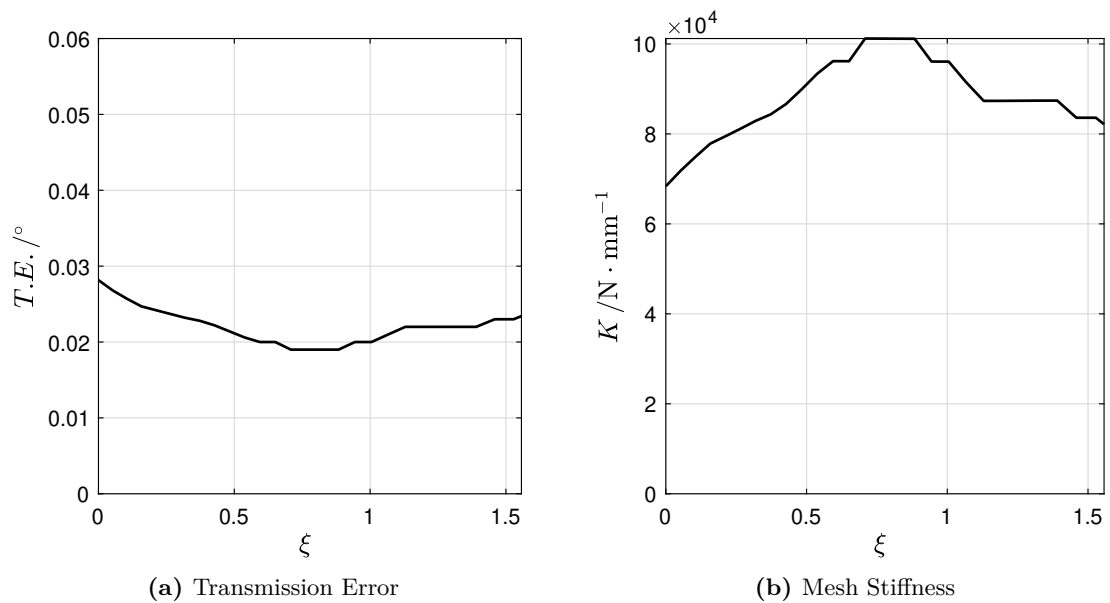


Figure B.40 Normalized mesh stiffness of the ER2 model.

ER1M45



(a) Transmission Error

(b) Mesh Stiffness

Figure B.41 Numerical results of the ER1M45 model.

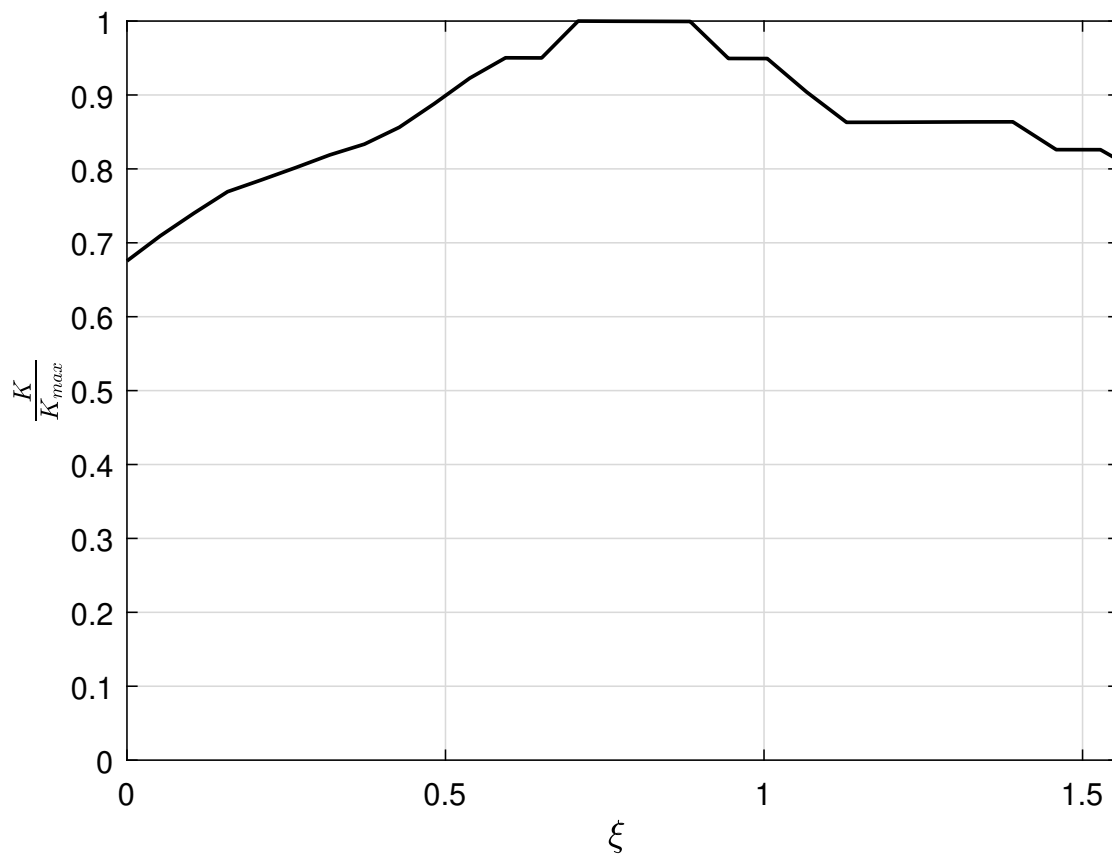


Figure B.42 Normalized mesh stiffness of the ER1M45 model.

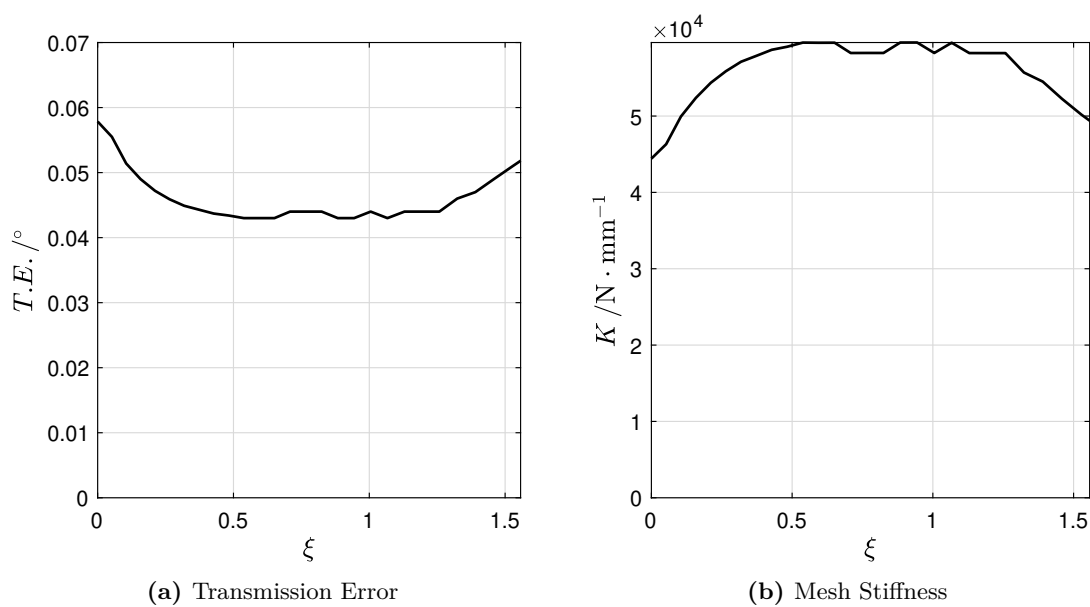


Figure B.43 Numerical results of the CR1 model.

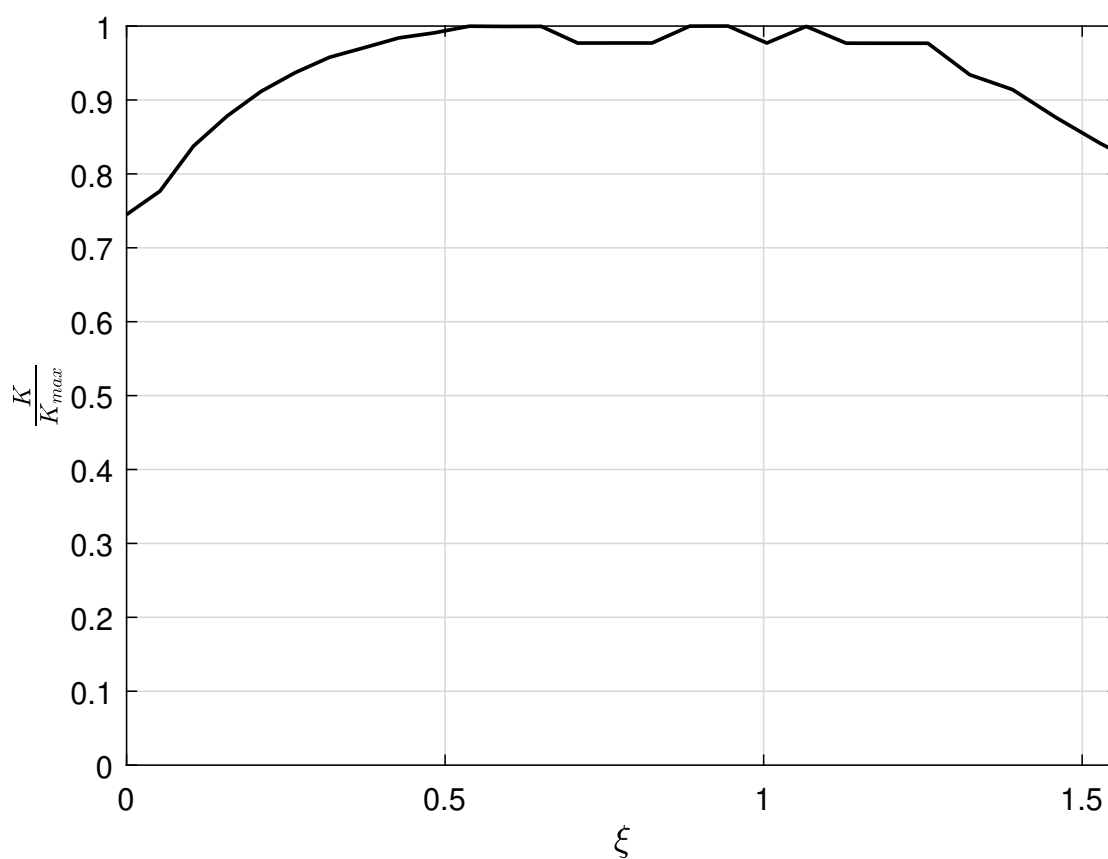
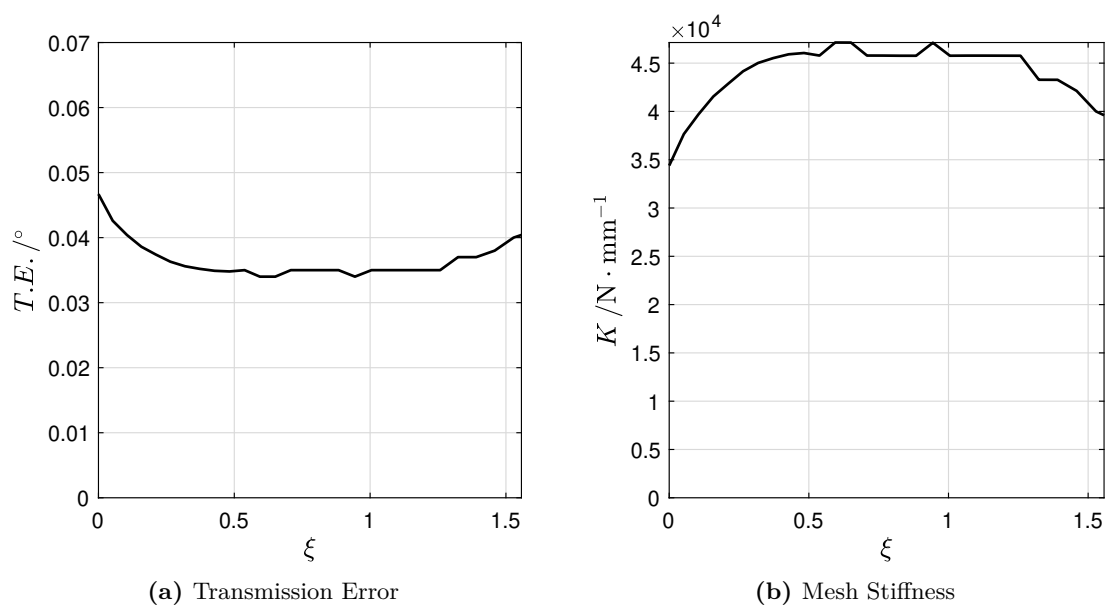


Figure B.44 Normalized mesh stiffness of the CR1 model.



(a) Transmission Error

(b) Mesh Stiffness

Figure B.45 Numerical results of the CR2 model.

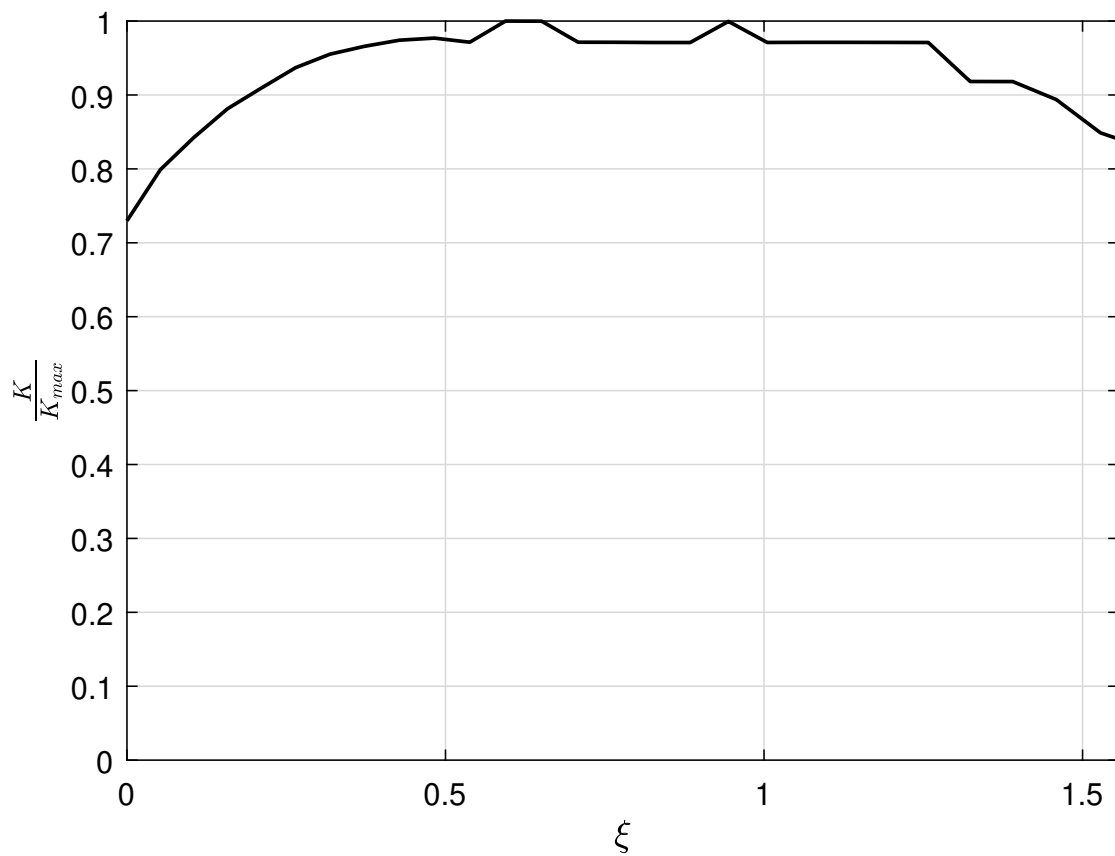


Figure B.46 Normalized mesh stiffness of the CR2 model.